IMPACT OF THE NAD^+ SALVAGE PATHWAY ON THE MOTOR SYSTEM AND BIOENERGETICS

A Dissertation Presented to

the Faculty of the Graduate School

at the University of Missouri

In Partial Fulfillment

of the Requirements for the Degree

Doctor of Philosophy

By

Samuel Lundt

Dr. Shinghua Ding, Thesis Supervisor

July 2023

The undersigned, appointed by the dean of the Graduate School,
have examined the dissertation entitled:

IMPACT OF THE NAD^+ SALVAGE PATHWAY ON THE MOTOR SYSTEM AND BIOENGERTICS

presented by Samuel Lundt,

a candidate for the degree of doctor of philosophy,

and hereby certify that, in their opinion, it is worthy of acceptance.

_____

Shinghua Ding, PhD

_____

Kevin Gillis, DSc

_____

Ilker Ozden, PhD

_____

Luis Polo-Parada, PhD

DEDICATION

I would like to dedicate this dissertation to my parents and siblings for all the support and encouragement they have given me. Also, to Clarence, who I never met but made all of this more achievable because of one very odd decision.

ACKNOWLEDGEMENTS

First and foremost, I would like to thank my advisor Dr. Shinghua Ding, who has served as a great mentor to me for the past six years. He is always pushing me to think more deeply about my experiments, to think about why and how an experiment works and not just collect data and present the result. His guidance to me about research and my career in general has been valuable. I will always be grateful for the patience, ideas and funding to make it possible for me to attain a Ph.D. I would also like to thank my committee members, Dr. Luis Polo-Parada, Dr. Kevin Gillis and Dr. Ilker Ozden. Dr. Polo-Parada especially has been generous in providing advice, knowledge, and lab space with me so that I was able to learn the skills that I needed to perform the most interesting parts of my research. Moreover, I would just like thank my entire committee for their insightful comments and suggestions.

I also want to thank my lab mates Nannan Zhang and Zhe Zhang, both of whom have been with me my entire Ph.D. journey. Nannan was always willing to share her experience with me to help me learn the finer details about performing research. Zhe and I started our Ph.D. research at the same time and I cannot imagine sharing this experience with anybody else. Finally, thanks to all of the other past members of the Ding lab that I have been able to work with.

TABLE OF CONTENTS

List of Figures

List of Tables

IMPACT OF THE NAD^+ SALVAGE PATHWAY ON THE

MOTOR SYSTEM AND BIOENERGETICS

Samuel Lundt

Dr. Shinghua Ding, Dissertation Supervisor

Abstract

Nicotinamide adenine dinucleotide (NAD^+) is a metabolite pivotal to numerous cellular functions, including energy metabolism, DNA repair, and protein modification. The majority of NAD^+ is generated by the NAD^+ salvage pathway, which is rate limited by nicotinamide phosphoribosyltransferase (NAMPT). NAMPT and the NAD^+ salvage pathway are critical to most cell types, but are especially important to neuronal health and function. Additionally, the NAD^+ salvage pathway is increasingly being investigated for being involved in neurodegenerative diseases. Recently, the importance of NAMPT to motor and neuromuscular junction (NMJ) activity and survival has been reported. However, how the NAD^+ salvage pathway affects NMJ function and what metabolic pathway are dysregulated when the salvage pathway becomes impaired warrants further investigation. In Chapter one, I review intracellular NAD^+ homeostasis, NAD^+ salvage pathway enzymes, and the importance of NAD^+ homeostasis in health and neurodegenerative diseases, specifically ALS. In Chapter two and Chapter three, I used inducible and conditional projection neuron-specific NAMPT knockout mouse, which previously was found to experience profound motor dysfunction and neuron loss. I investigated NMJ structure and function following NAMPT deletion and what benefits NMN administration produces. I also studied how the metabolic and transcriptional profiles in the motor cortex of these knockout mice are altered after NAMPT loss. In

Chapter Four, based on the similar phenotypes between the NAMPT knockout mice and ALS mice and NAD^+ reduction in ALS mouse model, I investigated how dietary NMN supplementation affects motor behavior and NMJ function in $SOD1^{G93A}$ ALS mice. Overall, the results from these studies provide novel insights into how the NAD^+ salvage path is critical for NMJs and what metabolic stress and signaling pathways are responsible for the neuronal death after NAMPT deletion

Chapter one: Introduction

1.1 Introduction

Nicotinamide adenine dinucleotide (NAD^+) (Fig. 1.1) is one of the most abundant and critical metabolites in the human body. NAD^+ is essential for its ability to be oxidized and reduced in cellular energy metabolism and bioenergetics (i.e., glycolysis, TCA cycle, oxidative phosphorylation, fatty acid oxidation). NAD^+ also functions as a co-factor for NAD^+-consuming enzymes, such as sirtuins (SIRTs) and poly-(ADP-ribose) polymerases (PARPs). NAD^+ consumption is utilized for many intracellular processes, including DNA repair, the circadian clock, protein modification, and autophagy [1-5]. Turnover of NAD^+ varies widely across tissue types and disrupting NAD^+ homeostasis elicits harmful effects at both the cellular and systemic levels [6]. Thus, the maintenance of intracellular NAD^+ levels is crucial for cellular function and survival.

Intracellular NAD^+ levels generally fluctuate with the circadian clock, making NAD^+ homeostasis a constant and dynamic process. NAD^+ homeostasis is also dependent on cell type, because NAD^+ levels vary across tissues [7-9]. Additionally, NAD^+ is not evenly distributed within a cell. Intracellular compartments have distinct NAD^+ pools, with the cytosol and nucleus having similar levels but mitochondria are considerably higher [10]. These pools appear independent from each other so the maintenance of NAD^+ levels involves balancing biosynthesis and consumption in each sub-compartment [10, 11]. During energy metabolism, NAD^+ is rapidly oxidized or reduced, with NAD^+ reduced to NAD(H) and NAD(H) oxidized back to NAD^+ to maintain redox balance. NAD^+ is not directly consumed, so this does not cause appreciably lower NAD^+ levels. However, NAD^+ also serves as a co-factor to NAD^+-consuming enzymes, which lowers cellular NAD^+ and

impacts NAD homeostasis. In the following sections, I will discuss cellular NAD^+ metabolism, NAD^+ salvage pathway and how salvage pathway is important in NAD^+ homeostasis, physiological health, disease, and neurodegeneration.

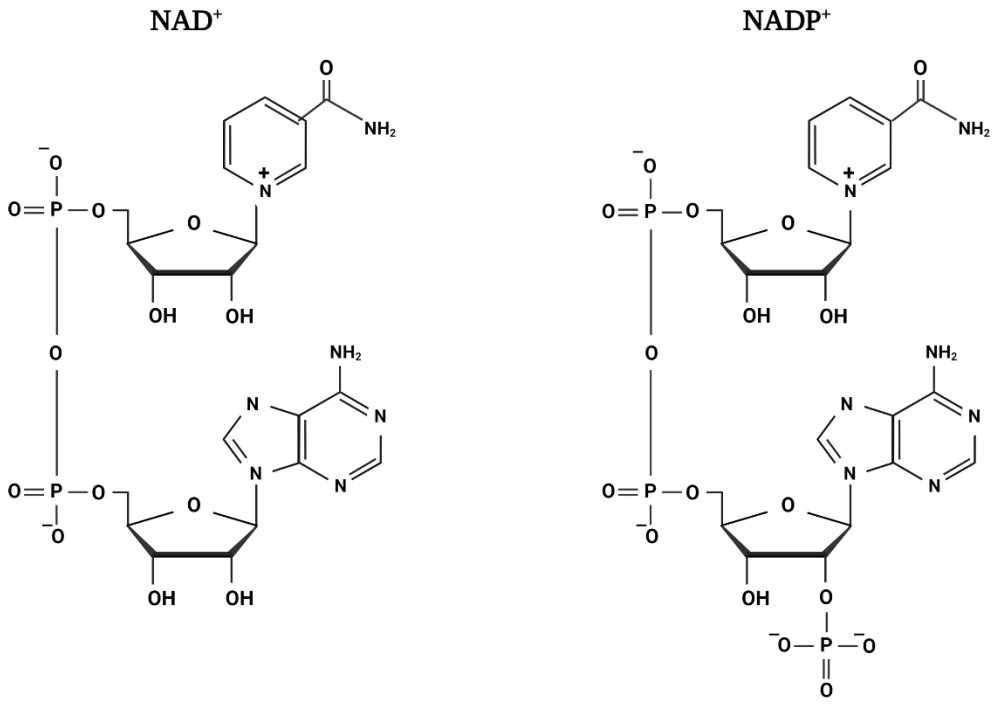

Figure 1.1. Chemical structure of NAD^+ and $NADP^+$.

1.2 NAD^+ homeostasis

NAD+ levels are affected by the balance between biosynthesis and consumption. To increase availability, cells have multiple pathways that can generate NAD^+, each beginning with a different metabolite. Decreases in NAD^+ are due to NAD^+ consuming enzymes, where the end-products of the reactions are nicotinamide (NAM) and ADP-ribose/cyclic ADP-ribose [12]. Ensuring NAD^+ homeostasis matches cellular demands is critical. NAD^+ availability can be rate limiting to energy metabolism and, should levels decline enough, glycolysis and the TCA cycle can be inhibited leading to cell death [13].

1.2.1 NAD^+ biosynthesis pathways

In mammals, there are three different paths for NAD^+ biosynthesis: the *de novo*, Preiss-Handler, and NAD^+ salvage pathways (Fig 1.2). The *de novo* pathway starts with the amino acid tryptophan and is converted into nicotinic acid mononucleotide (NAMN), which can enter the Preiss-Handler pathway to form NAD^+ [14]. The *de novo* pathway is a dominant pathway in the liver and intestines but is not highly expressed in the central nervous system (CNS), possibly because biological intermediates in the pathway are potentially neurotoxic [1, 15]. The Preiss-Handler pathway utilizes nicotinic acid and has three steps. In the first step, NA is converted to NAMN and NAMN is converted into nicotinic acid adenine dinucleotide (NAAD). NAAD is synthesized into NAD^+ by NAD synthetase [16]. The Preiss-Handler pathway is predominantly expressed in visceral organs and does not have strong expression in the CNS [17, 18].

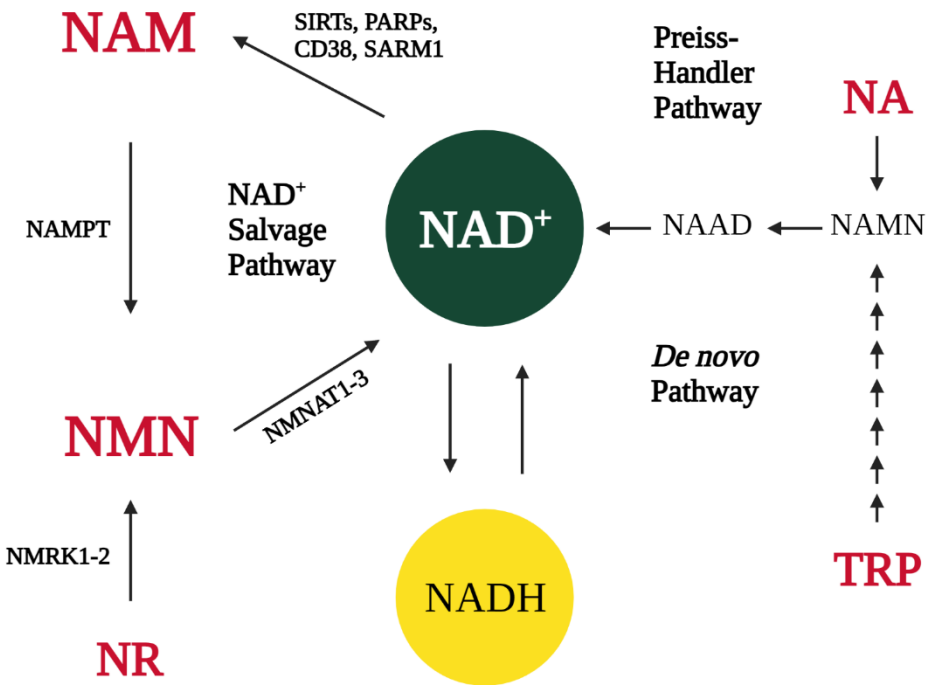

Figure 1.2. NAD^+ biosynthetic pathways. NAM, nicotinamide; NMN, nicotinamide mononucleotide; NR, nicotinamide riboside; NA, nicotinic acid; TRP, tryptophan; NAMN, nicotinic acid adenine mononucleotide; NAAD, nicotinic acid adenine dinucleotide.

The NAD^+ salvage pathway is considered the dominant NAD^+ biosynthetic pathway in mammalian cells [16]. The NAD^+ salvage pathway consists of only two steps and begins with nicotinamide (NAM). NAM is converted into nicotinamide mononucleotide (NMN) by NAMPT, this was also determined to be the rate limiting step [19]. NMN is converted to NAD^+ by nicotinamide mononucleotide adenylyltransferases (NMNAT1-3) [20]. NMN can also be formed from nicotinamide riboside (NR) in an NAMPT-independent manner, using nicotinamide riboside kinases (NMRK1-2). However, NAMPT expression is considered as ubiquitous while NMRK expression appears to be tissue specific [21, 22]. Also, circulating NAM levels are over a thousand-fold higher than NR, indicating a reliance on the NAMPT-dependent NAD^+ biosynthesis [6]. While the NAD^+ salvage pathway enzymes are expressed in nearly all tissues of the body, the expression in the CNS may be especially reliant on the salvage pathway due to the limited expression of *de novo* and Preiss-Handler pathway enzymes. This makes neurons especially susceptible to dysfunction in response to impairments to the salvage pathway.

1.2.2 NAD^+ consumption

NAD^+ availability is also affected by the activity of NAD^+ consuming enzymes. This includes SIRTs, PARPs, CD38/157, and SARM1. SIRTs are NAD^+-dependent deacetylases and are involved in transcription regulation, mitochondrial metabolism, autophagy, and apoptosis [12]. There are seven SIRT proteins which are located in the nucleus (SIRT1, 6, 7), cytosol (SIRT2), and mitochondria (SIRT3, 4, 5) [2]. Among the SIRTs, SIRT1, 3, and 6 have been the most widely investigated and have been found to be responsible for the many of the most prominent effects in cells [23]. The widespread effects of SIRTs are due to their interactions with many different signaling pathways such as,

AMPK, NF-κB, PGC-1α, Akt, and HIF-1α pathways [24-28]. Increasing SIRT activity or expression can improve lifespan, function of metabolic pathways, and motor behavior [29, 30]. Overall, SIRT activity, which is reliant on NAD^+ availability, is critical for cellular and systemic function.

PARPSs are another major consumer of NAD^+. There are seventeen PARP proteins, and they are primarily involved with DNA repair, genome maintenance, and cell death [20, 31]. PARP1 is estimated to account for over 80% of cellular PARP activity [20, 32]. Parthanatos, a type of cell death characterized by excessive addition of poly-ADP-ribose (PAR) polymers (PARylation), can occur with PARP1 over-activation. This can quickly deplete NAD^+ levels [2, 31-33]. During aging, NAD^+ levels decrease while PARylation increases, indicating that PARP activity may be contributing to age-related NAD^+ decline [29]. PARPs are critical for correcting DNA damage, however too much activity may result in more harm than good.

CD38 and CD157 are extracellular, membrane bound glycohydrolases and are important in regulation of Ca^{2+} second messenger signaling [12, 34]. Both CD38 and CD157 have enzymatic activity. CD38 can function as both a glycohydrolase or a base exchanger, generating NAM and cADPR or $NAADP^+$ respectively. CD157 only has glycohydrolase activity. Both cADPR and $NAADP^+$ are involved in Ca^{2+} signaling [35]. CD38 appears to be a major consumer of NAD^+. In CD38 knockout mice, NAD^+ levels were significantly elevated in all tissues that were measured, with the increase ranging from 88% to 2600% [36]. In fact, it has been suggested that age-related NAD^+ decline could be tied to CD38. As mice age, multiple tissues experience increasing CD38 expression and

activity. Other major NAD^+ consumers, SIRT1 and PARP1, do not have similar changes [37].

A more recently identified NAD^+ consuming enzyme is sterile α and TIR motif-containing 1 (SARM1). SARM1 is an NAD^+ hydrolase with a TIR domain that directly binds NAD^+. SARM1 is responsible for executing Wallerian degeneration, which is programmed axonal degeneration [38]. Interestingly, activation of SARM1 may not require physical or chemical injury but rather a change in NMNAT2 availability. Impairing the transport of NMNAT2 from the nucleus to the axon was enough to induce SARM1-dependent axon degeneration [39]. SARM1 activation produces a Ca^{2+} influx and instigates a Ca^{2+}-mediated cascade resulting in axonal degeneration [40]. NAD^+ consumption is important for many cellular activities though increased activity of these NAD^+-dependent enzymes can be problematic. Overall, due to NAD^+ being involved in many critical functions, cells are dependent upon a coordinated balance between NAD^+ synthesis and consumption.

1.3 NAD^+ salvage pathway enzymes

The NAD^+ salvage pathway is responsible for synthesizing the majority of intracellular NAD^+ in mammalian cells. While this is the primary function of NAMPT and NMNAT, both enzymes have been implicated in non-biosynthetic cellular activities as well.

1.3.1 NAD^+ Biosynthesis

NAMPT, previously known as visfatin or pre-B-cell colony enhancing factor, is considered to be ubiquitously expressed, with liver and adipose tissues having especially strong expression. In the CNS, NAMPT expression appears to be mostly restricted to

neurons [41-43]. There are two forms of NAMPT, intracellular and extracellular. Both forms are enzymatically active, with the extracellular form possibly having elevated activity [43]. Extracellular NAMPT is released in extracellular vesicles from various tissues, with the liver and adipose tissue responsible for a large amount. Extracellular NAMPT can be taken up by other organs and tissues in the body and actively contribute to the intracellular NAD^+ biosynthesis [44].

The knockout or inhibition of NAMPT produces many deficits. NAMPT is necessary for survival of embryonic and adult mice [43, 45]. The deletion of NAMPT from specific tissues has demonstrated the importance of NAMPT, with knockout in liver, muscle, neurons, glia, adipose, or kidney resulting in impairments that can extend beyond the knockout tissue [46-52]. Conversely, over-expressing NAMPT tends to be beneficial, not just to the targeted tissue but throughout the body [44, 46, 53-57].

There are three isoforms of NMNAT, namely NMNAT1-3, each with a different sub-cellular localization. NMNAT1 is located in the nucleus, NMNAT2 is located in the cytoplasm and Golgi, and NMNAT3 is located in the mitochondria. NMNAT1 is the most widely expressed of the three isoforms with NMNAT3 being weakly expressed in many of the same tissues. NMNAT2 appears to be the most tissue specific of the three, being expressed in skeletal muscle, heart, and brain [11]. NMNAT isoforms are enzymatically non-redundant, meaning the loss of one is not compensated for by the other two. Interestingly, the deletion of NMNAT1 or NMNAT2 is lethal whereas mice lacking NMNAT3 are anemic but have normal lifespans [58-60]. Over-expression of NMNATs has been less studied but are protective against axonal degeneration [61-63].

1.3.2 Non-enzymatic functions

While the importance of NAMPT and NMNATs in NAD^+ biosynthesis is well understood, actions outside the context of NAD^+ biosynthesis have been identified for both proteins. NAMPT, primarily the extracellular form, may function as an immunomodulatory cytokine. Secreted NAMPT can bind to extracellular receptors, such as TLR4 or CCR5, and activate proinflammatory signaling pathways [64]. The role of NAMPT in inducing an immune response is still being investigated. More recently, the NAMPT homolog in yeast exhibited a chaperone activity to protect against proteotoxicity [65]. Whether this also occurs in mammalian cells is unknown.

NMNATs have a well-established non-enzymatic function, though this appears to be mostly restricted to neurons. NMNATs have demonstrated a strong chaperone like activity. NMNATs can prevent unfolding and promote refolding of proteins in response to heat shock [66]. This chaperone function is active in neurodegenerative diseases. NMNATs can directly bind proteins involved in Parkinson's disease (PD) (α-synuclein), Alzheimer's disease (AD) (phosphorylated Tau, $A\beta_{40}$, IAPP), and Huntington's disease (huntingtin) [65, 67-69]. NMNATs can promote clearance of these proteins, likely via autophagic pathways, before they form pathogenic aggregates [68]. Importantly, this function is independent of enzymatic activity [65, 69]. Additionally, NMNATs may have a role in synapses. In *Drosophila*, NMNAT was important to both synapse stability and neurotransmission [70, 71]. NAMPT and NMNATs provide benefits beyond their role in NAD^+ biosynthesis, however, these functions are secondary to the primary function in regeneration of NAD^+.

1.4 NAD^+ salvage in health, aging, and disease

NAD^+ homeostasis is an important factor in general health and well-being. As mentioned previously, NAD^+ is critical for intracellular bioenergetics and serves as the primary redox molecule. In glycolysis and the TCA cycle, NAD^+ is reversibly reduced to NAD(H). The oxidation of NAD(H) back to NAD^+ during oxidative phosphorylation is what generates the proton gradient necessary for ATP production [13]. Additionally, the cellular response to oxidative stress is reliant on NAD^+; 10% of NAD^+ is converted to $NADP^+$ (Fig. 1.1) by NAD kinase [72], which can be reduced to NADPH, the primary redox agent against oxidative stress [1, 73].

The interaction between NAMPT activity and SIRT activity appears important for energy metabolism. The NAMPT-NAD^+-SIRT axis is involved in controlling energy intake and expenditure. Interestingly, energy intake can affect NAD^+ availability, with diets rich in lipids and/or simple carbohydrates leading to lower NAD^+ levels [1]. The hypothalamus controls many behaviors, including feeding and locomotion. Extracellular NAMPT can be taken up by the hypothalamus and increase NAD^+ levels and SIRT activity [74]. SIRTs deacetylate the transcription factor FOXO1 and mediate activity of hypothalamic neurons involved with locomotor activity and energy expenditure, resulting in both being elevated. The NAMPT-NAD^+-SIRT axis is dependent on NAMPT's enzymatic activity because loss of the activity eliminates these effects. Curiously, food intake was also reduced from either increased NAMPT activity or NMN administration [75]. This demonstrates the complex nature of the involvement of NAMPT in cellular energy metabolism.

Changes to NAD^+ homeostasis have been found to be involved in aging and many diseases. During the course of aging, NAD^+ levels are reduced in most tissues throughout

the body, including the brain, liver, and skeletal muscle [9, 37, 76]. There are two likely causes for the reduction in NAD^+: increased consumption or decreased biosynthesis. Supporting the role of increased NAD^+ consumption, PARP1 and CD38 expression and activity are elevated with age, thus decreasing NAD^+ availability. Inhibition or knockout of PARP1 or CD38 improved NAD^+ levels [37, 77]. There is also evidence indicating decreased NAD^+ biosynthesis, with changes to NAMPT being responsible. Both NAMPT expression and activity are lower in aged mice, with the reduced activity likely being the result of increased acetylation [78, 79]. Also, extracellular NAMPT levels decline with age and may represent a biomarker for aging. Increasing extracellular NAMPT in aged mice improved motor behavior and lifespan [44]. It is likely that age-related NAD^+ declines are the result of both increased consumption and reduced biosynthesis. Fortunately, administering NAD^+ precursors can restore NAD^+ levels and correct some age-related declines [80-82].

Impairments to NAD^+ homeostasis have been found in many different diseases, including metabolic and neurodegenerative disorders. The circadian oscillation of NAD^+ and NAMPT in the hypothalamus and liver are disrupted from a high-fat diet, which may impair daily activity and food intake [75]. Deleting NAMPT from adipocytes produces obesity-related impairments, including glucose intolerance and insulin resistance [50]. Obesity is a risk factor for many metabolic disorders, including diabetes. In diabetic mice, NAMPT-related NAD^+ production is reduced and NMN supplementation can elevate NAD^+ and reverse many disease-related dysfunctions [78]. Changes to NAD^+ homeostasis have been found in neurodegenerative conditions, including AD, PD, and amyotrophic lateral sclerosis (ALS). In AD mice, both NAD^+ and NAMPT are reduced in the cortex and

hippocampus and AD mice may experience a larger age-related decline in NAMPT expression [83, 84]. NAD^+ repletion was able to increase NAMPT expression and improved learning and memory and impaired amyloid plaque formation [83]. In *in vitro* PD models, NAMPT and NAD^+ levels declined as oxidative stress was elevated [85]. This may lead to bioenergetic stress and PARP1 activation. However, when NMN is administered these harmful effects are prevented [86]. The NAD^+ salvage pathway and ALS will be covered in Section 1.5.

1.5 NAD^+ salvage in neurodegeneration

While all cells require NAD^+, neurons are especially vulnerable to changes in NAD^+ homeostasis. NAD^+ depletion has been strongly linked to neurodegeneration, both during normal aging and in disease, especially aging-related neurodegenerative diseases. One common aspect of neurodegenerative diseases is axonal degeneration (i.e. Wallerian degeneration).

A role for NAD^+ and the salvage pathway in axonal degeneration was first observed in Wallerian degeneration slow (Wld^s) mice. These mice demonstrated delayed axonal degeneration following injury. Later it was determined that these mice express a chimeric NMNAT1 protein in the cytosol and expression was high in the nervous system [87]. The neuroprotection was driven by the NMNAT activity in the protein. Following injury, NAD^+ is quickly depleted but Wld^s neurons, or neurons overexpressing NMNATs, can prevent NAD^+ loss and significantly reduce axonal degeneration [88].

Later, Wallerian degeneration was determined to be due to SARM1 activation because loss axonal degeneration was prevented by the knockout of SARM1 [89]. Additionally, the decline in NAD^+ levels was due to SARM1. SARM1 consumes NAD^+

and activates a Ca^{2+} cascade that results in the destruction of axons. This SARM1-mediated degeneration requires this NAD^+ catalytic activity [38]. Recently, how NMNAT and SARM1 interact and influence axonal degeneration has become better understood. SARM1 serves as a sensor of the NMN/NAD^+ ratio and can bind both NMN and NAD^+. Thus, SARM1 effectively monitors NMNAT activity, whereby if NMNAT activity declines, the NMN/NAD^+ ratio increases and activates SARM1 leading to axonal degeneration [90]. Neurons are especially vulnerable because NMNAT2, which is highly expressed but degrades quickly, and requires axonal transport to reach the synaptic terminals [91, 92].

Being the rate-limiting enzyme of the salvage pathway, NAMPT is hugely influential on neuronal survival. NAMPT is neuroprotective, where over-expression of NAMPT can prevent neuron apoptosis from glutamate excitotoxicity or oxygen-glucose deprivation [93]. The involvement of NAMPT in neurodegeneration has been well demonstrated in mice, where NAMPT can be conditionally and inducibly deleted from adult mouse projection neurons. These mice have a nearly 70% decrease in cortical NAD^+, quickly develop motor dysfunction and become paralyzed. The NMJs also display many abnormalities, such as fragmentation, poly-innervation, and axonal swelling, while also having impaired neurotransmission. In the motor cortex, there is significant neuron loss and, despite NAMPT being only deleted from neurons, widespread glial cell activation. Mice only survive around 3 weeks following loss of NAMPT. Importantly however, administering NMN to these mice slows the motor performance decline and improves lifespan [48].

The knockout of NAMPT from a specific area in the brain also has profound effects. Deletion of NAMPT from a subset of hypothalamic neurons resulted in progressive

neuronal loss and produced significant changes to feeding behavior and energy expenditure in mice [94]. Knockout of NAMPT from the hippocampus resulted in significant neuron loss, especially in the CA1 region, and neurite degeneration. These knockout neurons have altered excitability profiles and decreased mitochondrial density [95, 96]. The importance of NAD^+ homeostasis and the salvage pathway to neurons has been well documented, but the recent findings demonstrating the effect that NAMPT deletion has on motor behavior, suggests that the NAD^+ salvage pathway may need to be further studied in relation to motor neuron diseases.

1.6 NAD^+ salvage and amyotrophic lateral sclerosis

ALS is a fatal neurological disorder, characterized by the progressive loss of motor neurons, limb weakness, and paralysis. In ALS, motor neurons in the brain, brainstem, and spinal cord degenerate, resulting in significant denervation of skeletal muscles and dysfunction of neuromuscular junctions (NMJs) [97]. ALS cases are separated into sporadic and familial, though there is no difference in the disease phenotype. Familial cases are result from mutations to specific genes, including *SOD1*, *TARDBP*, *FUS,* and *C9orf72* [98]. A specific cause of ALS remains unknown, though mitochondrial dysfunction, oxidative stress and neuroinflammation, along with other impairments, have been observed in ALS and are being investigated [99, 100]. NAD^+ homeostasis may be involved in development or progression of ALS because homeostasis is disrupted in ALS. NAM was reduced in the serum and CSF in human ALS patients [101]. In ALS mice, spinal cord NAD^+ was reduced around symptom on-set with the decline becoming worse, and occurring in other tissues, as ALS progressed [102, 103]. Overall, this suggests impairments to NAD^+ availability is important in ALS.

This is supported by evidence that the NAD^+ salvage pathway is altered in ALS. In ALS patient spinal cord samples, expression of NMNAT2 and NAMPT were significantly altered. Nmnat2 was decreased while total NAMPT was increased [48, 104]. Lower NMNAT levels in the spinal cord and skeletal muscle were also observed in ALS mice [102, 104, 105]. After further investigation, the NAMPT increase the extracellular form and that intracellular levels were reduced [48]. It is likely that the increase in NAMPT is not constant but the result of a disturbance in the circadian fluctuation in NAMPT expression. In ALS mice, peak NAMPT expression is shifted from the dark, or active, period to the light, or inactive, period [105]. As such, the time of tissue collection would be considerably important for assessing NAMPT expression.

The importance of NAMPT in ALS is becoming better understood. ALS mice treated with P7C3, a potential NAMPT activator, had greater motor neuron survival and motor performance [106]. Conversely, deleting NAMPT from motor neurons produced an ALS phenotype with similar motor and NMJ impairments, followed by hindlimb paralysis and death [48]. Beyond motor neurons, NAMPT could be involved in the non-cell autonomous nature of ALS. In ALS, astrocytes become neurotoxic and astrocytic NAMPT can counter this. NAMPT over-expression in astrocytes prevented motor neuron death potentially by improving oxidative stress response [107]. With NAMPT the rate-limiting enzyme in the salvage pathway, the benefits of NAD^+ intermediates that act downstream of NAMPT, such as NR and NMN, have been studied. NR or NMN improved motor behavior, motor neuron survival, glial cell activation, and lengthened lifespan in ALS mice and following NAMPT deletion from motor neurons [48, 103, 104]. Additionally, NMN and NR protected motor neurons from neurotoxic ALS astrocytes [108]. Gene expression

is also impacted by NAD^+ precursors, with NR or NMN positively affecting expression of antioxidant defense and denervation marker genes [104, 108]. While NAD^+ precursor metabolites are beneficial against ALS, further investigation is needed. Specifically, how NMJs, one of the most vulnerable and earliest affected sites in ALS, are affected by NAD^+ precursor metabolites is not known.

NAD^+ consuming enzymes have also been linked to ALS. Multiple SIRTs have been found to be beneficial against ALS. SIRT1 over-expression or activators improved motor neuron survival, NMJ innervation, and lifespan [109, 110]. SIRT3 and SIRT6 are necessary for NAD^+ supplementation to prevent motor neuron death from ALS astrocytes and SIRT6 expression is reduced in ALS patients [107, 108]. Additionally, pairing a SIRT activator with an NAD^+ precursor metabolite enhanced the protective effects [103]. While SIRT activity is generally positive against ALS, PARP activity is more negative. ALS patient spinal cords have higher levels of PAR [111]. PARP1 inhibition of knockdown prevented TDP-43 neurotoxicity, possibly by inhibiting formation of protein aggregates [111, 112].

Due to being critical for axonal degeneration, SARM1 has been studied for a role in ALS development and progression. The benefits of SARM1 deletion may depend on the cause of ALS. SARM1 knockout in $SOD1^{G93A}$ ALS models did not affect motor neuron survival or skeletal muscle innervation whereas loss of SARM1 in TDP-43 ALS models exhibited increased motor neuron number and innervation. Unfortunately, SARM1 knockout did not improve motor function or survival in that TDP-43 model [113-116]. NAD^+ was not measured in these studies, however, and would have provided insight into whether SARM1 deletion can increase NAD^+ levels. Recently, unique gain-of-function

mutations in SARM1 were found to be more common in ALS patients compared to healthy subjects. These mutations cause increased SARM1 activity and reduce NAD^+ levels in neurons while making them more vulnerable to oxidative stress [117]. Additionally, a constitutively active SARM1 mutant in neurons can cause motor dysfunction [118]. These recent findings suggest that SARM1 mutations may not cause ALS to develop but may contribute to ALS development and the NAD^+ decline. Overall, while increasing evidence indicates NAD^+ homeostasis is impaired in ALS and administering NAD^+ precursor molecules is beneficial, there has not been an investigation into how ALS NMJs are affected from NAD^+ precursors.

1.7 Outline for dissertation

As mentioned in the preceding chapter, disrupting the NAD^+ salvage pathway in neurons can produce motor deficiencies and neurodegeneration. Also, many neurodegenerative diseases exhibit impairments to NAD^+ homeostasis. For my dissertation, the projects described in Chapters 2-4 sought to investigate the impact of the NAD^+ salvage pathway on NMJ function and metabolic homeostasis in the motor system. In Chapter 2, using an inducible projection-neuron specific NAMPT knockout mouse [48], I investigated the effects on the function and structure of NMJs and skeletal muscle mitochondrial morphology after loss of NAMPT. For this, I primarily used the fluorescent dye FM1-43 which labels synaptic vesicles and can be used to visualize endocytosis and exocytosis. For Chapter 3, again utilizing this inducible projection-neuron specific NAMPT knockout mouse, I described the bioenergetic and signaling pathway alterations that occur in the motor cortex following NAMPT deletion using metabolomics and transcriptomics. Lastly, in Chapter 4, I studied how supplementing the diets of $SOD1^{G93A}$

mice, an ALS model, with NMN influences motor behavior, NMJ function, and mitochondrial morphology. My study may improve our understanding of the broad (motor behavior & bioenergetics) and localized (NMJ function) effects caused by disruption of the NAD^+ salvage pathway in ALS and other diseases. Given that NAD^+ homeostasis is impaired in many neurodegenerative diseases, our results may help us learn how NAD^+ supplementation is beneficial in protecting against diseases.

1.8 References

1. Katsyuba, E., et al., *NAD(+) homeostasis in health and disease.* Nat Metab, 2020. **2**(1): p. 9-31.
2. Lautrup, S., et al., *NAD(+) in Brain Aging and Neurodegenerative Disorders.* Cell Metab, 2019. **30**(4): p. 630-655.
3. Mendelsohn, A.R. and J.W. Larrick, *The NAD+/PARP1/SIRT1 Axis in Aging.* Rejuvenation Res, 2017. **20**(3): p. 244-247.
4. Levine, D.C., et al., *NAD(+) Controls Circadian Reprogramming through PER2 Nuclear Translocation to Counter Aging.* Mol Cell, 2020. **78**(5): p. 835-849 e7.
5. Kataura, T., et al., *Autophagy promotes cell survival by maintaining NAD levels.* Dev Cell, 2022. **57**(22): p. 2584-2598 e11.
6. Liu, L., et al., *Quantitative Analysis of NAD Synthesis-Breakdown Fluxes.* Cell Metab, 2018. **27**(5): p. 1067-1080 e5.
7. Nakahata, Y., et al., *Circadian control of the NAD+ salvage pathway by CLOCK-SIRT1.* Science, 2009. **324**(5927): p. 654-7.
8. Ramsey, K.M., et al., *Circadian clock feedback cycle through NAMPT-mediated NAD+ biosynthesis.* Science, 2009. **324**(5927): p. 651-4.
9. McReynolds, M.R., et al., *NAD(+) flux is maintained in aged mice despite lower tissue concentrations.* Cell Syst, 2021. **12**(12): p. 1160-1172 e4.
10. Cambronne, X.A., et al., *Biosensor reveals multiple sources for mitochondrial NAD(+).* Science, 2016. **352**(6292): p. 1474-7.

11. Berger, F., et al., *Subcellular compartmentation and differential catalytic properties of the three human nicotinamide mononucleotide adenylyltransferase isoforms.* J Biol Chem, 2005. **280**(43): p. 36334-41.

12. Rajman, L., K. Chwalek, and D.A. Sinclair, *Therapeutic Potential of NAD-Boosting Molecules: The In Vivo Evidence.* Cell Metab, 2018. **27**(3): p. 529-547.

13. Canto, C., K.J. Menzies, and J. Auwerx, *NAD(+) Metabolism and the Control of Energy Homeostasis: A Balancing Act between Mitochondria and the Nucleus.* Cell Metab, 2015. **22**(1): p. 31-53.

14. Verdin, E., *NAD(+) in aging, metabolism, and neurodegeneration.* Science, 2015. **350**(6265): p. 1208-13.

15. Fujigaki, H., Y. Yamamoto, and K. Saito, *L-Tryptophan-kynurenine pathway enzymes are therapeutic target for neuropsychiatric diseases: Focus on cell type differences.* Neuropharmacology, 2017. **112**(Pt B): p. 264-274.

16. Rongvaux, A., et al., *Reconstructing eukaryotic NAD metabolism.* Bioessays, 2003. **25**(7): p. 683-90.

17. Bogan, K.L. and C. Brenner, *Nicotinic acid, nicotinamide, and nicotinamide riboside: a molecular evaluation of NAD+ precursor vitamins in human nutrition.* Annu Rev Nutr, 2008. **28**(1): p. 115-30.

18. Mori, V., et al., *Metabolic profiling of alternative NAD biosynthetic routes in mouse tissues.* PLoS One, 2014. **9**(11): p. e113939.

19. Revollo, J.R., A.A. Grimm, and S. Imai, *The NAD biosynthesis pathway mediated by nicotinamide phosphoribosyltransferase regulates Sir2 activity in mammalian cells.* J Biol Chem, 2004. **279**(49): p. 50754-63.

20. Katsyuba, E. and J. Auwerx, *Modulating NAD(+) metabolism, from bench to bedside.* EMBO J, 2017. **36**(18): p. 2670-2683.

21. Bieganowski, P. and C. Brenner, *Discoveries of Nicotinamide Riboside as a Nutrient and Conserved NRK Genes Establish a Preiss-Handler Independent Route to NAD+ in Fungi and Humans.* Cell, 2004. **117**(4): p. 495-502.

22. Fletcher, R.S., et al., *Nicotinamide riboside kinases display redundancy in mediating nicotinamide mononucleotide and nicotinamide riboside metabolism in skeletal muscle cells.* Mol Metab, 2017. **6**(8): p. 819-832.

23. Wu, Q.J., et al., *The sirtuin family in health and disease.* Signal Transduct Target Ther, 2022. **7**(1): p. 402.

24. Canto, C., et al., *AMPK regulates energy expenditure by modulating NAD+ metabolism and SIRT1 activity.* Nature, 2009. **458**(7241): p. 1056-60.

25. Kawahara, T.L., et al., *SIRT6 links histone H3 lysine 9 deacetylation to NF-kappaB-dependent gene expression and organismal life span.* Cell, 2009. **136**(1): p. 62-74.

26. Wang, Q., et al., *SIRT3 protects cells from hypoxia via PGC-1alpha- and MnSOD-dependent pathways.* Neuroscience, 2015. **286**: p. 109-21.

27. Yang, X., et al., *The Role and Mechanism of SIRT1 in Resveratrol-regulated Osteoblast Autophagy in Osteoporosis Rats.* Sci Rep, 2019. **9**(1): p. 18424.

28. Stuart, J.A., et al., *Hypoxia inducible factors as mediators of reactive oxygen/nitrogen species homeostasis in physiological normoxia.* Med Hypotheses, 2019. **129**: p. 109249.

29. Mouchiroud, L., et al., *The NAD(+)/Sirtuin Pathway Modulates Longevity through Activation of Mitochondrial UPR and FOXO Signaling.* Cell, 2013. **154**(2): p. 430-41.

30. Roichman, A., et al., *Restoration of energy homeostasis by SIRT6 extends healthy lifespan.* Nat Commun, 2021. **12**(1): p. 3208.

31. Fang, E.F., et al., *NAD(+) in Aging: Molecular Mechanisms and Translational Implications.* Trends Mol Med, 2017. **23**(10): p. 899-916.

32. Bai, P. and C. Canto, *The role of PARP-1 and PARP-2 enzymes in metabolic regulation and disease.* Cell Metab, 2012. **16**(3): p. 290-5.

33. Krishnakumar, R. and W.L. Kraus, *The PARP side of the nucleus: molecular actions, physiological outcomes, and clinical targets.* Mol Cell, 2010. **39**(1): p. 8-24.

34. Garten, A., et al., *Physiological and pathophysiological roles of NAMPT and NAD metabolism.* Nat Rev Endocrinol, 2015. **11**(9): p. 535-46.

35. Higashida, H., et al., *An immunohistochemical, enzymatic, and behavioral study of CD157/BST-1 as a neuroregulator.* BMC Neurosci, 2017. **18**(1): p. 35.

36. Aksoy, P., et al., *Regulation of intracellular levels of NAD: a novel role for CD38.* Biochem Biophys Res Commun, 2006. **345**(4): p. 1386-92.

37. Camacho-Pereira, J., et al., *CD38 Dictates Age-Related NAD Decline and Mitochondrial Dysfunction through an SIRT3-Dependent Mechanism.* Cell Metab, 2016. **23**(6): p. 1127-1139.

38. Essuman, K., et al., *The SARM1 Toll/Interleukin-1 Receptor Domain Possesses Intrinsic NAD(+) Cleavage Activity that Promotes Pathological Axonal Degeneration.* Neuron, 2017. **93**(6): p. 1334-1343 e5.

39. Loreto, A., et al., *Mitochondrial impairment activates the Wallerian pathway through depletion of NMNAT2 leading to SARM1-dependent axon degeneration.* Neurobiol Dis, 2020. **134**: p. 104678.

40. Loreto, A., et al., *Wallerian Degeneration Is Executed by an NMN-SARM1-Dependent Late Ca(2+) Influx but Only Modestly Influenced by Mitochondria.* Cell Rep, 2015. **13**(11): p. 2539-2552.

41. Zhang, W., et al., *Neuronal protective role of PBEF in a mouse model of cerebral ischemia.* J Cereb Blood Flow Metab, 2010. **30**(12): p. 1962-71.

42. Samal, B., et al., *Cloning and characterization of the cDNA encoding a novel human pre-B-cell colony-enhancing factor.* Mol Cell Biol, 1994. **14**(2): p. 1431-7.

43. Revollo, J.R., et al., *Nampt/PBEF/Visfatin regulates insulin secretion in beta cells as a systemic NAD biosynthetic enzyme.* Cell Metab, 2007. **6**(5): p. 363-75.

44. Yoshida, M., et al., *Extracellular Vesicle-Contained eNAMPT Delays Aging and Extends Lifespan in Mice.* Cell Metab, 2019. **30**(2): p. 329-342 e5.

45. Zhang, L.Q., et al., *Metabolic and molecular insights into an essential role of nicotinamide phosphoribosyltransferase.* Cell Death Dis, 2017. **8**(3): p. e2705.

46. Wang, D.X., et al., *Hepatic Nampt Deficiency Aggravates Dyslipidemia and Fatty Liver in High Fat Diet Fed Mice.* Cells, 2023. **12**(4): p. 568.

47. Frederick, D.W., et al., *Loss of NAD Homeostasis Leads to Progressive and Reversible Degeneration of Skeletal Muscle.* Cell Metab, 2016. **24**(2): p. 269-82.

48. Wang, X., et al., *Deletion of Nampt in Projection Neurons of Adult Mice Leads to Motor Dysfunction, Neurodegeneration, and Death.* Cell Rep, 2017. **20**(9): p. 2184-2200.

49. Sasaki, Y., et al., *Dysregulation of NAD(+) Metabolism Induces a Schwann Cell Dedifferentiation Program.* J Neurosci, 2018. **38**(29): p. 6546-6562.

50. Stromsdorfer, K.L., et al., *NAMPT-Mediated NAD(+) Biosynthesis in Adipocytes Regulates Adipose Tissue Function and Multi-organ Insulin Sensitivity in Mice.* Cell Rep, 2016. **16**(7): p. 1851-60.

51. Yamaguchi, S., et al., *Adipose tissue NAD(+) biosynthesis is required for regulating adaptive thermogenesis and whole-body energy homeostasis in mice.* Proc Natl Acad Sci U S A, 2019. **116**(47): p. 23822-23828.

52. Muraoka, H., et al., *Role of Nampt-Sirt6 Axis in Renal Proximal Tubules in Extracellular Matrix Deposition in Diabetic Nephropathy.* Cell Rep, 2019. **27**(1): p. 199-212 e5.

53. Bermudez, B., et al., *Leukocyte Overexpression of Intracellular NAMPT Attenuates Atherosclerosis by Regulating PPARgamma-Dependent Monocyte Differentiation and Function.* Arterioscler Thromb Vasc Biol, 2017. **37**(6): p. 1157-1167.

54. Costford, S.R., et al., *Skeletal muscle overexpression of nicotinamide phosphoribosyl transferase in mice coupled with voluntary exercise augments exercise endurance.* Mol Metab, 2018. **7**: p. 1-11.

55. Jing, Z., et al., *Neuronal NAMPT is released after cerebral ischemia and protects against white matter injury.* J Cereb Blood Flow Metab, 2014. **34**(10): p. 1613-21.

56. Xiong, X., et al., *NAMPT overexpression alleviates alcohol-induced hepatic steatosis in mice.* PLoS One, 2019. **14**(2): p. e0212523.

57. Hsu, C.P., et al., *Nicotinamide phosphoribosyltransferase regulates cell survival through NAD+ synthesis in cardiac myocytes.* Circ Res, 2009. **105**(5): p. 481-91.

58. Conforti, L., et al., *Reducing expression of NAD+ synthesizing enzyme NMNAT1 does not affect the rate of Wallerian degeneration.* FEBS J, 2011. **278**(15): p. 2666-79.

59. Hicks, A.N., et al., *Nicotinamide mononucleotide adenylyltransferase 2 (Nmnat2) regulates axon integrity in the mouse embryo.* PLoS One, 2012. **7**(10): p. e47869.

60. Yamamoto, M., et al., *Nmnat3 Is Dispensable in Mitochondrial NAD Level Maintenance In Vivo.* PLoS One, 2016. **11**(1): p. e0147037.

61. Yan, T., et al., *Nmnat2 delays axon degeneration in superior cervical ganglia dependent on its NAD synthesis activity.* Neurochem Int, 2010. **56**(1): p. 101-6.

62. Yahata, N., S. Yuasa, and T. Araki, *Nicotinamide mononucleotide adenylyltransferase expression in mitochondrial matrix delays Wallerian degeneration.* J Neurosci, 2009. **29**(19): p. 6276-84.

63. Tang, B.L., *Why is NMNAT Protective against Neuronal Cell Death and Axon Degeneration, but Inhibitory of Axon Regeneration?* Cells, 2019. **8**(3): p. 267.

64. Carbone, F., et al., *Regulation and Function of Extracellular Nicotinamide Phosphoribosyltransferase/Visfatin.* Compr Physiol, 2017. **7**(2): p. 603-621.

65. Pinkerton, M., et al., *Salvage NAD+ biosynthetic pathway enzymes moonlight as molecular chaperones to protect against proteotoxicity.* Human Molecular Genetics, 2021. **30**(8): p. 672-686.

66. Zhai, R.G., et al., *NAD synthase NMNAT acts as a chaperone to protect against neurodegeneration.* Nature, 2008. **452**(7189): p. 887-91.

67. Huang, C., et al., *The mouse nicotinamide mononucleotide adenylyltransferase chaperones diverse pathological amyloid client proteins.* J Biol Chem, 2022. **298**(5): p. 101912.

68. Zhu, Y., et al., *Nmnat restores neuronal integrity by neutralizing mutant Huntingtin aggregate-induced progressive toxicity.* Proc Natl Acad Sci U S A, 2019. **116**(38): p. 19165-19175.

69. Ma, X., et al., *Nicotinamide mononucleotide adenylyltransferase uses its NAD(+) substrate-binding site to chaperone phosphorylated Tau.* Elife, 2020. **9**: p. e51859.

70. Zang, S., et al., *Nicotinamide mononucleotide adenylyltransferase maintains active zone structure by stabilizing Bruchpilot.* EMBO Rep, 2013. **14**(1): p. 87-94.

71. Russo, A., et al., *The E3 ligase Highwire promotes synaptic transmission by targeting the NAD-synthesizing enzyme dNmnat.* EMBO Rep, 2019. **20**(3): p. e46975.

72. Xiao, W., et al., *NAD(H) and NADP(H) Redox Couples and Cellular Energy Metabolism.* Antioxid Redox Signal, 2018. **28**(3): p. 251-272.

73. Xie, N., et al., *NAD(+) metabolism: pathophysiologic mechanisms and therapeutic potential.* Signal Transduct Target Ther, 2020. **5**(1): p. 227.

74. Yoon, M.J., et al., *SIRT1-Mediated eNAMPT Secretion from Adipose Tissue Regulates Hypothalamic NAD+ and Function in Mice.* Cell Metab, 2015. **21**(5): p. 706-17.

75. Park, J.W., et al., *Circulating blood eNAMPT drives the circadian rhythms in locomotor activity and energy expenditure.* Nat Commun, 2023. **14**(1): p. 1994.

76. Zhu, X.H., et al., *In vivo NAD assay reveals the intracellular NAD contents and redox state in healthy human brain and their age dependences.* Proc Natl Acad Sci U S A, 2015. **112**(9): p. 2876-81.

77. Zha, S., et al., *PARP1 inhibitor (PJ34) improves the function of aging-induced endothelial progenitor cells by preserving intracellular NAD(+) levels and increasing SIRT1 activity.* Stem Cell Res Ther, 2018. **9**(1): p. 224.

78. Yoshino, J., et al., *Nicotinamide mononucleotide, a key NAD(+) intermediate, treats the pathophysiology of diet- and age-induced diabetes in mice.* Cell Metab, 2011. **14**(4): p. 528-36.

79. Yang, L., et al., *Nicotine rebalances NAD(+) homeostasis and improves aging-related symptoms in male mice by enhancing NAMPT activity.* Nat Commun, 2023. **14**(1): p. 900.

80. Yoshino, J., J.A. Baur, and S.I. Imai, *NAD(+) Intermediates: The Biology and Therapeutic Potential of NMN and NR.* Cell Metab, 2018. **27**(3): p. 513-528.

81. Covarrubias, A.J., et al., *NAD(+) metabolism and its roles in cellular processes during ageing.* Nat Rev Mol Cell Biol, 2021. **22**(2): p. 119-141.

82. Mills, K.F., et al., *Long-Term Administration of Nicotinamide Mononucleotide Mitigates Age-Associated Physiological Decline in Mice.* Cell Metab, 2016. **24**(6): p. 795-806.

83. Xing, S., et al., *Nicotinamide phosphoribosyltransferaserelated signaling pathway in early Alzheimer's disease mouse models.* Mol Med Rep, 2019. **20**(6): p. 5163-5171.

84. Ghosh, D., K.R. Levault, and G.J. Brewer, *Relative importance of redox buffers GSH and NAD(P)H in age-related neurodegeneration and Alzheimer disease-like mouse neurons.* Aging Cell, 2014. **13**(4): p. 631-40.

85. Zou, X.D., et al., *NAMPT protects against 6-hydroxydopamine-induced neurotoxicity in PC12 cells through modulating SIRT1 activity.* Mol Med Rep, 2016. **13**(5): p. 4058-64.

86. Lu, L., et al., *Nicotinamide mononucleotide improves energy activity and survival rate in an in vitro model of Parkinson's disease.* Exp Ther Med, 2014. **8**(3): p. 943-950.

87. Raff, M.C., A.V. Whitmore, and J.T. Finn, *Axonal self-destruction and neurodegeneration.* Science, 2002. **296**(5569): p. 868-71.

88. Wang, J., et al., *A local mechanism mediates NAD-dependent protection of axon degeneration.* J Cell Biol, 2005. **170**(3): p. 349-55.

89. Osterloh, J.M., et al., *dSarm/Sarm1 is required for activation of an injury-induced axon death pathway.* Science, 2012. **337**(6093): p. 481-4.

90. Figley, M.D., et al., *SARM1 is a metabolic sensor activated by an increased NMN/NAD(+) ratio to trigger axon degeneration.* Neuron, 2021. **109**(7): p. 1118-1136 e11.

91. Gilley, J. and M.P. Coleman, *Endogenous Nmnat2 is an essential survival factor for maintenance of healthy axons.* PLoS Biol, 2010. **8**(1): p. e1000300.

92. Milde, S., J. Gilley, and M.P. Coleman, *Subcellular localization determines the stability and axon protective capacity of axon survival factor Nmnat2.* PLoS Biol, 2013. **11**(4): p. e1001539.

93. Wang, X., H. Li, and S. Ding, *Pre-B-cell colony-enhancing factor protects against apoptotic neuronal death and mitochondrial damage in ischemia.* Sci Rep, 2016. **6**: p. 32416.

94. de Guia, R.M., et al., *Ablation of Nampt in AgRP neurons leads to neurodegeneration and impairs fasting- and ghrelin-mediated food intake.* FASEB J, 2021. **35**(5): p. e21450.

95. Stein, L.R., et al., *Expression of Nampt in hippocampal and cortical excitatory neurons is critical for cognitive function.* J Neurosci, 2014. **34**(17): p. 5800-15.

96. Shen, C., et al., *The Depletion of NAMPT Disturbs Mitochondrial Homeostasis and Causes Neuronal Degeneration in Mouse Hippocampus.* Mol Neurobiol, 2023. **60**(3): p. 1267-1280.

97. Verma, S., et al., *Neuromuscular Junction Dysfunction in Amyotrophic Lateral Sclerosis.* Mol Neurobiol, 2022. **59**(3): p. 1502-1527.

98. Taylor, J.P., R.H. Brown, Jr., and D.W. Cleveland, *Decoding ALS: from genes to mechanism.* Nature, 2016. **539**(7628): p. 197-206.

99. Pandya, V.A. and R. Patani, *Decoding the relationship between ageing and amyotrophic lateral sclerosis: a cellular perspective.* Brain, 2020. **143**(4): p. 1057-1072.

100. Cappello, V. and M. Francolini, *Neuromuscular Junction Dismantling in Amyotrophic Lateral Sclerosis.* Int J Mol Sci, 2017. **18**(10).

101. Blacher, E., et al., *Potential roles of gut microbiome and metabolites in modulating ALS in mice.* Nature, 2019. **572**(7770): p. 474-480.

102. Roderer, P., et al., *Increased ROS Level in Spinal Cord of Wobbler Mice due to Nmnat2 Downregulation.* Mol Neurobiol, 2018. **55**(11): p. 8414-8424.

103. Obrador, E., et al., *Nicotinamide Riboside and Pterostilbene Cooperatively Delay Motor Neuron Failure in ALS SOD1(G93A) Mice.* Mol Neurobiol, 2021. **58**(4): p. 1345-1371.

104. Harlan, B.A., et al., *Evaluation of the NAD(+) biosynthetic pathway in ALS patients and effect of modulating NAD(+) levels in hSOD1-linked ALS mouse models.* Exp Neurol, 2020. **327**: p. 113219.

105. Killoy, K.M., et al., *Altered expression of clock and clock-controlled genes in a hSOD1-linked amyotrophic lateral sclerosis mouse model.* FASEB J, 2021. **35**(2): p. e21343.

106. Tesla, R., et al., *Neuroprotective efficacy of aminopropyl carbazoles in a mouse model of amyotrophic lateral sclerosis.* Proc Natl Acad Sci U S A, 2012. **109**(42): p. 17016-21.

107. Harlan, B.A., et al., *Enhancing NAD+ Salvage Pathway Reverts the Toxicity of Primary Astrocytes Expressing Amyotrophic Lateral Sclerosis-linked Mutant Superoxide Dismutase 1 (SOD1).* J Biol Chem, 2016. **291**(20): p. 10836-46.

108. Harlan, B.A., et al., *Enhanced SIRT6 activity abrogates the neurotoxic phenotype of astrocytes expressing ALS-linked mutant SOD1.* FASEB J, 2019. **33**(6): p. 7084-7091.

109. Mancuso, R., et al., *Resveratrol improves motoneuron function and extends survival in SOD1(G93A) ALS mice.* Neurotherapeutics, 2014. **11**(2): p. 419-32.

110. Herskovits, A.Z., et al., *SIRT1 deacetylase in aging-induced neuromuscular degeneration and amyotrophic lateral sclerosis.* Aging Cell, 2018. **17**(6): p. e12839.

111. McGurk, L., et al., *Nuclear poly(ADP-ribose) activity is a therapeutic target in amyotrophic lateral sclerosis.* Acta Neuropathol Commun, 2018. **6**(1): p. 84.

112. Duan, Y., et al., *PARylation regulates stress granule dynamics, phase separation, and neurotoxicity of disease-related RNA-binding proteins.* Cell Res, 2019. **29**(3): p. 233-247.

113. Peters, O.M., et al., *Loss of Sarm1 does not suppress motor neuron degeneration in the SOD1G93A mouse model of amyotrophic lateral sclerosis.* Hum Mol Genet, 2018. **27**(21): p. 3761-3771.

114. Collins, J.M., et al., *Sarm1 knockout modifies biomarkers of neurodegeneration and spinal cord circuitry but not disease progression in the mSOD1(G93A) mouse model of ALS.* Neurobiol Dis, 2022. **172**: p. 105821.

115. Veriepe, J., L. Fossouo, and J.A. Parker, *Neurodegeneration in C. elegans models of ALS requires TIR-1/Sarm1 immune pathway activation in neurons.* Nat Commun, 2015. **6**(1): p. 7319.

116. White, M.A., et al., *Sarm1 deletion suppresses TDP-43-linked motor neuron degeneration and cortical spine loss.* Acta Neuropathol Commun, 2019. **7**(1): p. 166.

117. Gilley, J., et al., *Enrichment of SARM1 alleles encoding variants with constitutively hyperactive NADase in patients with ALS and other motor nerve disorders.* medRxiv, 2021: p. 2021.06.17.21258268.

118. Bloom, A.J., et al., *Constitutively active SARM1 variants found in ALS patients induce neuropathy.* bioRxiv, 2021: p. 2021.04.16.439886.

Chapter two: The effect of NAMPT deletion in projection neurons on the function and structure of neuromuscular junctions (NMJ) in mice

2.1 Abstract

Nicotinamide adenine dinucleotide (NAD^+) plays a critical role in energy metabolism. Most NAD^+ in mammalian cells is synthesized via the NAD^+ salvage pathway, where nicotinamide phosphoribosyltransferase (NAMPT) is the rate-limiting enzyme, converting nicotinamide into nicotinamide mononucleotide (NMN). Using a Thy1-Nampt$^{-/-}$ projection neuron conditional knockout (cKO) mouse, we studied the impact of NAMPT on synaptic vesicle cycling in the neuromuscular junction (NMJ), end-plate structure of NMJs and muscle contractility. Loss of NAMPT impaired synaptic vesicle cycling (endocytosis/exocytosis) in motor neurons. Morphological analysis indicated that the cKO mice also had motor endplates with significantly reduced area and thickness. When the cKO mice were treated with NMN, synaptic vesicle cycling was improved, and endplate morphology was restored. Muscle contraction was significantly impacted in Thy1-Nampt$^{-/-}$ cKO mice, with NMN-treated and untreated conditions responding similarly to low frequency stimulation. Relative to controls, untreated cKO mice demonstrated increased contraction strength as frequency was increased but NMN-treated cKO mice showed reduced strength. TEM revealed sarcomere misalignment and changes to mitochondrial morphology in semitendinosus muscles in cKO mice, with NMN treatment improving sarcomere alignment but not mitochondrial morphology. This study

demonstrates that neuronal NAMPT is important for both pre-synaptic and post-synaptic NMJ function and maintaining skeletal muscle structure and mitochondrial morphology.

2.2 Introduction

In chapter one, we described how NAMPT and the NAD salvage pathway are integral to cellular bioenergetics and that in disrupting NAD homeostasis produces many impairments. NAD homeostasis have also been increasingly linked with aging and aging related diseases. One of those diseases being ALS, which is the most common adult motor neuron disorder. Previously, we demonstrated how the conditional knockout of NAMPT from projection neurons produces significant motor impairments, similar to those observed in ALS. In chapter two we investigated whether this conditional knockout affected the synaptic vesicle cycling in the nerve terminal and structure of the NMJ and skeletal muscle.

Nicotinamide adenine dinucleotide (NAD^+) is found in all cells of the human body and is an important cofactor or co-substrate, used in numerous enzymatic processes including glycolysis, the tricarboxylic acid (TCA) cycle, oxidative phosphorylation, DNA repair, and protein deacetylation [44]. NAD^+ levels may be important for many aspects of health and aging, including cellular metabolism, sarcopenia, and neurodegeneration [45]. NAD^+ can be synthesized through multiple enzymatic pathways. One is a *de novo* pathway that begins with the amino acid tryptophan, while other pathways utilize different metabolites capable of being converted into NAD^+. In mammalian cells, the majority of NAD^+ is produced from metabolites entering the NAD^+ salvage pathway [46]. The rate limiting enzyme of the salvage pathway is nicotinamide phosphoribosyltransferase (NAMPT), converting nicotinamide into nicotinamide mononucleotide (NMN), which is subsequently synthesized into NAD^+ by nicotinamide mononucleotide adenylyltransferases (NMNATs) [47].

NAD^+ levels decline with age and in different diseases. However, administration of NAD^+ precursor molecules, such as NMN or nicotinamide riboside (NR), are effective at preventing or reversing many age- or disease-related declines [48-53]. NAD^+ and the NAD^+ salvage pathway are vitally important to the normal health and function of many different organs and tissues in the human body, with neurons and skeletal muscles being impacted greatly by changes to NAD^+ availability. In neuron cell cultures, increased NMNAT activity or NAD^+ pre-treatment could prevent axon degeneration following physical or chemical injury [54]. Overexpression of NAMPT is also able to delay axon degeneration following axotomy [55] and can elevate NAD^+ levels in neurons [21]. The protective effects of NAD^+ on neurons has not only been shown *in vitro*, mice administered NMN following an ischemic event had reduced neuronal death and prevented cognitive and motor impairment [56]. Knockout of NAMPT from Schwann cells, cells responsible for myelinating and providing metabolic support to peripheral axons, produces severe peripheral neuropathy and death but these problems can be attenuated when an NAD^+ precursor is provided [57]. There is also evidence indicating a possible therapeutic role for NAD^+. P7C3, an NAMPT enhancing compound, has been shown to be neuroprotective in stroke [58], Parkinson disease [59], and amyotrophic lateral sclerosis (ALS) rodent models [60].

Skeletal muscle is also affected by changes to NAD^+ biosynthesis. Energy production of skeletal myotubes is impaired following NAMPT inhibition [61]. Deletion of NAMPT from the tibialis anterior muscle in mice reduced NAD^+ availability and mitochondrial function [62]. Mice lacking NAMPT in skeletal muscles exhibited many impairments, including reduced muscle mass, twitch force, and respiratory capacity but

those problems were reversed when those mice were provided NR [52]. Mice over-expressing NAMPT in skeletal muscles had elevated NAD^+ and metabolite levels and showed improved exercise endurance capacity when allowed voluntary exercise [63]. NAD^+ supplementation has also been shown to be beneficial to skeletal muscle disorders. In mdx mice, a model of Duchene's muscular dystrophy, NR supplementation was able to reduce fibrosis and improve skeletal muscle function [50]. How neurons and skeletal muscles are individually affected by altering NAD^+ homeostasis has been well studied but what is less understood is how disruptions of the NAD^+ salvage pathway may impact where nerves and muscles interact, the neuromuscular junction (NMJ).

Our recent study showed that the knockout of NAMPT in projection neurons, using a Thy1-$NAMPT^{-/-}$ conditional knockout (cKO) mouse model, produced neurodegeneration, muscle atrophy, abnormal NMJs and, eventually, death. These symptoms are similar to those observed in ALS. When these cKO mice were administered NMN, these detrimental effects were ameliorated and lifespan was extended [64]. These results indicate a non-cell autonomous effect of neuronal NAMPT on skeletal muscle structure and function. In this study, using the same cKO mouse model, we further investigated the effects of neuronal NAMPT on the structure and function of NMJs and skeletal muscles. Using FM1-43 imaging, we found that loss of NAMPT disrupted the normal synaptic vesicle cycle and possibly prevented some vesicles from being released. We also found that the motor end-plate is smaller, flatter, and thinner. Muscle contractility was significantly impacted, with contractions ending more quickly at lower stimulation frequencies but contraction strength being increased as the stimulation frequency increases. Sarcomere alignment and mitochondrial morphology were also affected. To study whether

NAD^+ supplementation can prevent these alterations, we treated Thy1-$NAMPT^{-/-}$ cKO mice with NMN. Our results show that NMN treatment has beneficial effects on NMJ function of the cKO mice but is less helpful to skeletal muscles only.

2.3 Materials and methods

2.3.1 Mice housing and NAMPT deletion

Mice were maintained on a 12 h light:12 h dark cycle (lights on 7 am-7 pm) in our AAALAC-accredited animal facility at the University of Missouri. All experimental procedures were performed in accordance with the NIH Guide for the Care and Use of Laboratory Animals and approved by the University of Missouri Animal Care Quality Assurance Committee (#9444). Both male and female adult mice were used for this study. Generation of projection neuron-specific conditional knockout (*Thy1-YFP-Nampt*$^{-/-}$) mice was done following the same procedure as described in our previous publication [64]. Briefly, *Thy1-CreER*^{T2}*-YFP* mice (Jackson Laboratory) [65] were crossed with *Nampt*$^{f/f}$ mice [66] to obtain *Thy1-CreER*^{T2}*-YFP: Nampt*$^{f/f}$ double homozygous transgenic mice. Nampt was deleted by administration of tamoxifen (TAM), dissolved in sunflower oil, with a dose of 200 mg/kg bodyweight, via oral gavage, for 5 consecutive days. We designated *Thy1-YFP-Nampt*$^{-/-}$ mice for homozygous Nampt$^{-/-}$ cKO mice. Starting 10 days after the final TAM administration, *Thy1-YFP-Nampt*$^{-/-}$ mice were given a daily intraperitoneal injection of either 0.9% saline solution or NMN solution, with a dose of 400 mg/kg. Control mice were administered NMN daily for at least 16 days prior to sacrifice. Body weights were recorded at the same time daily.

2.3.2 Western blotting analysis

Western blotting was used to analyze NAMPT expression in the semitendinosus muscle following a protocol similar to what was used in a previous study [64]. Protein was extracted from muscles that had been dissected and immediately flash frozen using liquid nitrogen. Muscle tissues were dissolved in lysis buffer mixed with a protease inhibitor

(Pierce Biotechnology, Rockford, IL). And phosphatase inhibitor cocktails (Sigma). The homogenized tissue was centrifuged at 13,500 g at 4 °C for 20 minutes and supernatant was retained. BCA assay kit (Thermo Scientific) was used to test protein concentration. Equivalent amounts of protein from each sample were diluted with lysis buffer and boiled for 5 minutes. Samples were then subjected to electrophoresis in a 10% SDS-polyacrylamide gel at 100 mV for 110-120 minutes. Gels were then transferred to polyvinylidene fluoride membranes using mixed molecular weight function of Trans-Blot Turbo Transfer System (Bio-Rad). Membranes were blocked for 1 hour in 5% BSA in Tris-buffered saline containing (0.1%) Tween-20 (TBST). Membranes were then incubated overnight at 4 °C with mouse monoclonal anti-NAMPT antibody (1:1000, ALX-804-922-C100, Enzo Life Sciences). Monoclonal mouse anti-β-actin (1:5000, sc-47778, Santa Cruz) was used as a control for total protein. Membranes were exposed to Clarity™ Western ECL Substrate (Bio-Rad) and imaged with ChemiDoc™ XRS+. Precision Plus Protein™ Dual Color Standards (Bio-Rad) was used as the marker to evaluate the molecular size of protein bands.

2.3.3 NAD^+ measurement in skeletal muscle

NAD^+ levels were measured using a commercially available assay kit (E2ND-100, Bioassay Systems, CA). NMN was administered to mice via intraperitoneal injection for two consecutive days, with the mice being sacrificed one hour after the second injection. Non-injected mice were used as controls. Semitendinosus and gastrocnemius muscles were dissected from mice. Tissues (~5 mg) were placed into 1.5 mL tube with 100 µL extraction buffer and homogenized on ice. Extracts were heated to 60 °C fro 5 minutes and then 20 µL assay buffer and 100 µL of the opposite extraction buffer were added to neutralize the

extracts. Samples were mixed briefly and the centrifuged at 14,000 RPM for 5 minutes. The supernatant was retained and used for the NAD^+ enzymatic assay. Total NAD^+ level was expressed as pmol/mg tissue.

2.3.4 Imaging of synaptic vesicle cycling with FM1-43 dye

Vesicle cycling in semitendinosus muscle was studied by imaging change of FM1-43 fluorescence. FM1-43 is a styryl dye that capable of labeling synaptic vesicles undergoing endocytosis and exocytosis [67]. For isolation of semitendinosus muscles, mice were sacrificed between 21 and 28 days after the last TAM administration, and the semitendinosus muscles were rapidly isolated, taking care to leave the nerve attached intact. Muscles were placed in Tyrode's solution (140 mM NaCl, 5.6 mM KCl,1 mM $MgCl_2$, 2 mM $CaCl_2$, 1.8 mM Na_2HPO_4, 10 mM $NaHCO_3$, 5.5 mM glucose) receiving 95%O_2/5%CO_2 continuously. Excessive non-semitendinosus muscle, connective tissue, and fat were removed from the muscles and electrical stimulation was applied to the nerve to ensure the muscle was still contracting. Clean muscles were pinned flat in a recording dish with sylgard bottom and filled with Tyrode's solution receiving 95%O_2/5%CO_2 continuously.

The attached nerve was stimulated using a suction electrode to find minimum current for muscle contraction. Muscle was incubated with Alexa-555-conjugated α-bungarotoxin (α-BTX-555) (Sigma, 1.5:1000) to block contractions. After contractions stopped, the muscle was stimulated at twice the minimum current threshold (10 Hz, 10 ms delay, 6 ms duration; Grass S88 Stimulator). Time-lapse imaging of vesicle endocytosis was conducted with a speed of one frame/minute, for 30 minutes, in Tyrode's solution containing 12 μM FM1-43 fluorescent dye (Life Technologies, Cat. No. F35355). The

muscle was then washed twice with low Ca^{2+} Tyrode's solution (140 mM NaCl, 5.6 mM KCl,5 mM $MgCl_2$, 0.2 mM $CaCl_2$, 1.8 mM Na_2HPO_4, 10 mM $NaHCO_3$, 5.5 mM glucose) 5 minutes for each time. The first wash contained 10 μM ADVASEP^{TM}-7 (Sigma-Aldrich, A3723) to reduce background fluorescence. Time-lapse imaging for vesicle exocytosis was conducted with a speed of one frame/minute, for 25 minutes, while muscle was stimulated in Tyrode's solution.

Imaging was performed using a Nikon Eclipse FN1 fluorescent microscope with a 40x water immerse Olympus objective (LUMPlanFI/IR, NA/0.8). Images were acquired as stack files using a Photometric Cool SNAP EZ CCD camera controlled by Metaview software. Image analysis was performed using Metamorph software. Acquired stack images were aligned, and a region-of-interest was assigned to assess fluorescent intensity changes of the neuromuscular junction.

For imaging FM1-43 release for an extended period of time, all procedures were identical except for the length of the second stimulation period. The second stimulation time was increased from 25 minutes to 120 minutes. For the spontaneous FM1-43 uptake, all procedures were identical except no stimulation occurred. Following the incubation with FM1-43, he muscles used for spontaneous FM1-43 uptake were fixed with 3.7% paraformaldehyde and stored at -20^{o} C until the NMJs were imaged.

2.3.5 Motor endplate labelling and structural analysis

Isolated clean semitendinosus muscles were incubated with α-BTX-555 (1.5:1000) for 10-15 minutes, and then washed 3 times for 10 minutes each. Muscles were then covered with OCT compound and flash frozen in liquid nitrogen. Muscles were stored at -20^{o} C prior to cutting. Using a cryostat (Leica CM1900), cross-sections of semitendinosus

muscles were cut onto coated microscope glass slides with a thickness of 5 μm. Muscle slices were carefully washed with distilled water to remove OCT. Motor endplate images were taken using the same fluorescent microscope and camera as the FM1-43 imaging but with a lens of 60x Olympus objective (A 60, NA/0.80). Measurements of area, length, breadth, outer radius, inner radius, and average intensity were performed by Metamorph software. Depression depth, depression width, left thickness, right thickness, and bottom thickness were manually measured using the Single Line function in Metamorph.

2.3.6 Measurement of skeletal muscle contractile response

Mice were sacrificed between 21 and 28 days following the final TAM injection. The semitendinosus isolation procedure was the same as the FM1-43 staining. Muscle was pinned to a sylgard dish, with the wide end secured with a pin and the narrow end left free. A piece of string was used to connect the muscle to a force transducer (MLT500/A, ADInstruments). The string was looped around the narrow end of the muscle and pulled tight. The force transducer was moved parallel to and away from the muscle until the muscle was pulled tight. The force transducer was connected to an amplifier (PowerLab 4/25T, ADInstruments). The muscle was stimulated at 1, 5, 10, 20, 50, and 100 Hz using a Grass SD9 stimulator. Responses were recorded using LabChart software.

Muscle contraction parameters were assessed using LabChart. Rise time, *i.e.*, the time from the onset of the response after stimulation to the maximal response of contraction force. Amplitude was the difference between baseline and maximum contraction force. Fall time was the amount of time it took to return to baseline once stimulation was removed. Slope was calculated as the amount of force lost from when maximum contractile force

was reached until the point stimulation was ended, divided by the length of time from maximum contractile force until stimulation was removed (grams of force loss/second).

2.3.7 Transmission electron microscopy (TEM) of skeletal muscle

Semitendinosus muscles were isolated from Nampt$^{-/-}$ cKO, NMN-treated Nampt$^{-/-}$ cKO, and Nampt$^{f/f}$ mice 23 days after the final TAM administration. Excess non-semitendinosus muscle, connective tissue, and fat were removed. The muscles were cut into smaller sections, with only the sections that likely contained NMJs retained. Remaining sections were fixed in 100 mM sodium cacodylate buffer containing 2% paraformaldehyde and 2% glutaraldehyde (pH 7.35). Samples were left at room temperature for at least one hour and moved to 4°C for at least 23 hours. Fixed samples were washed with 100 mM sodium cacodylate buffer (pH 7.35) containing 130 mM sucrose. Secondary fixation was performed using 1% osmium tetroxide in cacodylate buffer using a Pelco Biowave (Ted Pella, Inc. Redding, California) operated at 100 Watts for 1 minute. Samples were incubated at 4° C for 1 hour, then rinsed with cacodylate buffer, followed with distilled water. En bloc staining was performed using 1% aqueous uranyl acetate and incubated at 4° C overnight, then rinsed with distilled water. A graded dehydration series (30%, 50%, 70%, 90%, 100%, 100%) was performed using ethanol at 4° C, transitioned to acetone. Dehydrated samples were then infiltrated with Epon resin for 24 hours at room temperature and polymerized at 60°C for 48-72 hours. Samples were cut into 85 nm thick longitudinal and transverse sections using an ultramicrotome (Ultracut UCT, Leica Microsystems, Germany) and a diamond knife (Diatome, Hatfield, PA). 2000X and 6000X images were acquired with a JEOL JEM 1400 transmission electron microscope (JEOL, Peabody, MA) at 80 kV (0.35 s exposure time) on a Gatan Ultrascan

1000 CCD (Gatan, Inc, Pleasanton, CA). Myofiber composition and mitochondria morphology (area, perimeter, circularity, and Feret's diameter) were assessed using ImageJ (NIH). Circularity is scored from 0 to 1, with a score of 1 reflecting a perfect circle and the score decreasing as the shape become elongated. Feret's diameter is the longest distance between any two points along the outlined area and can be referred to as caliper distance. These parameters have been used previous to characterize mitochondrial morphology in skeletal muscle [68].

2.3.8 Statistical analysis

Data expressed as mean ±standard error of the mean (SEM). Comparisons were made using unpaired Student's t-test or One-way ANOVA with Tukey post-test. Levels of significance set as *$p<0.05$, **$p<0.01$, and ***$p<0.001$. Statistical analyses were performed using OriginPro 8 and Excel.

2.4 Results

2.4.1 NAMPT deletion from projection neurons impairs synaptic vesicle endocytosis and exocytosis

Our previous study has shown that Nampt deletion in projection neurons of mice produced NMJ abnormalities and reduced synaptic transmission [64]. To further understand the phenomena induced by Nampt deletion, using FM1-43 imaging, we investigated if the endocytosis and exocytosis of synaptic vesicles, important for synaptic function, at the NMJs have also been changed in Nampt$^{-/-}$ cKO mice. We isolated the semitendinosus muscles from Nampt$^{f/f}$ control mice and Nampt$^{-/-}$ cKO mice treated for two weeks with either saline or NMN (400 mg/kg dose). We also isolated the semitendinosus muscles from Nampt$^{f/f}$ mice treated with NMN for 2 weeks as an additional control. Fig. 2.1A-B indicates the experimental timeline and illustration of FM1-43 imaging of NMJs. To study endocytosis and exocytosis, the isolated muscles were incubated with a fluorescent α-BTX to block contractions and loaded with FM1-43 for imaging of synaptic vesicle endocytosis (Fig. 2.1C-F). Once loaded with FM1-43, the muscles underwent a second period of stimulation, this time without FM1-43 in the extracellular solution. Time lapse imaging was conducted to track changes in FM1-43 fluorescence to study endocytosis and exocytosis in the same NMJs.

Fig. 2.1G-J shows fluorescent images of the NMJs at different times during stimulation with FM1-43. For all four conditions, the normalized FM1-43 fluorescence increased in the motor nerve terminals, indicating FM1-43 uptake (Fig. 2.1K). Our data show that Nampt$^{-/-}$ cKO mice had a slower FM1-43 uptake rate than Nampt$^{f/f}$ mice, while NMN-treatment could increase FM1-43 uptake in Nampt$^{-/-}$ cKO mice; NMN-treated Nampt$^{f/f}$ mice exhibit the fastest FM1-43 uptake rate. The total FM1-43 fluorescence

uptake in Nampt$^{-/-}$ cKO mice (247.4±40.0 a.u.) following 30 minutes of stimulation, was significantly reduced as compared with Nampt$^{f/f}$ mice (470.5 ±71.5 a.u.) (Fig. 2.1L). Treatment of Nampt$^{-/-}$ cKO mice with NMN significantly increased total FM1-43 fluorescence (445.8±63.1 a.u.) to a value similar to Nampt$^{f/f}$ mice, while treatment of Nampt$^{f/f}$ mice with NMN did not significantly increase in FM1-43 fluorescence (589.2 ±66.6 a.u.) (Fig. 2.1H). These results suggest that loss of NAMPT reduces the rate and amount of evoked endocytosis, while treatment of NMN can restore endocytosis.

Next, we studied the effect of Nampt deletion on exocytosis. Time-lapse imaging was conducted for 25 minutes with stimulation of nerve-muscle preparations that had been successfully loaded with FM1-43 in the previous stimulation period (Fig. 2.2A-D). All four conditions showed a reduction in FM1-43 fluorescence within the nerve terminal after stimulation (Fig 2.2E-H). The loss of NAMPT lead to a noticeable reduction in the rate of FM1-43 release, while NMN-treated Nampt$^{-/-}$ cKO mice had a similar rate of FM1-43 reduction to Nampt$^{f/f}$ mice treated with and without NMN (Fig. 2.2I). The total fluorescence reduction was also significantly lower in the Nampt$^{-/-}$ cKO mice (14.0±2.0 a.u.) compared to Nampt$^{f/f}$ mice (27.2±6.1 a.u.), while NMN-treatment restored exocytosis in Nampt$^{-/-}$ cKO (21.9±3.0 a.u.) mice (Fig. 2J). FM1-43 fluorescence reduction in Nampt$^{f/f}$, NMN-treated Nampt$^{f/f}$ (18.8±2.6 a.u.) and NMN-treated Nampt$^{-/-}$ cKO mice were not significantly different (Fig. 2.2J). These results indicate that loss of NAMPT in projection neurons significantly impairs evoked exocytosis, both in the rate and amount of vesicle release at NMJs, but NMN can largely prevent these impairments.

The differences in the FM1-43 fluorescence reduction after destaining stimulation led us to investigate why this impairment may be occurring. Specifically, whether the rate

of FM1-43 release was simply reduced in the Nampt$^{-/-}$ cKO mice or whether there was a problem in accessing a portion of FM1-43 loaded vesicles. To investigate this, we extended the destaining stimulation time from 25 to 120 minutes, while keeping the FM1-43 loading time the same. During the 120 minutes of destaining stimulation, the Nampt$^{-/-}$ cKO mice stopped decreasing in fluorescence around 30 minutes, while the Nampt$^{f/f}$ and NMN-treated Nampt$^{-/-}$ cKO mice continued to decrease until around 90 minutes (Fig. 2.2K). This suggests that the Nampt$^{-/-}$ cKO mice are unable to release certain vesicles that have been loaded with FM1-43 dye or have a reduced number of synaptic vesicles [64].

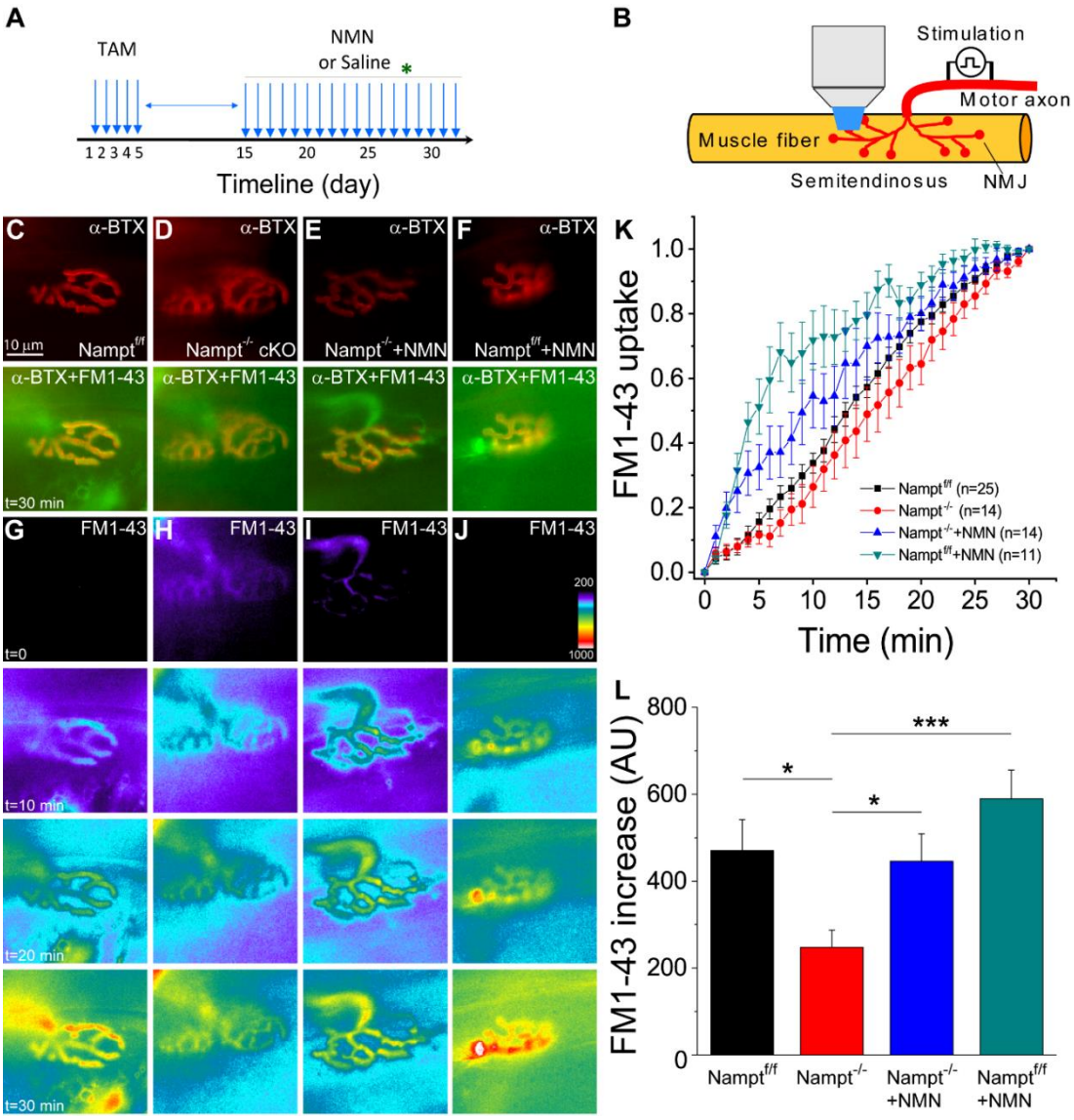

Figure 2.1. Impaired endocytosis in motor nerve terminal of Nampt$^{-/-}$ cKO mice. A) Experimental timeline. Star indicates the starting date of imaging. **B)** Illustration of FM1-43 imaging of NMJs. Motor axon is stimulated for staining and destaining of FM1-43. **C-F**) Motor endplates of Nampt$^{f/f}$ mice (C), Nampt$^{-/-}$ cKO mice (D), NMN-treated Nampt$^{-/-}$ cKO mice (E), and NMN-treated Nampt$^{f/f}$ mice (F). The top row shows images of nAChRs in NMJs labeled with α-BTX conjugated with Alexa 555, and the 2nd row shows the merged images of the same NMJs labeled with α-BTX and FM1-43. Nerve terminals were stained with FM1-43 dye and images were taken at speed of one frame/min after 30 minutes of stimulation with 10 Hz in the presence of the dye. **G-J**) Representative fluorescent images of FM1-43 uptake in nerve terminal before

stimulation, and 10, 20 and 30 min after stimulation. **K**) Normalized intensity of FM1-43 uptake in nerve terminals. Images were taken at speed of one frame/min during 30 min stimulation with 10 Hz in the presence of the FM1-43 dye. **L**) Mean fluorescence increase in nerve terminal for $Nampt^{f/f}$ (470.49±71, n=24), $Nampt^{-/-}$ cKO (247.35±40, n=16), NMN-treated $Nampt^{-/-}$ cKO (445.76±63, n=13.) mice, and NMN-treated $Nampt^{f/f}$ mice (589.18±67, n=11). Mean pixel intensity was calculated after 30 minutes of stimulation. n is the number of motor nerve terminals from 11-21 mice. *$p<0.05$, *** $p<0.001$, Student's t-test.

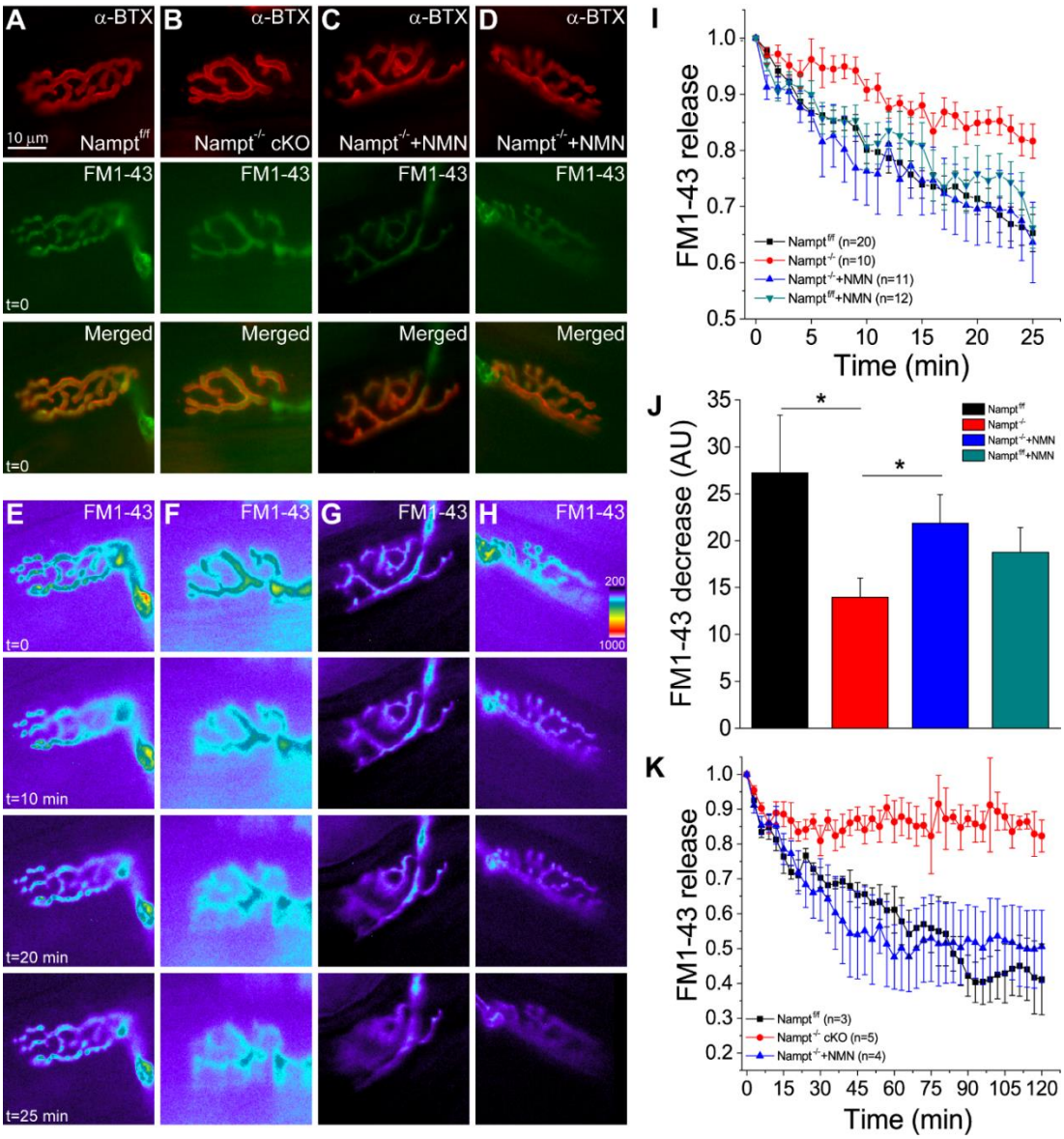

Figure 2.2. Impaired exocytosis from motor nerve terminal in Nampt$^{-/-}$ cKO mice. A-D) Motor endplates of Nampt$^{f/f}$ mice (A), Nampt$^{-/-}$ cKO and NMN-treated Nampt$^{-/-}$ cKO mice (B-C), and NMN-treated Nampt$^{f/f}$ mice (D). nAChRs were labeled with α-BTX conjugated with Alexa 555 (top row). Nerve terminal of the corresponding motor endplate in (A-D) stained with FM1-43 prior to destain stimulation (row second from top). Images taken prior to stimulation. Merged images of the NMJs in (A-C) labeled with α-BTX and FM1-43 (row third from top). **E-H**) Fluorescent imaging of FM1-43 release from nerve terminal before stimulation, and 10 minutes, 20 minutes and 25 minutes after stimulation. **I**) Normalized intensity of FM1-43 release from nerve terminal. Images taken every minute during the 25 minutes of stimulation. **J**) Mean fluorescence

decrease from nerve terminal for Nampt$^{f/f}$ (27.24±6, n=9), Nampt$^{-/-}$ cKO (13.96±2.0, n=11), and NMN-treated Nampt$^{-/-}$ cKO (20.22±3.20, n=10), and NMN-treated NAMPT$^{f/f}$ mice (18.77±2, n=12). Mean pixel intensities were calculated after 25 minutes of stimulation. **K**) Normalized intensity of FM1-43 release from nerve terminal. Image taken every three minutes during the 120 minutes of stimulation. n reflects the number of motor nerve terminals analyzed from 8-18 (**J**) and 3-4 (**K**) mice; *$p<0.05$, Student's t-test.

2.4.2 NAMPT and NAD^+ levels are not significantly changed in skeletal muscle

To determine whether the impairments of vesicle recycling is caused by the reduction of NAMPT levels in muscle, we used Western blotting to analyze whether $Nampt^{-/-}$ cKO mice had reduced NAMPT levels in semitendinosus muscles. Our results show that $Nampt^{-/-}$ cKO mice expressed similar intracellular NAMPT (iNAMPT) and extracellular NAMPT (eNAMPT) levels compared to the $Nampt^{f/f}$ control mice, furthermore, NMN administration did not affect iNAMPT and eNAMPT levels in the muscle (Fig. 2.3A-C). In addition, NMN administration did not increase NAD^+ levels in the semitendinosus and gastrocnemius muscles of control mice (Fig. 2.3D-E). These results are consistent with those in our previous study showing that deletion of Nampt in the projection neurons did not affect iNAMPT and eNAMPT levels in non-CNS organs [64]. These results also suggest that altered exocytosis and endocytosis in $Nampt^{-/-}$ cKO mice probably resulted from the long-term effect of neuronal Nampt deletion on NMJs. Since there were no significant changes in endocytosis, exocytosis, and NAD^+ level in muscle of the NMN-treated control mice, we only used three groups of mice, *i.e.*, $Nampt^{f/f}$ mice, $Nampt^{-/-}$ cKO mice, and $Nampt^{-/-}$ cKO mice treated with NMN for the rest of study.

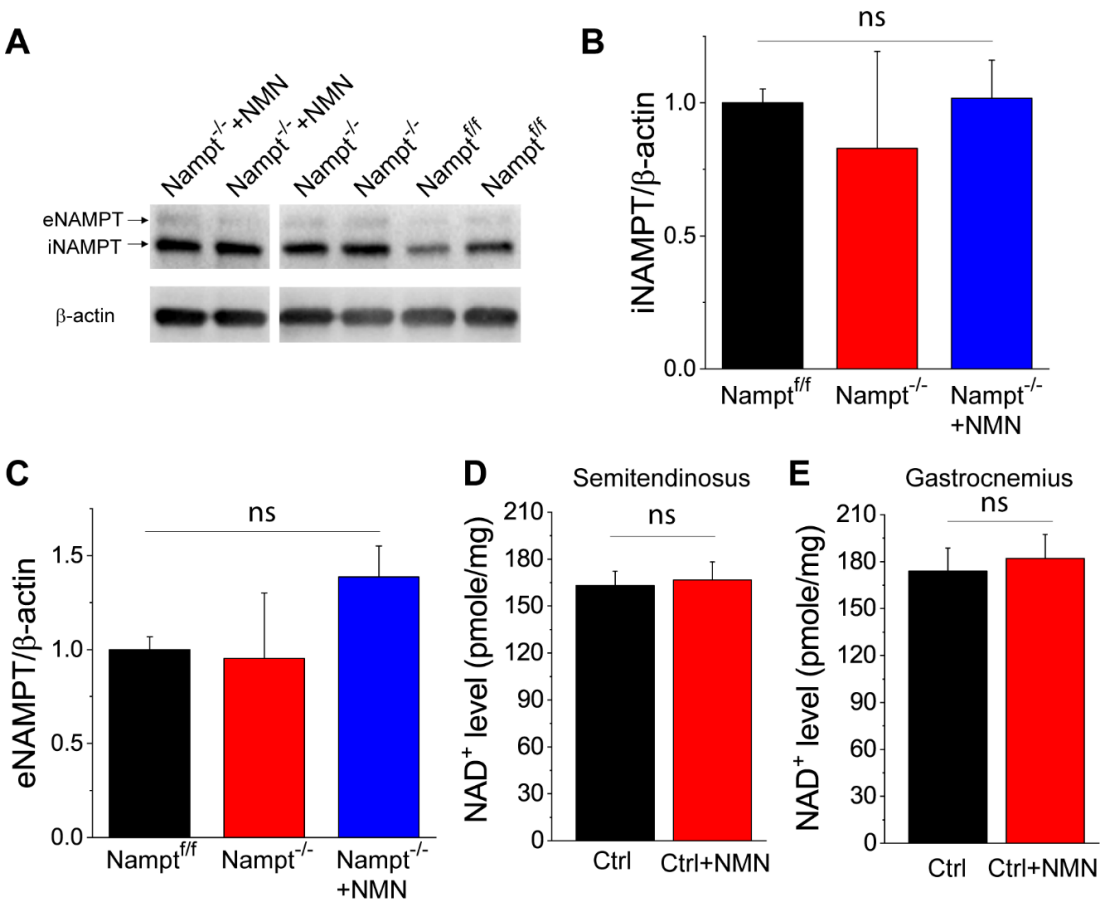

Figure 2.3. Western blot analysis of iNAMPT and eNAMPT and NAD$^+$ assay in the semitendinosus muscles. A-C) Western blot images (A) and summary data of iNAMPT (B) and eNAMPT (C) in the semitendinosus muscles of Nampt$^{f/f}$ mice, Thy1-Nampt$^{-/-}$ cKO mice and NMN-treated Thy1-Nampt$^{-/-}$ cKO mice. **D-E**) NAD$^+$ levels in semitendinosus and gastrocnemius muscles of control mice after NMN administration. Summary data in (B-D) were averaged values from N=4 mice for each group. ns, no significant difference, Student's t-test or ANOVA test.

2.4.3 Spontaneous synaptic vesicle endocytosis is not impacted by NAMPT deletion from projection neurons

The previous experiment provided evidence that the loss of NAMPT was detrimental to the stimulation-induced activity within the synaptic terminal, however, it is unknown whether spontaneous endocytosis may also be impacted after NAMPT deletion. To assess this, after staining with α-BTX, the muscle was incubated with FM1-43 for 30 minutes without stimulation and then fixed (Fig. 2.4A-C). The spontaneous fluorescence increase (Fig. 2.4D) did not significantly differ among the $Nampt^{f/f}$ (29.58±2.39 a.u.), $Nampt^{-/-}$ (30.00±2.88 a.u.) and NMN-treated $Nampt^{-/-}$ mice (29.93±2.92 a.u.).

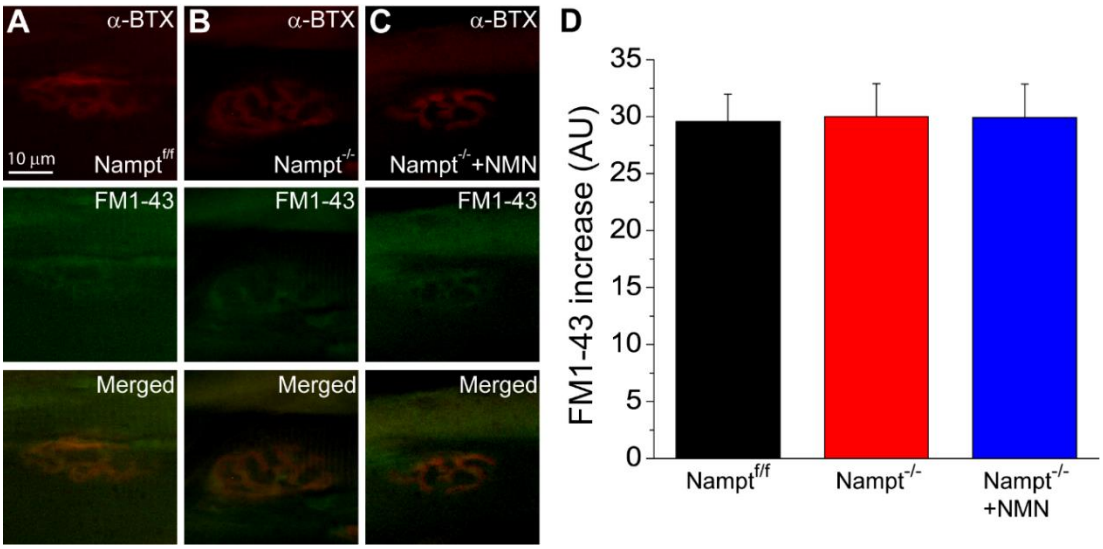

Figure 2.4. Spontaneous endocytosis in not altered in Nampt$^{-/-}$ cKO mice. A-C) Motor endplate and nerve terminal from Nampt$^{f/f}$ (A), Nampt$^{-/-}$ cKO and NMN-treated Nampt$^{-/-}$ cKO mice (B-C). nAChRs labeled with α-BTX conjugated with Alexa 555 (top row). Nerve terminal of the corresponding motor endplate (A-C) stained with FM1-43 dye (middle row), image taken after 30 minutes of incubation without nerve stimulation. Merged image of NMJ from α-BTX and FM1-43 images (bottom row). **D**) Mean fluorescence increase in nerve terminal of Nampt$^{f/f}$ (29.6±2.4, n=34), Nampt$^{-/-}$ cKO (30.0±2.9, n=27), and NMN-treated Nampt$^{-/-}$ cKO (29.9±2.9, n=36) mice. n is the number of nerve terminals from 3-4 mice.

2.4.4 Deletion of NAMPT in projection neurons leads to alterations in post-synaptic NMJ structure

Knockout of NAMPT in projection neurons not only impacts the neurons, but also produces changes in the skeletal muscles, most noticeably the significant amount of muscle atrophy [64]. Here, we investigated how the structure of the post-synaptic portion of the NMJ may be changed after the deletion of NAMPT. To do this, we isolated the semitendinosus muscle and incubated with α-BTX. The muscle was then covered with OCT and flash froze in liquid nitrogen. The muscle was then cross-sectioned for imaging. The α-BTX staining was used to locate the NMJs with acceptable orientation. Using Metamorph software, the α-BTX stained region was mapped using an exclusive threshold function (Fig. 2.5A-C). This region was then assessed to determine motor endplate measurements, as indicated in Fig. 2.5D. $Nampt^{-/-}$ cKO mice had a significantly reduced mean cross-sectional area compared to those in $Nampt^{f/f}$ mice (Fig. 2.5E). $Nampt^{-/-}$ cKO mice also had significantly lower mean length, breadth, and outer radius compared to $Nampt^{f/f}$ mice (Fig. 2.5F-G, I). The mean inner radius and the width of the endplate depression of NMJ was not significantly different between $Nampt^{-/-}$ cKO and $Nampt^{f/f}$ mice (Fig. 2.5H, J), but the depth of the depression was significantly reduced (Fig. 2.5K). The thickness of the endplate was also reduced in the $Nampt^{-/-}$ cKO mice. The left arm thickness, right arm thickness, and bottom thickness were all significantly smaller than $Nampt^{f/f}$ mice (Fig. 2.5L-N).

When the knockout mice were treated with NMN, there were significant improvements to the NMJ structure. The mean cross-sectional area of the NMN-treated $Nampt^{-/-}$ cKO mice was significantly larger than $Nampt^{-/-}$ cKO mice but was still less than $Nampt^{f/f}$ mice (Fig. 2.5E). Mean length, mean breadth, and mean outer radius were

significantly longer in the NMN-treated Nampt$^{-/-}$ cKO mice compared to Nampt$^{-/-}$ cKO mice but still significantly reduced compared to Nampt$^{f/f}$ mice (Fig. 2.5F-G,I). The mean inner radius for NMN-treated Nampt$^{-/-}$ cKO mice was significantly larger than both Nampt$^{-/-}$ cKO and Nampt$^{f/f}$ mice (Fig. 2.5H). NMN treatment lead to a significantly more narrow depression compared to both Nampt$^{-/-}$ cKO and Nampt$^{f/f}$ mice (Fig. 2.5J). The NMN treatment also produced a deeper depression than Nampt$^{-/-}$ cKO mice but not as deep as the Nampt$^{f/f}$ mice (Fig. 2.5K). Thickness of the left arm, right arm, and bottom of the motor endplate for the NMN-treated cKO mice was significantly larger than Nampt$^{-/-}$ cKO mice and not different from Nampt$^{f/f}$ mice (Fig. 2.5L-M).

The mean fluorescent intensity of the α-BTX staining, reflecting nicotinic acetylcholine receptor (nAChR) density, of the endplate was only significantly different between the Nampt$^{f/f}$ and NMN-treated Nampt$^{-/-}$ cKO mice (Fig. 2.5O). Overall, these data suggest that loss of NAMPT produces post-synaptic structural alterations of the NMJs. These endplates tend to be smaller, flatter and less thick compared to the endplates of Nampt$^{f/f}$ mice, but treatment of the Nampt$^{-/-}$ cKO mice with NMN prevented most alterations observed. The density of the postsynaptic nicotinic acetylcholine receptors may not be altered from loss of NAMPT.

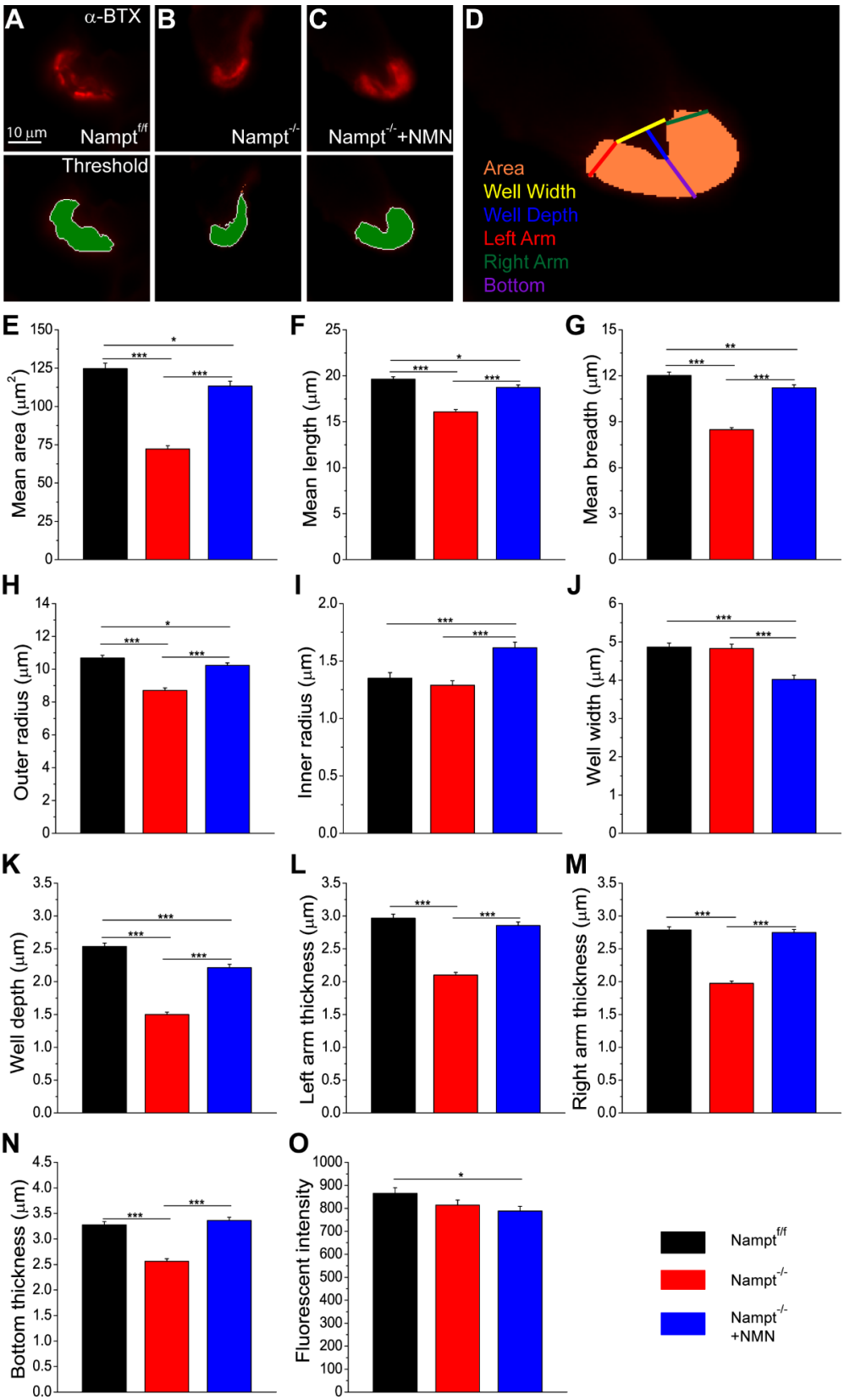
A
α-BTX
10 μm
Nampt^f/f
Threshold
B
Nampt^-/-
C
Nampt^-/-+NMN
D
Area
Well Width
Well Depth
Left Arm
Right Arm
Bottom
E
Mean area (μm²)
F
Mean length (μm)
G
Mean breadth (μm)
H
Outer radius (μm)
I
Inner radius (μm)
J
Well width (μm)
K
Well depth (μm)
L
Left arm thickness (μm)
M
Right arm thickness (μm)
N
Bottom thickness (μm)
O
Fluorescent intensity
Nampt^f/f
Nampt^-/-
Nampt^-/- +NMN

Figure 2.5. Motor endplate morphology is altered in Nampt$^{-/-}$ cKO mice. A-C) Cross-section of motor endplate from (A) Nampt$^{f/f}$ (n=342), (B) Nampt$^{-/-}$ cKO (n=268) and (C) NMN-treated Nampt$^{-/-}$ cKO (n=290) mice. nAChRs were labeled with α-BTX conjugated with Alexa 555 (top row). Area in green was the region analyzed after an exclusive fluorescence thresholding function was applied to the α-BTX labeled image (bottom row). **D)** Diagram of dimensions manually assessed (well depth, well width, and left, right, and bottom thickness) using the thresholded endplate region. Area was calculated by analysis software. Motor endplate measurements always go Nampt$^{f/f}$, Nampt$^{-/-}$ cKO, and NMN-treated Nampt$^{-/-}$ cKO mice. **E**) Mean area of motor endplate cross-section; (124.7±3.5), (72.3±2.1), and (113.32±3.13). **F**) Mean length of motor endplate; (19.62±0.28), (16.07±0.26), and (18.73±0.27). **G**) Mean breadth of motor endplate; (12.03±0.20), (8.50±0.14), and (11.21±0.20). **H**) Mean inner radius of motor endplate; (1.35±0.05), (1.29±0.04), and (1.62±0.05). **I**) Mean outer radius of motor endplate; (10.69±0.16), (8.71±0.15), and (10.23±0.16). **J**) Mean width of motor endplate depression; (4.86±0.10), (4.83±0.12), and (4.02±0.11). **K**) Mean depth of motor endplate depression; (2.54±0.05), (1.50±0.04), and (2.21±0.05). **L**) Mean thickness of left arm of motor endplate; (2.97±0.06), (2.10±0.04), and (2.86±0.05). **M**) Mean thickness of right arm of motor endplate; (2.79±0.05), (1.97±0.04), and (2.75±0.05). **N**) Mean thickness of bottom of motor endplate; (3.27±0.06), (2.56±0.05), and (3.36±0.06**). O**) Mean fluorescence of α-BTX staining; (865.21±24), (813.80±22), and (788.16±21). n is the number of motor endplates from 9-12 mice; *p<0.05, **p<0.01, ***p<0.001, Student's t-test.

2.4.5 Skeletal muscle contractile response is affected following NAMPT deletion from projection neurons

Our previous experiments indicated that synaptic transmission has been impaired following NAMPT knockout. Disabled synaptic transmission from the motor terminal at the NMJ has been suggested to affect muscle function [69, 70]. To determine whether knockout of NAMPT produces any changes to muscle contraction, semitendinosus muscles were isolated in the same manner as for the previous experiments. In a sylgard coated dish, the wide end of the muscle was pinned down and the other end was connected to a force transducer by a piece of string. The muscle was stimulated at different frequencies and the responses were recorded.

The contractile responses can be separated into three stimulation groups: low frequency (1Hz and 5 Hz), moderate frequency (10, 20, and 50 Hz), and high frequency (100 Hz). For low frequency group, the contractile response patterns were very similar between 1 Hz and 5 Hz. At 1 and 5 Hz stimulation (Fig. 2.6A & C), peak contractile force was not significantly different between the three groups (Fig. 2.6B1 & D1). Also, the time to peak force was not significantly different between the three groups (Fig. 2.6B2 & D2). For both frequencies, $Nampt^{f/f}$ mice had a prolonged return to baseline time relative to $Nampt^{-/-}$ cKO and NMN-treated $Nampt^{-/-}$ cKO mice (Fig. 2.6B3 & D3). The return to baseline time for $Nampt^{-/-}$ cKO and NMN-treated $Nampt^{-/-}$ cKO mice was only different at 1 Hz (Fig. 2.6B3). Overall, these results indicate that after knockout of NAMPT, skeletal muscles have shorter relaxation times following low frequency stimulation.

The response pattern for moderate stimulation frequencies was very different from the low frequencies (Fig. 2.6E, G, I). The peak contractile force for $Nampt^{-/-}$ cKO mice was significantly larger than for NMN-treated $Nampt^{-/-}$ cKO mice at 10, 20, and 50 Hz (Fig.

2.6F1, H1, I1). Nampt$^{f/f}$ and Nampt$^{-/-}$ cKO mice were not different at 10 Hz but Nampt$^{f/f}$ mice produced significantly weaker contractions at 20 and 50 Hz (Fig. 2.6H1 & I1). Nampt$^{f/f}$ and NMN-treated Nampt$^{-/-}$ cKO mice had a significant difference in peak contractile force at 10 Hz and 20 Hz but not 50 Hz (Fig. 2.6F1, H1, I1). Nampt$^{f/f}$ mice had a longer time to reach peak force at 10 Hz (Fig. 2.6F2). Nampt$^{-/-}$ cKO mice displayed increased time to peak force at 20 and 50 Hz (Fig. 2.6H2 & I2). Nampt$^{f/f}$ mice had a longer return to baseline time at 10 Hz and 50 Hz but Nampt$^{-/-}$ cKO mice had a longer return time at 20 Hz (Fig. 2.6F3, H3, I3). There was no difference in the slope between the three groups at 10 Hz (Fig. 2.6F4). For 20 and 50 Hz, NMN-treated Nampt$^{-/-}$ cKO mice had significantly smaller slopes Nampt$^{f/f}$ and Nampt$^{-/-}$ cKO mice (Fig. 2.6H4 & I4). For moderate frequencies, these data indicate that loss of NAMPT in the projection neuron may induce significant changes in the muscle, with the muscles attempting to compensate for the loss with increased contractile force. Interestingly, NMN treatment produced a unique phenotype separate from Nampt$^{f/f}$ and Nampt$^{-/-}$ cKO mice, where the muscles had reduced contractile force but lost force more slowly.

Stimulation at a high frequency (100 Hz) formed a third group of responses (Fig. 2.6K). The Nampt$^{-/-}$ cKO mice were completely unresponsive to this stimulation. No significant difference was found in peak contractile force or time to reach peak force between the Nampt$^{f/f}$ and NMN-treated Nampt$^{-/-}$ cKO mice (Fig. 2.6L1-2). NMN-treated Nampt$^{-/-}$ cKO did have a significantly shorter return to baseline time than Nampt$^{f/f}$ mice (Fig. 2.6L3). There was no significant difference in slope between the two groups (Fig. 2.6L4). It may be more useful to compare the recordings themselves (Fig. 2.6K) because, whereas the Nampt$^{f/f}$ traces were smooth with little vacillation of the trace, the NMN-

treated Nampt$^{-/-}$ cKO mice recordings seem to indicate a muscle struggling to maintain a contraction. The difference found in the return to baseline time would support this.

Overall, these results indicate changes within the skeletal muscles of Nampt$^{-/-}$ cKO mice. At low frequencies, contractions are similarly fast and strong as Nampt$^{f/f}$, but with relaxation occurring more quickly in both of the Nampt$^{-/-}$ cKO groups. Surprisingly, as stimulation frequency was increased into moderate ranges, the contraction force was significantly increased for Nampt$^{-/-}$ cKO mice but reduced for the NMN-treated Nampt$^{-/-}$ cKO mice. This may point toward some compensatory action in the muscle as a response to the knockout of NAMPT from the projection neurons, an action that does not occur if NMN is provided. The NMN administration seemed to produce an intermediate response state, where the muscle is not unhealthy enough for compensation to occur but also not healthy enough to respond as the Nampt$^{f/f}$ mice do. Treatment with NMN does allow the nerve to remain responsive to 100 Hz stimulation, though the response of the muscle suggests some impairment.

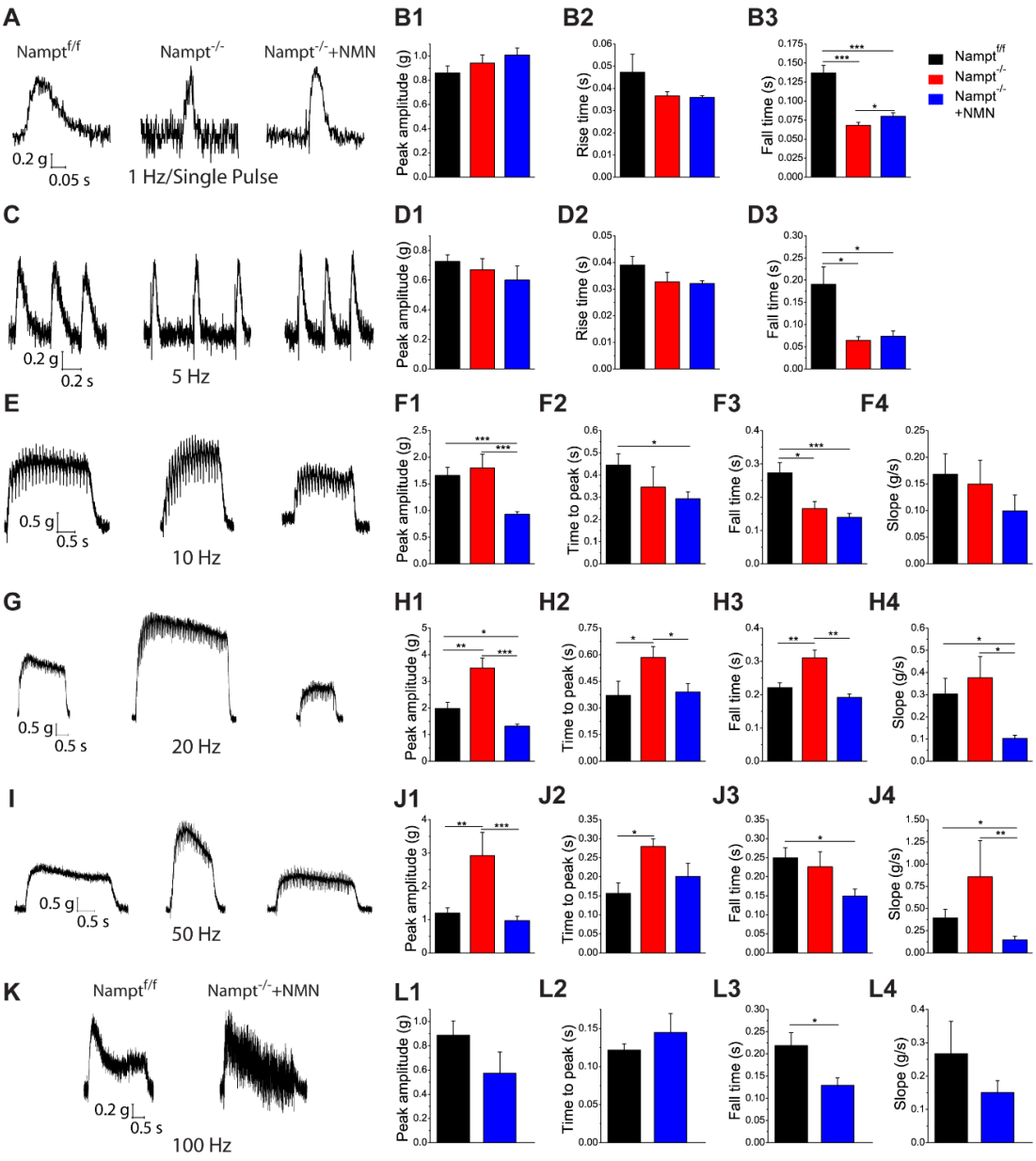

Figure 2.6. Nampt$^{-/-}$ cKO mice exhibit quicker muscle relaxation and enhanced contractile force but reduced range of responsiveness. A) Representative trace for 1 Hz/Single Pulse stimulation for Nampt$^{f/f}$ (N=5; n=57), Nampt$^{-/-}$ cKO (N=4; n=53), and NMN-treated Nampt$^{-/-}$ cKO (N=5; n=49) mice. **B**) Mean contractile force (B1), Mean rise time to peak contraction force (B2), and Mean time return to baseline (B3) for 1 Hz/Single pulse stimulation. **C**) Representative traces for 5 Hz stimulation for Nampt$^{f/f}$ (N=3; n=19), Nampt$^{-/-}$ cKO (N=3; n=10), and NMN-treated Nampt$^{-/-}$ cKO (N=2; n=10) mice. **D**) Mean contractile force (D1), Mean rise time to peak contraction force (D2), and Mean time return to baseline (D3) for 5 Hz

stimulation. **E**) Representative trace for 10 Hz stimulation for Nampt$^{f/f}$ (N=4; n=20), Nampt$^{-/-}$ cKO (N=4; n=13), and NMN-treated Nampt$^{-/-}$ cKO (N=5; n=22) mice. **F**) Mean maximum contractile force (F1), Mean time to maximum contraction force (F2), Mean time to return to baseline after stimulation was ended (F3), and Mean slope (in grams force lost per second; calculated from time when maximum contractile force is reached to time when stimulation was removed) (F4) for 10 Hz stimulation. **G**) Representative trace for 20 Hz stimulation for Nampt$^{f/f}$ (N=3; n=9), Nampt$^{-/-}$ cKO (N=3; n=10), and NMN-treated Nampt$^{-/-}$ cKO (N=2; n=6) mice. **H**) Mean maximum contractile force (H1), Mean time to maximum contraction force (H2), Mean time to return to baseline after stimulation was ended (H3), and Mean slope (H4) for 20 Hz stimulation. **I**) Representative trace for 50 Hz stimulation for Nampt$^{f/f}$ (N=4; n=18), Nampt$^{-/-}$ cKO (N=3; n=5), and NMN-treated Nampt$^{-/-}$ cKO (N=5; n=14) mice. **J**) Mean maximum contractile force (J1), Mean time to maximum contraction force (J2), Mean time to return to baseline after stimulation was ended (J3), and Mean slope (J4) for 50 Hz stimulation. **K**) Representative trace for 100 Hz stimulation for Nampt$^{f/f}$ (N=3; n=8) and NMN-treated Nampt$^{-/-}$ cKO (N=3; n=6) mice. **L**) Mean maximum contractile force (L1), Mean time to maximum contraction force (L2), Mean time to return to baseline after stimulation was ended (L3), and Mean slope (L4) for 100 Hz stimulation. N is the number of mice and n is the number of responses; *$p<0.05$; **$p<0.01$; ***$p<0.001$, Student's t-test.

2.4.6 Skeletal muscle sarcomere alignment and mitochondria morphology following NAMPT deletion from projection neurons

Based on the results from the skeletal muscle contractile response, we decided to investigate whether knockout of NAMPT may also produce changes to skeletal muscle structure and mitochondria morphology in conjunction to the functional changes we found. The mitochondria in skeletal muscles can be divided into two groups, the sub-sarcolemmal (SS) and the intermyofibrillar (IMF). The SS and IMF mitochondria differ in location, morphology, and physiological properties [68, 71, 72]. IMF mitochondria are also thought to be more important for muscle contraction [71, 73]. This led us to investigate how IMF mitochondrial morphology may be affected following NAMPT knockout. To do this, we performed TEM on semitendinosus muscles dissected from $Nampt^{-/-}$ cKO and NMN-treated $Nampt^{-/-}$ cKO 23 days after the final TAM injection, as well as aged matched $Nampt^{f/f}$ mice to assess myofiber composition and mitochondrial morphology. Fig. 2.7A diagrams the analysis of different structures of a longitudinal section.

For longitudinal sections, knockout of NAMPT altered myofibers. Skeletal muscle myofibers are made up of many smaller functional units called sarcomeres. Skeletal muscles from $Nampt^{f/f}$ mice had myofibers with well aligned sarcomeres, with Z discs typically in line with the Z discs of adjacent sarcomeres (Fig. 2.7B, top panels). $Nampt^{-/-}$ cKO mice displayed noticeable sarcomere misalignment, with some areas being well aligned but other areas having no alignment (Fig. 2.7B, middle panels, asterisks). NMN-treated $Nampt^{-/-}$ cKO mice had sarcomere alignment similar to the $Nampt^{f/f}$ mice (Fig. 2.7B, bottom panels). There did not seem to be any noticeable changes to the triadic junctions, a group composed of a transverse tubule flanked by sarcoplasmic reticulum, in

the Nampt$^{-/-}$ cKO or NMN-treated Nampt$^{-/-}$ cKO mice (Fig. 2.7C, arrows). Thus, deletion of Nampt causes considerable misalignment of sarcomeres which NMN treatment is able to restore.

Longitudinal (Fig. 2.7C) and transverse (Fig. 2.7D) mitochondrial morphology was altered for both Nampt$^{-/-}$ cKO and NMN-treated Nampt$^{-/-}$ cKO mice. Longitudinal mitochondrial area was significantly larger for NMN-treated Nampt$^{-/-}$ cKO mice (Fig. 2.7E). The perimeter was also significantly longer for NMN-treated Nampt$^{-/-}$ cKO mice (Fig. 2.7F). Namp$^{-/-}$ cKO and Nampt$^{f/f}$ mice did not differ for area or perimeter. Circularity was significantly lower for both Nampt$^{-/-}$ cKO and NMN-treated Nampt$^{-/-}$ cKO mice (Fig. 2.7G). Feret's diameter was significantly longer in Nampt$^{-/-}$ cKO and NMN-treated Nampt$^{-/-}$ cKO mice (Fig. 2.7H). Transverse mitochondrial area was reduced in the Nampt$^{-/-}$ cKO mice (Fig. 2.7I). Though, no difference was observed in perimeter length between the three conditions (Fig. 2.7J). Circularity was significantly higher in the NMN-treated Nampt$^{-/-}$ cKO mice and significantly lower in the untreated Nampt$^{-/-}$ cKO mice (Fig. 2.7K). No difference was observed in Feret's diameter (Fig. 2.7L). Overall, these results suggest that deletion of NAMPT alters skeletal muscle mitochondria morphology, with NMN unable to restore normal shape.

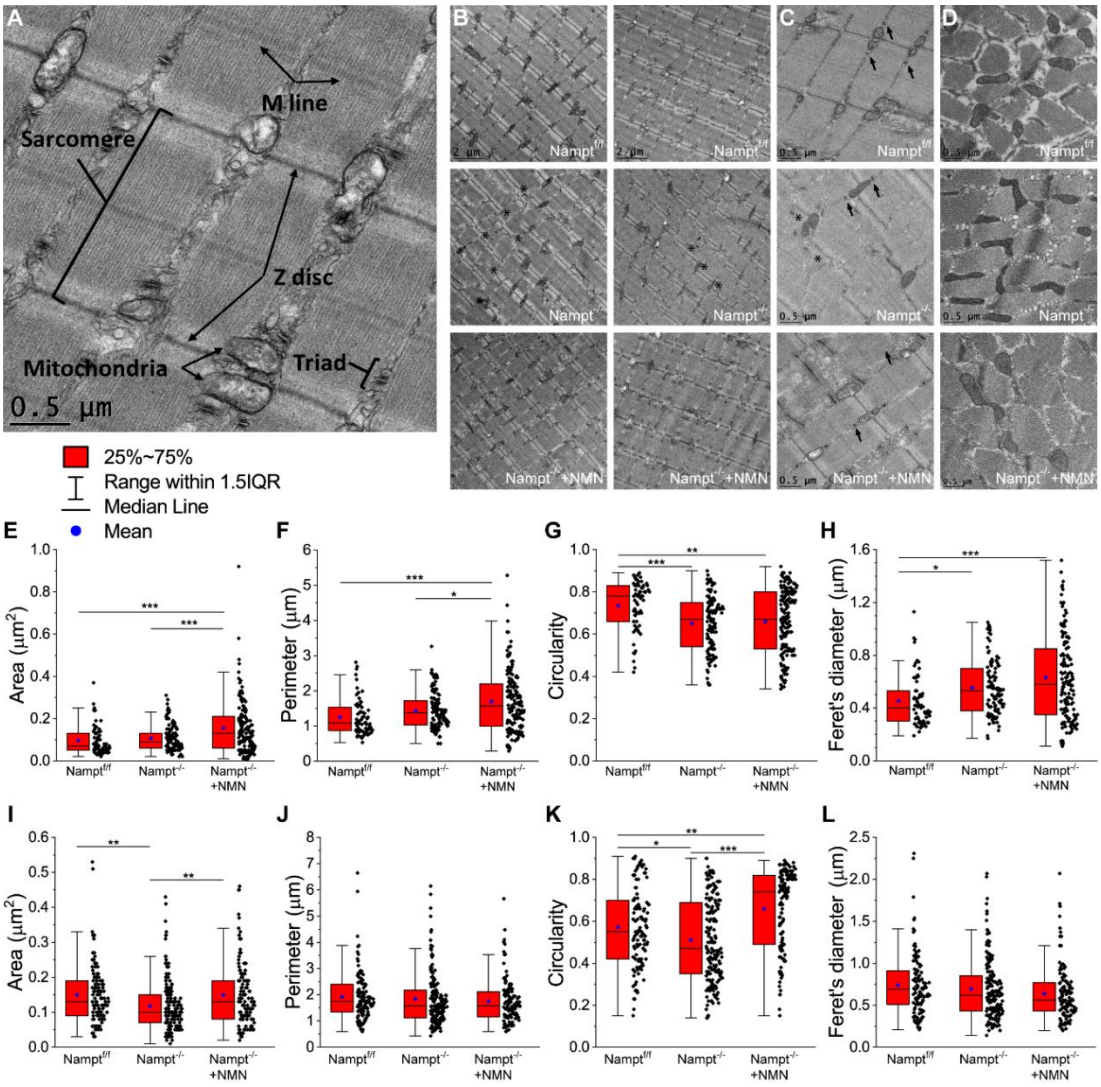

Figure 2.7. Altered sarcomere alignment and mitochondrial morphology in longitudinal and transverse plane of Nampt$^{-/-}$ cKO mice revealed by TEM. A) Diagram of skeletal muscle components analyzed from TEM images. **B-C**) Representative longitudinal TEM images of Nampt$^{f/f}$, Nampt$^{-/-}$ cKO, and NMN-treated Nampt$^{-/-}$ cKO mice. Arrows in indicate triadic junctions and asterisks indicate misaligned Z discs. **D**) Representative transverse TEM images of Nampt$^{f/f}$, Nampt$^{-/-}$ cKO, and NMN-treated Nampt$^{-/-}$ cKO mice. **E**) Distribution of mitochondrial area in longitudinal plane from Nampt$^{f/f}$ (n=65), Nampt$^{-/-}$ cKO (n=109), and NMN-treated Nampt$^{-/-}$ cKO (n=140) mice. **F**) Distribution of mitochondrial perimeter in longitudinal plane from Nampt$^{f/f}$, Nampt$^{-/-}$ cKO, and NMN-treated Nampt$^{-/-}$ cKO mice. **G**) Distribution of mitochondrial circularity in longitudinal plane from Nampt$^{f/f}$, Nampt$^{-/-}$ cKO, and NMN-treated Nampt$^{-/-}$ cKO

mice. **H**) Distribution of mitochondrial perimeter in longitudinal plane from Nampt$^{f/f}$, Nampt$^{-/-}$ cKO, and NMN-treated Nampt$^{-/-}$ cKO mice. **I**) Distribution of mitochondrial area in transverse plane from Nampt$^{f/f}$ (n=115), Nampt$^{-/-}$ cKO (n=170), and NMN-treated Nampt$^{-/-}$ cKO (n=118) mice. **J**) Distribution of mitochondrial perimeter in transverse plane from Nampt$^{f/f}$, Nampt$^{-/-}$ cKO, and NMN-treated Nampt$^{-/-}$ cKO mice. **K**) Distribution of mitochondrial circularity in transverse plane from Nampt$^{f/f}$, Nampt$^{-/-}$ cKO, and NMN-treated Nampt$^{-/-}$ cKO mice. **L**) Distribution of mitochondrial perimeter in transverse plane from Nampt$^{f/f}$, Nampt$^{-/-}$ cKO, and NMN-treated Nampt$^{-/-}$ cKO mice. n is the number of mitochondria from 1-2 mice; *p<0.05, **p<0.01, ***p<0.001, Student's t-test.

2.5 Discussion

The results from our experiments demonstrate how the conditional knockout of NAMPT in projection neurons produces detriments to both the presynaptic and postsynaptic aspects of the NMJ. Neurons lacking NAMPT displayed impaired endocytosis and exocytosis based on live muscle imaging of FM1-43 dye. Both the rate of dye uptake/release and total amount of dye loaded/unloaded were reduced in the Nampt$^{-/-}$ cKO mice. Our data also suggests that Nampt$^{-/-}$ cKO mice are unable to mobilize all labeled synaptic vesicles. The detriments observed in Nampt$^{-/-}$ cKO mice were alleviated when the NAD^+ precursor, NMN, was administrated in the mice. Control mice administered NMN daily showed had similar levels of FM1-43 dye uptake and release.

Our western blot data did not indicate a significant change in iNAMPT or eNAMPT levels which is consistent with data from our previous study [64]. We did not find any increase in NAD^+ in skeletal muscle following NMN injection. This finding is consistent with previous research that found administration of a different NAD salvage pathway precursor, nicotinamide riboside, also did not increase skeletal muscle NAD^+ [52].

The differences in total fluorescence could be explained by a reduction in the number of synaptic vesicles in the NAMPT knockout mice. A reduction in the amount synaptic vesicles has been observed in the NMJs of different gene knockout and disease mouse models that have exhibited synaptic transmission problems [74-76]. Previous experiments in Thy1-NAMPT$^{-/-}$ cKO mice has also supported the possibility of a smaller pool of vesicles [64]. However, a reduction in the number of synaptic vesicles available would not fully explain our results. Fewer synaptic vesicles should result in faster saturation/depletion of the fluorescence intensity, but that is not what we found. Instead,

we found that Nampt$^{-/-}$ cKO mice were slower at loading and unloading the dye. This suggests problems within the synaptic vesicle cycle of projection neurons though more investigation is needed to determine whether the synaptic vesicle pool size has changed following deletion or NAMPT.

The vesicles used in synaptic signaling can be separated into two different pools: the readily-releasable pool (RRP) and the reserve pool (RP) [77]. Stimulation at 10 Hz is believed to load FM1-43 into vesicles of both pools [78], so our experiments should be labeling vesicles in the RRP and RP. Identifying where the problem is occurring may be challenging because there are many proteins involved in synaptic vesicle recycling [79]. Alterations to Ca^{2+} levels could also be occurring, given the critical role Ca^{2+} has in endocytosis and exocytosis [80, 81].

The results from our initial destain data led us to investigate whether Nampt$^{-/-}$ cKO mice experienced problems in mobilizing vesicles loaded with FM1-43 dye or had the rate of exocytosis only been reduced. If only the rate of exocytosis had been affected, then increasing the duration of destain stimulation would provide more time for the FM1-43 labeled vesicles to be released and for fluorescence to steadily decline. On the other hand, if certain labeled vesicles cannot be released, then the fluorescence decrease would plateau and the intensity level remain relatively stable. We observed the latter, indicating that Nampt$^{-/-}$ cKO mice may not be able to access certain synaptic vesicles, possibly a result of RP vesicles not being moved to the RRP. The specific mechanisms that mobilize a synaptic vesicle from the RP to the RRP are not well understood [77]. Curiously, our results are similar to the differences observed in 10 Hz vs. 100 Hz exocytosis [78], suggesting that knockout of NAMPT may inappropriately activate rapid recycling of vesicles at lower

frequencies. More investigation is needed to determine the cause of synaptic cycle dysfunction.

The spontaneous endocytosis of FM1-43 was not affected from the knockout of NAMPT. Given that our results indicate only evoked activity has been altered and the importance NAMPT activity has on cell metabolism, knockout of NAMPT from projection neurons may disrupt neuronal energetics and a consequence of this may be disruption of the synaptic vesicle cycle. However, more research is needed to determine if this assumption is correct. The exact role NAMPT may have in the synaptic vesicle cycle is unclear but recently NMNAT, the enzyme performing the reaction immediately after NAMPT, was shown to impact synaptic transmission [82], giving some evidence that the enzymes of the NAD salvage pathway may directly influence the synaptic vesicle cycle .

A significant alteration in the morphology of the motor endplate was also observed in Nampt$^{-/-}$ cKO mice. Loss of NAMPT produced a smaller, flatter, and thinner motor endplate but receptor density did not seem to be affected. The clustering and recycling of the nAChRs, which an important aspect of normal NMJ maintenance, has been a focus of a large amount of research [83]. Our results do not suggest any problems with the localization of nAChRs, indicating that the signaling pathway and microtubules involved in clustering and inserting nAChRs may not have been affected [84]. Future investigations should investigate proteins involved in maintenance of NMJ structure as well as proteins involved in nAChR expression and formation.

Our results from the muscle contraction experiment were unexpected. At low frequencies of stimulation (1 Hz or 5 Hz), we observed no change in peak force and rise time after NAMPT deletion. The return to baseline, indicating muscle relaxation, was

significantly faster in both Nampt$^{-/-}$ cKO conditions. This may indicate that the speed or amount of Ca^{2+} released has not been affected but that Ca^{2+} may be removed from the cytosol faster. A possible explanation for our results could be upregulation of SERCA expression in the Nampt$^{-/-}$ cKO mice. The sarcoplasmic reticulum (SR) is the main storage site of Ca^{2+} in muscle and the sarco-(endo) plasmic reticulum Ca^{2+}-ATPase (SERCA) is responsible for clearing the Ca^{2+} from the cytosol. More investigation is needed to determine the cause for the faster muscle relaxation.

The impact of the deletion of NAMPT became more evident as the stimulation frequency was increased. Loss of NAMPT appears to induce a compensatory response in the skeletal muscle, where Nampt$^{-/-}$ cKO mice exhibit enhanced contractile force across moderate stimulation frequencies. We also found that providing NMN to the Nampt$^{-/-}$ cKO mice did not restore the normal contractile response, but instead produced a unique phenotype. This was surprising given the results indicating how NMN administration can return synaptic function and motor endplate morphology to relatively normal levels. It is possible that the supplementation produced partial recovery. NMN may have prevented the downstream effects that resulted in the increased contractile force observed in the Nampt$^{-/-}$ cKO mice but was insufficient for maintaining normal muscle contraction. Instead, the NMN-treated mice to had responses that resembled the Nampt$^{f/f}$ mice in shape but with reduced force.

Excitation-contraction coupling has been well defined in skeletal muscles and there are many possibilities where changes could have occurred. Altered Ca^{2+} clearance could also be responsible, with the enhanced contractile force the result of elevated Ca^{2+} release in Nampt$^{-/-}$ cKO mice for moderate stimulation frequencies. Investigation of Ca^{2+}

movement and the excitation-contraction pathway is needed. The lack of response to 100 Hz stimulation in Nampt$^{-/-}$ cKO mice is consistent with previous research showing motor nerves lacking NAMPT exhibited impaired synaptic transmission at high stimulation frequencies [64]. Direct stimulation of the muscle would be needed to determine the contractile response of muscles form Nampt$^{-/-}$ cKO mice. NMN treatment allowed the motor nerves to respond to 100 Hz stimulation but the muscle contractions still indicated some impairment compared to Nampt$^{f/f}$ mice.

We also observed changes to myofiber arrangement and mitochondrial morphology. Sarcomere misalignment was common in Nampt$^{-/-}$ cKO mice. NMN treatment seemed to prevent this misalignment. Sarcomere misalignment has been observed in animal models for muscular dystrophy, ataxia telangiectasia, and amyotrophic lateral sclerosis (ALS), as well as in denervated muscles and indicates changes in normal myofiber interactions [85-88]. We also observed no differences in the triadic junction. Alterations to triadic junctions has been observed in skeletal muscle-specific NAMPT knockout mice, as well as in denervated rat skeletal muscles [52, 87]. Nampt$^{-/-}$ cKO mice undergo significant denervation [64] so the lack of triad alterations is slightly unexpected. However, this could be due to the life expectancy of our mice following NAMPT knockout. Following NAMPT deletion mice typically will not survive beyond 4 weeks, while the triad alterations observed in the skeletal muscle NAMPT knockout mice were observed at 7 months of age and from rats that had been devervated for 56 days [52, 87]. In could simply be that Nampt$^{-/-}$ cKO mice do not survive long enough for these alterations to occur.

IMF mitochondrial morphology is significantly different following the loss of NAMPT. The mitochondria from Nampt$^{-/-}$ cKO mice were similar, if not slightly smaller,

in size relative to Nampt$^{f/f}$ mice but were abnormally shaped. The mitochondria from NMN-treated Nampt$^{-/-}$ cKO mice were also abnormally shaped but also seemed to larger, especially compared the untreated Nampt$^{-/-}$ cKO mice. No swelling or cristae disruptions were observed in any condition, which are common for mitochondrial dysfunction [89]. It is widely thought that mitochondrial dysfunction and abnormal mitochondrial morphology are connected. This is supported by from experimentation in aged and disease models of mice [52, 68, 88-90]. We did not perform any functional experimentation on skeletal muscle mitochondria but Nampt$^{-/-}$ cKO and NMN-treated Nampt$^{-/-}$ cKO mice both demonstrated abnormal mitochondria morphology relative to Nampt$^{f/f}$ mice, so possible functional changes would not be unexpected. More investigation is needed to determine how mitochondrial function may have been altered.

In summary, the current study found that deletion of NAMPT from projection neurons causes detrimental effects in NMJ function and structure. Skeletal muscles are also impacted from this deletion. NMN can largely prevent the NMJ changes but is less effective in preventing alterations to the skeletal muscle. Further experiments are needed to identify whether these results are the product of very specific alterations or caused by changes to normal neuronal function. As the symptoms (*e.g.*, muscle atrophy, paralysis and NMJ dysfunction) of the Nampt$^{-/-}$ cKO mice resemble to those in ALS model and NAMPT is downregulated in human ALS brain [64], the current study also provides further implication for the involvement of the NAMPT-mediated NAD^+ salvage pathway in the pathology of ALS.

2.6 Reference

1. Fuke, S., et al., *Hesr1 knockout mice exhibit behavioral alterations through the dopaminergic nervous system.* J Neurosci Res, 2006. **84**(7): p. 1555-63.
2. Revollo, J.R., et al., *Nampt/PBEF/Visfatin regulates insulin secretion in beta cells as a systemic NAD biosynthetic enzyme.* Cell Metab, 2007. **6**(5): p. 363-75.
3. Luk, T., Z. Malam, and J.C. Marshall, *Pre-B cell colony-enhancing factor (PBEF)/visfatin: a novel mediator of innate immunity.* J Leukoc Biol, 2008. **83**(4): p. 804-16.
4. Imai, S., *The NAD World: a new systemic regulatory network for metabolism and aging--Sirt1, systemic NAD biosynthesis, and their importance.* Cell Biochem Biophys, 2009. **53**(2): p. 65-74.
5. Magni, G., et al., *Enzymology of NAD+ homeostasis in man.* Cell Mol Life Sci, 2004. **61**(1): p. 19-34.
6. Alano, C.C., et al., *NAD+ depletion is necessary and sufficient for poly(ADP-ribose) polymerase-1-mediated neuronal death.* J Neurosci, 2010. **30**(8): p. 2967-78.
7. Yang, H., S. Lavu, and D.A. Sinclair, *Nampt/PBEF/Visfatin: a regulator of mammalian health and longevity?* Exp Gerontol, 2006. **41**(8): p. 718-26.
8. Raval, A.P., K.R. Dave, and M.A. Perez-Pinzon, *Resveratrol mimics ischemic preconditioning in the brain.* J Cereb Blood Flow Metab, 2006. **26**(9): p. 1141-7.
9. Csiszar, A., et al., *Resveratrol induces mitochondrial biogenesis in endothelial cells.* American Journal of Physiology - Heart and Circulatory Physiology, 2009. **297**(1): p. H13-H20.

10. Lagouge, M., et al., *Resveratrol improves mitochondrial function and protects against metabolic disease by activating SIRT1 and PGC-1alpha.* Cell, 2006. **127**(6): p. 1109-22.

11. Wang, S., et al., *Cellular NAD replenishment confers marked neuroprotection against ischemic cell death: role of enhanced DNA repair.* Stroke, 2008. **39**(9): p. 2587-95.

12. Pittelli, M., et al., *Pharmacological effects of exogenous NAD on mitochondrial bioenergetics, DNA repair, and apoptosis.* Mol Pharmacol, 2011. **80**(6): p. 1136-46.

13. Wang, X., H. Li, and S. Ding, *The effects of NAD+ on apoptotic neuronal death and mitochondrial biogenesis and function after glutamate excitotoxicity.* Int J Mol Sci, 2014. **15**(11): p. 20449-68.

14. Ding, D., et al., *Addition of Exogenous NAD+ Prevents Mefloquine-Induced Neuroaxonal and Hair Cell Degeneration through Reduction of Caspase-3-Mediated Apoptosis in Cochlear Organotypic Cultures.* PloS one, 2013: p. e79817.

15. Gomes, A.P., et al., *Declining NAD(+) induces a pseudohypoxic state disrupting nuclear-mitochondrial communication during aging.* Cell, 2013. **155**(7): p. 1624-38.

16. Yoshino, J., et al., *Nicotinamide mononucleotide, a key NAD(+) intermediate, treats the pathophysiology of diet- and age-induced diabetes in mice.* Cell Metab, 2011. **14**(4): p. 528-36.

17. Zheng, C., et al., *NAD(+) administration decreases ischemic brain damage partially by blocking autophagy in a mouse model of brain ischemia.* Neurosci Lett, 2012. **512**(2): p. 67-71.

18. van der Veer, E., et al., *Extension of human cell lifespan by nicotinamide phosphoribosyltransferase.* J Biol Chem, 2007. **282**(15): p. 10841-5.

19. Belenky, P., K.L. Bogan, and C. Brenner, *NAD+ metabolism in health and disease.* Trends Biochem Sci, 2007. **32**(1): p. 12-9.

20. Dvir-Ginzberg, M., et al., *Regulation of cartilage-specific gene expression in human chondrocytes by SirT1 and nicotinamide phosphoribosyltransferase.* J Biol Chem, 2008. **283**(52): p. 36300-10.

21. Revollo, J.R., A.A. Grimm, and S. Imai, *The NAD biosynthesis pathway mediated by nicotinamide phosphoribosyltransferase regulates Sir2 activity in mammalian cells.* J Biol Chem, 2004. **279**(49): p. 50754-63.

22. McGlothlin, J.R., et al., *Molecular Cloning and Characterization of Canine Pre-B-Cell Colony-Enhancing Factor.* Biochemical Genetics, 2005. **43**(3-4): p. 127-141.

23. Stein, L.R., et al., *Expression of Nampt in hippocampal and cortical excitatory neurons is critical for cognitive function.* J Neurosci, 2014. **34**(17): p. 5800-15.

24. Stein, L.R. and S. Imai, *Specific ablation of Nampt in adult neural stem cells recapitulates their functional defects during aging.* EMBO J, 2014. **33**(12): p. 1321-40.

25. Bi, J., et al., *Pre-B-cell colony-enhancing factor exerts a neuronal protection through its enzymatic activity and the reduction of mitochondrial dysfunction in in vitro ischemic models.* J Neurochem, 2012. **120**(2): p. 334-46.

26. Zhang, W., et al., *Neuronal protective role of PBEF in a mouse model of cerebral ischemia.* J Cereb Blood Flow Metab, 2010. **30**(12): p. 1962-71.

27. Lu, L.F., et al., *Elevated visfatin/pre-B-cell colony-enhancing factor plasma concentration in ischemic stroke.* J Stroke Cerebrovasc Dis, 2009. **18**(5): p. 354-9.

28. Wang, P., et al., *Nicotinamide phosphoribosyltransferase protects against ischemic stroke through SIRT1-dependent adenosine monophosphate-activated kinase pathway.* Ann Neurol, 2011. **69**(2): p. 360-74.

29. Erfani, S., et al., *Nampt/PBEF/visfatin exerts neuroprotective effects against ischemia/reperfusion injury via modulation of Bax/Bcl-2 ratio and prevention of caspase-3 activation.* J Mol Neurosci, 2015. **56**(1): p. 237-43.

30. Jing, Z., et al., *Neuronal NAMPT is released after cerebral ischemia and protects against white matter injury.* J Cereb Blood Flow Metab, 2014. **34**(10): p. 1613-21.

31. Wang, P., et al., *Intracellular NAMPT-NAD+-SIRT1 cascade improves post-ischaemic vascular repair by modulating Notch signalling in endothelial progenitors.* Cardiovasc Res, 2014. **104**(3): p. 477-88.

32. Zhao, Y., et al., *Regenerative Neurogenesis After Ischemic Stroke Promoted by Nicotinamide Phosphoribosyltransferase-Nicotinamide Adenine Dinucleotide Cascade.* Stroke, 2015. **46**(7): p. 1966-74.

33. Wang, P., et al., *Induction of autophagy contributes to the neuroprotection of nicotinamide phosphoribosyltransferase in cerebral ischemia.* Autophagy, 2012. **8**(1): p. 77-87.

34. Li, Y., et al., *Extracellular Nampt promotes macrophage survival via a nonenzymatic interleukin-6/STAT3 signaling mechanism.* J Biol Chem, 2008. **283**(50): p. 34833-43.

35. Ami P. Raval, et al., *Resveratrol and Ischemic Preconditioning in the Brain.* Current Medicinal Chemistry, 2008. **15**: p. 1545-1551.

36. Kim, J.S., C.S. Yoon, and D.R. Park, *NAMPT regulates mitochondria biogenesis via NAD metabolism and calcium binding proteins during skeletal muscle contraction.* J Exerc Nutrition Biochem, 2014. **18**(3): p. 259-66.

37. Sun, Z., H. Lei, and Z. Zhang, *Pre-B cell colony enhancing factor (PBEF), a cytokine with multiple physiological functions.* Cytokine Growth Factor Rev, 2013. **24**(5): p. 433-442.

38. Li, H., et al., *Augmentation of Pulmonary Epithelial Cell IL-8 Expression and Permeability by Pre-B-cell Colony Enhancing Factor.* J Inflamm (Lond), 2008. **5**: p. 1.

39. Moschen, A., et al., *Visfatin, an Adipocytokine with Proinflammatory and Immunomodulating Properties.* J Immunol, 2007. **178**: p. 1748-1758.

40. Fukuhara, A., et al., *Visfatin: a protein secreted by visceral fat that mimics the effects of insulin.* Science, 2005. **307**(5708): p. 426-430.

41. Laudes, M., et al., *Visfatin/PBEF/Nampt and resistin expressions in circulating blood monocytes are differentially related to obesity and type 2 diabetes in humans.* Horm Metab Res, 2010. **42**(4): p. 268-73.

42. Stastny, J., J. Bienertova-Vasku, and A. Vasku, *Visfatin and its role in obesity development.* Diabetes Metab Syndr, 2012. **6**(2): p. 120-4.

43. Dirnagl, U., C. Iadecola, and M.A. Moskowitz, *Pathobiology of ischaemic stroke: an integrated view.* Trends Neurosci., 1999. **22**: p. 391-397.

44. Verdin, E., *NAD(+) in aging, metabolism, and neurodegeneration.* Science, 2015. **350**(6265): p. 1208-13.

45. Rajman, L., K. Chwalek, and D.A. Sinclair, *Therapeutic Potential of NAD-Boosting Molecules: The In Vivo Evidence.* Cell Metab, 2018. **27**(3): p. 529-547.

46. Mori, V., et al., *Metabolic profiling of alternative NAD biosynthetic routes in mouse tissues.* PLoS One, 2014. **9**(11): p. e113939.

47. Garten, A., et al., *Nampt: linking NAD biology, metabolism and cancer.* Trends Endocrinol Metab, 2009. **20**(3): p. 130-8.

48. Yoshino, J., J.A. Baur, and S.I. Imai, *NAD(+) Intermediates: The Biology and Therapeutic Potential of NMN and NR.* Cell Metab, 2018. **27**(3): p. 513-528.

49. Wang, J., et al., *A local mechanism mediates NAD-dependent protection of axon degeneration.* J Cell Biol, 2005. **170**(3): p. 349-55.

50. Ryu, D., et al., *NAD+ repletion improves muscle function in muscular dystrophy and counters global PARylation.* Sci Transl Med, 2016. **8**(361): p. 361ra139.

51. Yao, Z., et al., *Nicotinamide mononucleotide inhibits JNK activation to reverse Alzheimer disease.* Neurosci Lett, 2017. **647**: p. 133-140.

52. Frederick, D.W., et al., *Loss of NAD Homeostasis Leads to Progressive and Reversible Degeneration of Skeletal Muscle.* Cell Metab, 2016. **24**(2): p. 269-82.

53. Mills, K.F., et al., *Long-Term Administration of Nicotinamide Mononucleotide Mitigates Age-Associated Physiological Decline in Mice.* Cell Metab, 2016. **24**(6): p. 795-806.

54. Araki, T., Y. Sasaki, and J. Milbrandt, *Increased nuclear NAD biosynthesis and SIRT1 activation prevent axonal degeneration.* Science, 2004. **305**(5686): p. 1010-3.

55. Sasaki, Y., T. Araki, and J. Milbrandt, *Stimulation of nicotinamide adenine dinucleotide biosynthetic pathways delays axonal degeneration after axotomy.* J Neurosci, 2006. **26**(33): p. 8484-91.

56. Park, J.H., et al., *Nicotinamide mononucleotide inhibits post-ischemic NAD(+) degradation and dramatically ameliorates brain damage following global cerebral ischemia.* Neurobiol Dis, 2016. **95**: p. 102-10.

57. Sasaki, Y., et al., *Dysregulation of NAD(+) Metabolism Induces a Schwann Cell Dedifferentiation Program.* J Neurosci, 2018. **38**(29): p. 6546-6562.

58. Loris, Z.B., A.A. Pieper, and W.D. Dietrich, *The neuroprotective compound P7C3-A20 promotes neurogenesis and improves cognitive function after ischemic stroke.* Exp Neurol, 2017. **290**: p. 63-73.

59. De Jesus-Cortes, H., et al., *Neuroprotective efficacy of aminopropyl carbazoles in a mouse model of Parkinson disease.* Proc Natl Acad Sci U S A, 2012. **109**(42): p. 17010-5.

60. Tesla, R., et al., *Neuroprotective efficacy of aminopropyl carbazoles in a mouse model of amyotrophic lateral sclerosis.* Proc Natl Acad Sci U S A, 2012. **109**(42): p. 17016-21.

61. Oakey, L.A., et al., *Metabolic tracing reveals novel adaptations to skeletal muscle cell energy production pathways in response to NAD (+) depletion.* Wellcome Open Res, 2018. **3**(147): p. 147.

62. Agerholm, M., et al., *Perturbations of NAD(+) salvage systems impact mitochondrial function and energy homeostasis in mouse myoblasts and intact skeletal muscle.* Am J Physiol Endocrinol Metab, 2018. **314**(4): p. E377-E395.

63. Costford, S.R., et al., *Skeletal muscle overexpression of nicotinamide phosphoribosyl transferase in mice coupled with voluntary exercise augments exercise endurance.* Mol Metab, 2018. **7**: p. 1-11.

64. Wang, X., et al., *Deletion of Nampt in Projection Neurons of Adult Mice Leads to Motor Dysfunction, Neurodegeneration, and Death.* Cell Rep, 2017. **20**(9): p. 2184-2200.

65. Young, P., et al., *Single-neuron labeling with inducible Cre-mediated knockout in transgenic mice.* Nat Neurosci, 2008. **11**(6): p. 721-8.

66. Rongvaux, A., et al., *Nicotinamide phosphoribosyl transferase/pre-B cell colony-enhancing factor/visfatin is required for lymphocyte development and cellular resistance to genotoxic stress.* J Immunol, 2008. **181**(7): p. 4685-95.

67. Amaral, E., S. Guatimosim, and C. Guatimosim, *Using the Fluorescent Styryl Dye FM1-43 to Visualize Synaptic Vesicles Exocytosis and Endocytosis in Motor Nerve Terminals*, in *Light Microscopy: Methods and Protocols*, H. Chiarini-Garcia and R.C.N. Melo, Editors. 2011, Humana Press: Totowa, NJ. p. 137-148.

68. Leduc-Gaudet, J.P., et al., *Mitochondrial morphology is altered in atrophied skeletal muscle of aged mice.* Oncotarget, 2015. **6**(20): p. 17923-37.

69. Oki, K., et al., *Contractile dysfunction in muscle may underlie androgen-dependent motor dysfunction in spinal bulbar muscular atrophy.* J Appl Physiol (1985), 2015. **118**(7): p. 941-52.

70. Xu, Y., et al., *Defects in Neuromuscular Transmission May Underlie Motor Dysfunction in Spinal and Bulbar Muscular Atrophy.* J Neurosci, 2016. **36**(18): p. 5094-106.

71. Ploquin, C., et al., *Lack of myostatin alters intermyofibrillar mitochondria activity, unbalances redox status, and impairs tolerance to chronic repetitive contractions in muscle.* Am J Physiol Endocrinol Metab, 2012. **302**(8): p. E1000-8.

72. Ferreira, R., et al., *Subsarcolemmal and intermyofibrillar mitochondria proteome differences disclose functional specializations in skeletal muscle.* Proteomics, 2010. **10**(17): p. 3142-54.

73. Lundby, C. and R.A. Jacobs, *Adaptations of skeletal muscle mitochondria to exercise training.* Exp Physiol, 2016. **101**(1): p. 17-22.

74. Kong, L., et al., *Impaired synaptic vesicle release and immaturity of neuromuscular junctions in spinal muscular atrophy mice.* J Neurosci, 2009. **29**(3): p. 842-51.

75. Chen, F., et al., *Ubiquitin carboxyl-terminal hydrolase L1 is required for maintaining the structure and function of the neuromuscular junction.* Proc Natl Acad Sci U S A, 2010. **107**(4): p. 1636-41.

76. Liu, Y., et al., *Ubiquitin-Synaptobrevin Fusion Protein Causes Degeneration of Presynaptic Motor Terminals in Mice.* J Neurosci, 2015. **35**(33): p. 11514-31.

77. Rizzoli, S.O. and W.J. Betz, *Synaptic vesicle pools.* Nat Rev Neurosci, 2005. **6**(1): p. 57-69.

78. Maeno-Hikichi, Y., et al., *Frequency-dependent modes of synaptic vesicle endocytosis and exocytosis at adult mouse neuromuscular junctions.* J Neurosci, 2011. **31**(3): p. 1093-105.

79. Li, Y.C. and E.T. Kavalali, *Synaptic Vesicle-Recycling Machinery Components as Potential Therapeutic Targets.* Pharmacol Rev, 2017. **69**(2): p. 141-160.

80. Zefirov, A.L., et al., *The role of extracellular calcium in exo- and endocytosis of synaptic vesicles at the frog motor nerve terminals.* Neuroscience, 2006. **143**(4): p. 905-10.

81. Hosoi, N., M. Holt, and T. Sakaba, *Calcium dependence of exo- and endocytotic coupling at a glutamatergic synapse.* Neuron, 2009. **63**(2): p. 216-29.

82. Russo, A., et al., *The E3 ligase Highwire promotes synaptic transmission by targeting the NAD-synthesizing enzyme dNmnat.* EMBO Rep, 2019. **20**(3): p. e46975.

83. Li, L., W.C. Xiong, and L. Mei, *Neuromuscular Junction Formation, Aging, and Disorders.* Annu Rev Physiol, 2018. **80**(1): p. 159-188.

84. Basu, S., et al., *Acetylcholine receptor (AChR) clustering is regulated both by glycogen synthase kinase 3beta (GSK3beta)-dependent phosphorylation and the level of CLIP-associated protein 2 (CLASP2) mediating the capture of microtubule plus-ends.* J Biol Chem, 2014. **289**(44): p. 30857-30867.

85. Banks, G.B., et al., *Muscle structure influences utrophin expression in mdx mice.* PLoS Genet, 2014. **10**(6): p. e1004431.

86. Tassinari, V., et al., *Atrophy, oxidative switching and ultrastructural defects in skeletal muscle of the ataxia telangiectasia mouse model.* J Cell Sci, 2019. **132**(5): p. jcs223008.

87. Chen, S.P., et al., *Decline in titin content in rat skeletal muscle after denervation.* Muscle Nerve, 2005. **32**(6): p. 798-807.

88. Dobrowolny, G., et al., *Skeletal muscle is a primary target of SOD1G93A-mediated toxicity.* Cell Metab, 2008. **8**(5): p. 425-36.

89. Silva, K.A.S., et al., *Angiotensin II suppresses autophagy and disrupts ultrastructural morphology and function of mitochondria in mouse skeletal muscle.* J Appl Physiol (1985), 2019. **126**(6): p. 1550-1562.

90. Winter, L., et al., *Mutant desmin substantially perturbs mitochondrial morphology, function and maintenance in skeletal muscle tissue.* Acta Neuropathol, 2016. **132**(3): p. 453-73.

Chapter three: NAMPT deletion induces bioenergetic stress and cell death and inflammatory pathway activation

3.1 Abstract

Nicotinamide phosphoribosyltransferase (NAMPT) is the rate-limiting enzyme in the NAD^+ salvage pathway. Our previous studies demonstrated that deletion of NAMPT gene in projection neurons, using $Nampt^{-/-}$ conditional knockout (cKO) mice, causes neuronal degeneration, muscle atrophy, neuromuscular junction abnormalities, paralysis and eventually death. Here we conducted a combined metabolomic and transcriptional profiling study to investigate the mechanism of neuronal degeneration at the metabolite and mRNA levels after NAMPT deletion. Steady-state metabolomics demonstrated that deletion of NAMPT causes a significant decrease to the NAD^+ metabolome and a buildup of metabolic intermediates upstream of glyceraldehyde 3-phosphate dehydrogenase (GAPDH) in glycolysis. Deletion of NAMPT also increased oxidative stress. RNA-seq showed that NAMPT deletion leads to increased mRNA levels of NAD metabolic proteins, notably the NAD^+ consuming PARPs, as well as glycolytic genes preceding GAPDH (Glut1, Hk2 and PFBFK3). GSEA found activation of apoptosis, inflammation and immune responsive pathways and inhibition of neuronal/synaptic function in the cKO mice. The current study suggests that increased oxidative stress, apoptosis and neuroinflammation contribute to neurodegeneration and mouse death as a direct consequence of bioenergetic stress following NAMPT deletion.

3.2 Introduction

In chapter two, we demonstrated how NAMPT is needed for synaptic vesicle cycling, motor endplate morphology, and skeletal muscle fiber structure and function. Loss of NAMPT resulted in reduced vesicle endocytosis and exocytosis, which was improved by NMN repletion. Motor endplate and skeletal muscle structure in our conditional knockout mice also benefited from NMN treatment. Having found that activity at the NMJ was significantly altered, we next wanted to investigate a different aspect of the motor system, specifically the brain. Thus, we investigated how the metabolic and transcriptional profiles of the motor cortex are affected after deletion of NAMPT.

Nicotinamide adenine dinucleotide (NAD^+) is a co-factor required for cellular energy metabolism (i.e., glycolysis, the tricarboxylic acid (TCA) cycle and mitochondrial oxidative phosphorylation/OXPHOS). NAD^+ is also a co-substrate for many NAD^+-consuming enzymes, including sirtuins (SIRTs), Poly (ADP-ribose) polymerases (PARPs) and cluster of differentiation 38 and 157 (CD38 and CD157) [1, 2]. SIRTs, PARPs, CD38 and CD157 generate nicotinamide (NAM), which in turn serves as a precursor metabolite for the NAD^+ salvage pathway. In mammalian cells, NAD^+ is synthesized through three pathways: the *de novo*, the Preiss-Handler and the salvage pathways. Each pathway utilizes different precursors, which include tryptophan (Trp), nicotinic acid (NA), NAM, and nicotinamide riboside (NR) [1-3] (Fig 1A-B). It is widely accepted that the salvage pathway is the predominant NAD^+ biosynthetic pathway in mammalian cells. In this pathway, the first step is catalyzed by the rate-limiting enzyme nicotinamide phosphoribosyltransferase (NAMPT), which condenses NAM and 5-phosphoribosyl

pyrophosphate (PRPP) to nicotinamide mononucleotide (NMN), and the second step is catalyzed by nicotinamide mononucleotide adenylyltransferases (NMNATs), which converts NMN to NAD^+. There are three isoforms of NMNAT (NMNAT1-3) which have differing cellular and sub-cellular expression in mammalian cells. NMNAT1 is localized in the nucleus, NMNAT2 at the Golgi-cytoplasmic interface, and NMNAT3 in the mitochondria [4, 5]. $NADP^+$ availability, a structural analogue of NAD^+, is tightly associated with NAD^+. The interconversion of $NAD(P)^+$ and NAD(P)H is critical for regulating cellular redox homeostasis.

The effects of NAMPT and NAD^+ dysregulation have been widely investigated in outside of the central nervous system (CNS) [2, 6-8]. Increasing evidence suggests that NAMPT plays an important role in neuronal protection in various pathological conditions within the CNS. Previously, we demonstrated that NAMPT is primarily expressed in neurons, but not in glial cells, under normal conditions in the mouse brain and that NAMPT is neuroprotective against ischemia by suppressing mitochondrial dysfunction [9-11]. An NAD^+ decrease in the CNS was also observed in aging and neurodegenerative diseases in human and animal models [12-14]. Repletion of NAD^+ precursors, including NR, NAM, and NMN, can ameliorate pathological phenotypes of ageing related neurodegenerative diseases [15-17]. Studies have demonstrated that conditional, as opposed to inducible, NAMPT deletion results in functional changes across a variety of cell and tissue types including skeletal muscle, CaMKII neurons, adipocytes, rod and cone cells [18-22]. Recently, we showed that deletion of NAMPT in the projection neurons using conditional and inducible NAMPT knockout (cKO) mice, (i.e., $Nampt^{-/-}$ cKO mice) causes motor

neuron degeneration, neuromuscular junction (NMJ) abnormalities, muscle atrophy, body weight loss, paralysis and death [17, 23]. Our results indicate that the disruptions of bioenergetics and mitochondrial homeostasis contribute to the phenotype. To further investigate the mechanism of neuronal death in Nampt$^{-/-}$ cKO mice, we conducted a combined study of metabolomics and high-throughput RNA sequencing (RNA-Seq) to quantitatively analyze metabolic and transcriptional alterations. Using metabolomics, we studied the impact of NAMPT deletion on the NAD^+ metabolome, glycolysis, TCA cycle, and pentose phosphate pathway (PPP) intermediates, the GSH-GSSG system and other related pathways. Gene set enrichment analysis (GSEA) was also used to analyze and identify up and down regulated gene pathways. Our study suggests that activation of oxidative stress, apoptosis, inflammation and immune responsive pathways as potential mechanism of neurodegeneration after NAMPT deletion and reveals an essential role of NAMPT-mediated NAD^+ biosynthesis in maintaining energy and redox homeostasis in the CNS.

3.3 Method and materials

3.3.1 Animals

Mice were housed in the animal facility at the University of Missouri. All experimental procedures were approved by the University of Missouri Animal Care Quality Assurance Committee and were performed according to the NIH Guide for the Care and Use of Laboratory Animals and in compliance with the ARRIVE guidelines 2.0 [24]. Both male and female mice were used in the current study. Projection neuron-specific and inducible NAMPT conditional knockout (cKO) mice were generated as described in our previous study [17]. Briefly, Nampt$^{f/f}$ control (Ctrl) mice [22] were crossed with Thy1-CreER^{T2}-YFP mice [25] to obtain Nampt$^{f/f}$:Thy1-CreER^{T2}-YFP double homozygous transgenic mice confirmed by PCR amplification of their DNA from tail snips. Both Nampt$^{f/f}$ and Thy1-CreER^{T2}-YFP transgenic mouse lines have a C57BL/6J background. Deletion of NAMPT in double transgenic mice was achieved by administration of tamoxifen (TAM, 200 mg/kg in sunflower seed oil, T5648, Sigma, MO) for 5 consecutive days at 8-weeks old by oral gavage and designated as Thy1-YFP-Nampt$^{-/-}$ conditional knockout mice (hereafter, the Nampt cKO mice) [17]. Mice were sacrificed for experiments 3 weeks after the last injection of tamoxifen.

3.3.2 Metabolomic and transcriptional profiling of cortical tissues

Motor cortical tissues were isolated from the control and Nampt cKO mice for metabolomic and transcriptional profiling. Steady-state metabolomic analysis was done using LC/MS in CRI's Metabolomics Facility at UT Southwestern Medical Center (https://cri.utsw.edu/facilities/metabolomics-facility/) [26]. RNA-sequencing was

conducted by LC Sciences (Houston, TX).

3.3.3 Preparation of mouse cortical tissues for metabolomic profiling and metabolomic analysis

After a mouse was decapitated, the brain was rapidly taken out and placed in brain matrix on ice and the motor cortical regions of both hemispheres were isolated with a razor blade and placed in a 1.5 ml pre-weighed autoclaved Eppendorf tube. The brain tissue was put in pre-chilled (-77 °C) 900 µl mixture of 80% liquid chromatograph-mass spectrometer (LC/MS) grade methanol (Cat. No. MX0486, EMD Millipore)/water, vortexed for 30 sec and kept in -20 °C until use. The brain tissue was homogenized, vortexed rigorously for 1 min, centrifuged at 13,300g for 15 min in a refrigerated centrifuge (4 °C). The protein pellet was collected for protein quantitation. The metabolite-containing supernatant (80-90% of all solution, ~850 µl) was transferred to a new 1.5 ml Eppendorf tube, and dried using a SpeedVac. The dried metabolite pellets were kept at -80 °C until performing metabolomic profiling analysis.

The metabolites of each tube were reconstituted with 50 µl of 0.03% formic acid in analytical-grade water, vortexed and centrifuged at 14,000g for 14 min to remove debris, and 40 µl supernatant removed for metabolomic profiling. Steady-state metabolomic analysis was done using LC/MS in CRI's Metabolomics Facility at UT Southwestern Medical Center (https://cri.utsw.edu/facilities/metabolomics-facility/) (Xiong *et al*, 2020). Samples were then injected into a SCIEX QTRAP 5500 liquid chromatograph/triple quadrupole mass spectrometer (SCIEX, Framingham, MA). Separation was achieved on a Phenomenex Synergi Polar-RP HPLC column (150 × 2 mm, 4 µm, 80 Å) using a Nexera

Ultra-High-Performance Liquid Chromatograph (UHPLC) system (Shimadzu Corporation, Columbia, MD). The mobile phases employed were 0.03% formic acid in water (A) and 0.03% formic acid in acetonitrile (B). The gradient program was: 0-3 min, 100% A; 3-15 min, 100%-0% A; 15-21 min, 0% A; 21-21.1 min, 0%-100% A; 21.1-30 min, 100% A. The flow rate was 0.5 ml/min, and the injection volume was 20 µl. The mass spectrometer was used with an electrospray ionization (ESI) source operated in multiple reaction monitoring (MRM) mode. Samples were analyzed in positive/negative switching mode. The declustering potential (DP), collision energy (CE), and collision cell exit potential (CXP) were optimized for each metabolite by directly infusing the reference standards using a syringe pump prior to sample analysis. MRM data were acquired using Analyst 1.6.3 software from SCIEX.

3.3.4 Data analysis for metabolites

Unsupervised and supervised multivariate data analysis approaches including principal component analysis (PCA), hierarchical clustering, and partial least squares discriminant analysis (PLS-DA) were performed using MetaboAnalyst 4.0 software (https://www.metaboanalyst.ca/) [1]. We performed feature selection in PLS-DA to identify metabolites that maximize separation between the two groups of the Ctrl and cKO mice by rotating the PCA components. The importance of a metabolite in the model is determined by the Variable Importance in Projection (VIP) score, which is calculated as a weighted sum of the squared correlations between this metabolite and the derived PLS-DA components. The VIP score of a metabolite indicates its intensity of association with the PLS-DA components that best distinguish between the two groups. By definition, the

average of squared VIP scores equals 1, and by convention a VIP score of greater than 1 is used as a criterion for variable selection [2]. There, metabolites with a VIP score > 1 were reported.

3.3.5 RNA-sequencing

RNA-sequencing of brain cortical tissues was conducted by LC Sciences (Houston, TX). Total RNA was extracted using the miRNeasy kit (QIAQEN Inc., Germantown, MD) according to the manufacturer protocol. Samples with high RNA quality were used to construct poly A selected paired-end sequencing libraries (150 bp) using Illumina® TruSeq® Stranded mRNA sample preparation kits (Cat. No. RS-122-2101, Illumina, San Diego, CA). The constructed sequencing libraries were subject to sequencing with Illumina Novaseq^{TM} 6000 platform. Prior to assembly, reads containing sequencing adaptors, reads containing sequencing primers, and sequences with quality score Q lower than 20 were removed. The cleaned sequencing reads were aligned to reference genome using HISAT2 package [3]. Aligned reads of individual samples were assembled using StringTie [4]. Transcriptomes from all samples were then merged to reconstruct a comprehensive transcriptome using a proprietary Perl script of LC Sciences. Following transcriptome reconstruction, expression levels were reported as counts per million (CPM) values by StringTie.

3.3.6 Identification of DEGs and analyses of GO and KEGG pathways

Empirical analysis of digital gene expression in R (edgeR) package v3.12.1 in the Bioconductor was used to analyze DEGs in the assembled transcriptome [5]. For comparison of transcript counts between Nampt cKO and Nampt$^{f/f}$ Ctrl mice, primary

parameters such as false discovery rate (FDR, *i.e.*, P_{adj}), fold change (FC) were obtained using edgeR. Unigenes with $P_{adj}<0.05$ and the fold change (FC) threshold of $|Log_2(FC)|>1$ was considered as DEGs. Heatmaps were generated by plotting these values using heatmap in R with row scaling to produce z-score values.

3.3.7 Gene set enrichment analysis (GSEA) using pre-ranked gene list

The mechanisms underlying the relationship between NAD metabolism and cell death were explored with GSEA [8-10]. GSEA was used to analyze specific gene sets against our pre-ranked gene list with Enrichment Score (ES) (Ctrl versus Nampt cKO mice) using the metrics algorithm by applying the sign of Log_2 (FC) and $-Log_{10}$ (P_{adj}), and statistical result of edgeR (see **Table S8**). A comprehensive Gene Set Knowledge Base (GSKB) of 4603 gene sets for metabolic pathway analysis in mouse were generated [8]. The GSKB contains various gene sets including pathways and functional categories. Pre-ranked (.rnk) gene list and selected gene sets were used as input for analysis using software GSEA v4.0.3 (WWW.gsea-msigdb.org/gsea/index.jsp). GSEA calculates an ES by scanning a ranked-ordered gene list according to significance of differential expression, *i.e.*, $-Log_{10}P_{adj}$, increasing a running-sum statistic when a gene is in the gene set and decreasing it when it is not. The top of this list (red) contains genes upregulated in cKO mice while the bottom of the list (blue) represents downregulated genes in cKO mice. The number of permutations were set at 1000, enrichment statistics were set at 'weighted'. Parameters of the size of gene in gene sets, ES, normalized ES (NES), false discovery rate q-value (FDR q-val) were obtained. Gene sets were considered significantly enriched with FDR q-val<0.1, |NES|>1.5, and gene size >5.

3.3.8 Data analysis and statistics

Data for individual metabolite level and gene expression between Ctrl and Nampt cKO mice were expressed as means ± SD. Statistical comparisons were made by t-test for two groups. P values were indicated in the figure legends.

3.4 Results

3.4.1 Deletion of NAMPT in the projection neurons reduces brain NAD^+ metabolome and causes the impairment of glycolysis

In order to identify the molecular mechanism that potentially causes neuronal degeneration and death in Nampt cKO mice [17], we conducted a metabolomic study on adult Nampt cKO and the age-matched $Nampt^{f/f}$ Ctrl mice to determine the metabolite contents for different metabolic pathways. Three weeks after the final TAM injection, motor cortical tissues from cKO and Ctrl mice were dissected for LC/MS-based metabolomic profiling (Fig. 3.1C-D). We identified 158 metabolites, 56 of which were significantly altered (30 decreased, 26 increased). Univariate analyses of all metabolites using a volcano plot shows up- and down-regulations of multiple metabolites in cKO mice (Fig. 3.1E). Multivariate analyses using PCA scores, dendrogram of metabolic tree, and the heatmap and VIP scores of the top 25 metabolites show distinct metabolic profiles between Ctrl and cKO mice (Fig. 3.1F-I).

As NAMPT is the rate-limiting enzyme in the NAD^+ salvage pathway, we examined NAD^+ and its related metabolites (hereafter, the NAD^+ metabolome). Our results show that NAD^+, NAM, nicotinate, $NADP^+$, ADP-ribose, cADP-ribose (the product generated by CD38 and CD157 activity [27, 28]), adenine, AMP and dAMP were largely reduced in cKO mice as compared with the Ctrl mice, while adenosine and ADP were unchanged (Fig. 3.1J). Of all metabolites identified, the top 5 most significantly reduced metabolites were NAD^+, cADP-ribose, ADP-ribose, NAM, and dAMP which, apart from being in the NAD^+ metabolome, are important for ATP production. This decrease in NAD^+

levels in Nampt cKO mice is associated with ATP reduction and consistent with our previous study [10, 17].

These data suggest that neuronal deletion of NAMPT could cause a detrimental effect on metabolic processes, redox homeostasis, energy production and signaling pathways that require NAD^+ or $NADP^+$. It is important to note that methylated NAM (MNAM) is highly increased in cKO mice, suggesting the elimination of NAM by nicotinamide N-methyltransferase (NNMT) (Fig. 3.1J). The increase in MNAM is likely due to the shutdown of NAM conversation to NMN by NAMPT in cKO mice, and consequently, the equilibrium of NAM conversion to MNAM catalyzed by NNMT shifts towards MNAM.

Next, we examined the impact of NAMPT deletion on metabolites in glycolysis, the TCA cycle and other related pathways (Fig. 3.2A). Our data show accumulation of intermediate metabolites upstream of GAPDH in glycolysis, G-6P/F-6P, F-1,6BP (Fructose-1,6-biphosphate) and DHAP (dihydroxyacetone-phosphate), while metabolites downstream were not different (Fig. 3.2B). This is likely the direct result of lower NAD^+ concentration in cKO mice which reduces the activity of the NAD^+-dependent GAPDH. Generally, these data indicate that deletion of NAMPT causes impaired ATP production in glycolysis, further confirming cellular energy stress.

There were no significant changes to TCA cycle intermediates (Fig. 3.2C). The glyoxylate cycle is a variation of the TCA cycle but is an anabolic pathway that converts acetyl-CoA to succinate for carbohydrates biosynthesis [29]. We detected that glyoxylate was significantly increased in cKO mice. Likewise, 2-HG, which is generated from

isocitrate and requires NADPH, was also lower, presumably resulting from reduced NADPH levels.

Amino acids (AAs) are the building blocks of proteins and many of them are associated with the TCA cycle (Fig. 3.2A). Among all AAs, aspartate had the highest increase in cKO mice (Fig. 3.2D). The accumulation of aspartate is likely due to less conversion of malate to oxaloacetate (OAA) in the TCA cycle, which requires NAD^+. Isoleucine, proline, phenylalanine and histidine were also significantly increased, while tyrosine, methionine and glutamate were decreased in the cKO mice. Of note, glutamate, the most important neurotransmitter and a substrate for GSH synthesis, was reduced in cKO mice.

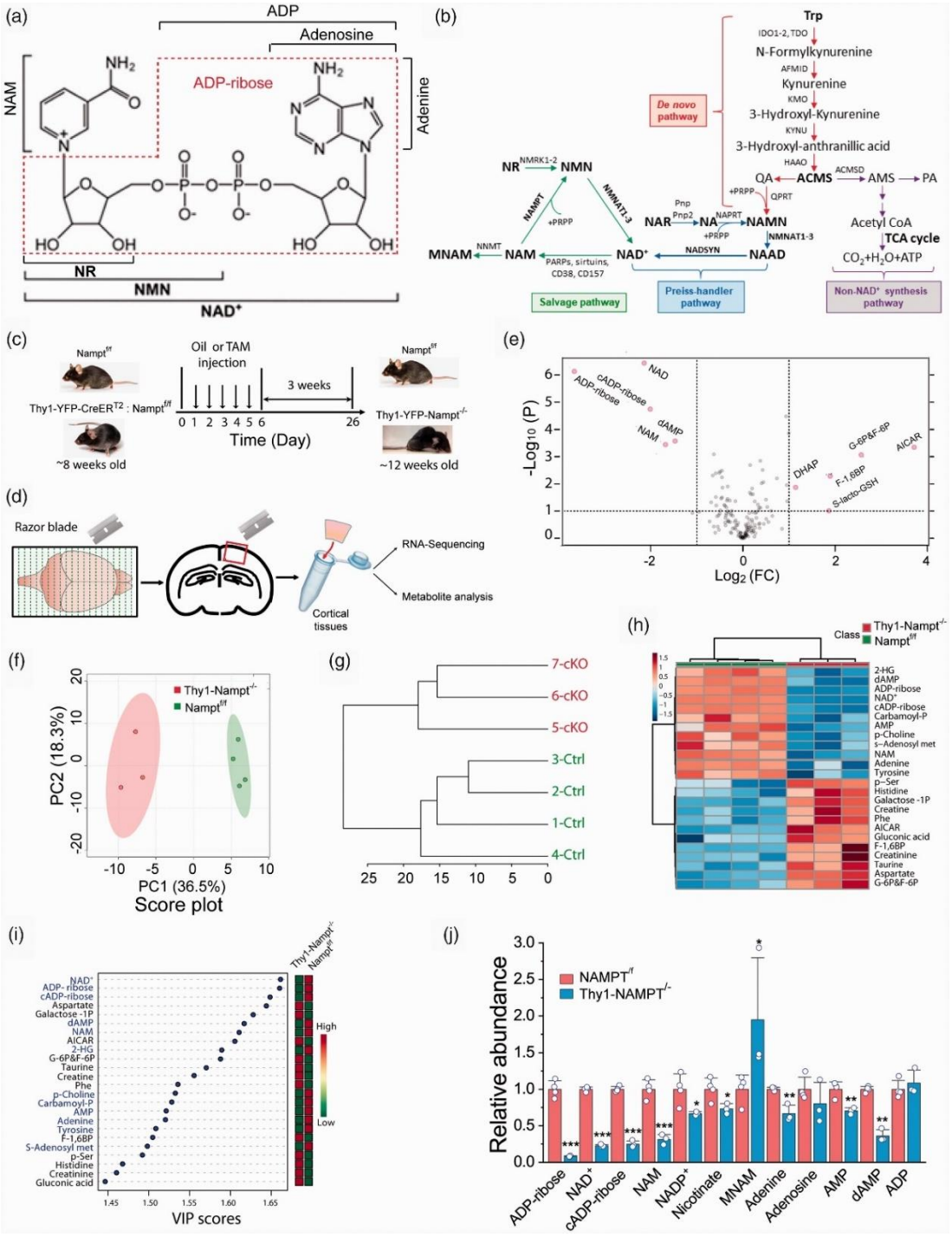

Figure 3.1. Deletion of NAMPT in the projection neurons reduces NAD⁺ metabolome and bioenergetics. A) NAD⁺ structure. **B)** NAD⁺ biosynthesis pathways. **C-D**) Experimental timeline. Nampt$^{f/f}$ and Thy1-YFP-CreER^{T2}:Nampt$^{f/f}$ mice were injected with oil and TAM for 5 consecutive days (C) and were

sacrificed for metabolomics and RNA-seq 3 weeks after the last injection (D). **E**) Volcano plot of 158 metabolites with P value threshold of 0.1. FC≥2 was set in volcano plot. The red circles represent features above the threshold. **F**) Principal component analysis (PCA) of 158 metabolites. Top two PCs explain 54.8% (36.5% and 18.3%) of the total variance. **G**) Dendrogram of metabolic tree from 158 metabolites. **H**) Heatmap of top 25 metabolites. **I**) Variable importance in projection (VIP) score of top 25 metabolites from partial least squares discriminant analysis (PLS-DA). The metabolites enriched in the cKO mice are labeled with blue and reduced with black. The abundance of each metabolite is increased (red) or reduced (green) in the cKO mice is indicated in the column on the right. The colored boxes indicate the relative concentrations of the corresponding metabolites in each group. **J**) Relative abundance of NAD^+ metabolome. N=4 Ctrl, 3 cKO mice. *P<0.05, **P<0.01, ***P<0.005, t-test with 2-tail distribution. Formal tests for normality were not used to assess data distribution.

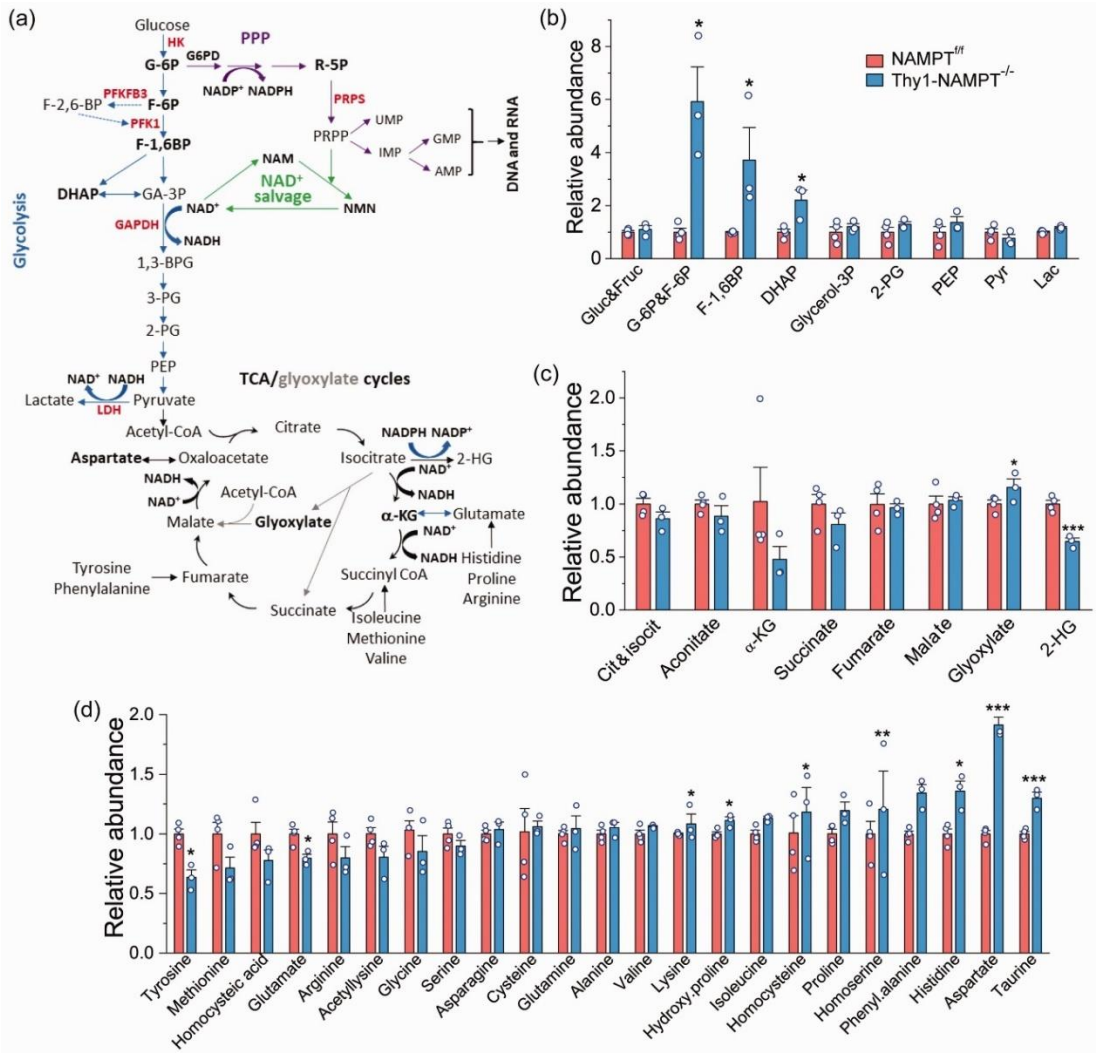

Figure 3.2. Metabolite analysis of Nampt^{f} Ctrl and Nampt$^{-/-}$ cKO mice. A) Metabolic pathways including glycolysis, PPP, TCA/glyoxylate cycles, NAD^+ salvage and AA synthesis. **B-D**) Relative abundance of metabolites in glycolysis (B) and TCA/Glyoxylate cycles (C), and of AAs (D). Note: G-6P and F-6P cannot be differentiated, so the total of them were measured. N=4 Ctrl, 3 cKO mice. *P<0.05, **P<0.01, ***P<0.005, t-test with 2-tail distribution. Formal tests for normality were not used to assess data distribution.

3.4.2 Deletion of NAMPT increases oxidative stress

The PPP is a metabolic pathway parallel to glycolysis and is also a major pathway for glucose metabolism (Fig. 3.3A). It generates a pentose sugar, ribose 5-phosphate (R-5P), for nucleotide synthesis; another key function of the PPP is to maintain cellular redox homeostasis by producing NADPH. The glycolytic intermediate G-6P can either enter glycolysis to generate ATP or the PPP to generate pentoses and NADPH from $NADP^+$ in the cytosol. Noticeably, R-5P, was significantly accumulated, suggesting the buildup of G-6P causes shunting from glycolysis to the PPP (Fig. 3.3B). R-5P can be converted to PRPP by PRPP synthetase (PRPS). PRPP is not only a precursor for the synthesis of nucleobases, nucleosides and nucleotides but is also incorporated into the NAD^+ salvage pathway by NAMPT (Fig. 3.1B & 3.3A). The accumulation of R-5P is also possibly due to the reduction of ATP which is involved in conversion of R-5P to PRPP. Consistent with the accumulation of R-5P, cKO mice also exhibited reduced levels of nucleobases, nucleosides and nucleotides including adenine, AMP, dAMP, guanine, GMP, and deoxyuridine (Fig. 3.1E & 3.3D).

In the PPP, the conversion of G-6P to 6P-glucono-δ-lactone is regulated by both glucose 6-phosphate dehydrogenase (G6PD) and $NADP^+$ availability. NADPH produced from this step is critical for maintaining cellular redox status and plays as a direct role in regulating the production of reduced glutathione (GSH), the major endogenous antioxidant produced by cells [30, 31]. Reduction of oxidized glutathione (GSSG) to GSH by glutathione reductase (GSR) is coupled to NADPH generated by G6PD in the PPP (Fig. 3.3A). The GSH/GSSG ratio has been used as a marker of oxidative stress. We found that

GSH levels and the GSH/GSSG ratio were significantly reduced in cKO mice (by 21.3% and 48.7%, respectively) (Fig. 3.3B). A reduced GSH/GSSG ratio indicates enhanced oxidative stress in cKO mice, potentially a major reason for the neurodegeneration and death of Nampt cKO mice. Noticeably, S-lactoylglutathione (SLG), an intermediate related to GSH, was highly upregulated in the cKO mice.

Meanwhile, we found that AICAR (5-aminoimidazole-4-carboxamide ribonucleotide), a downstream intermediate of PRPP, upstream intermediate of inosine monophosphate (IMP), and analog of adenosine monophosphate (AMP), has the highest FC increase in cKO mice (Fig. 3.3C). AICAR is an activator of adenosine 5′ monophosphate (AMP)-dependent protein kinase (AMPK), a key sensor of cellular energy [32, 33]. Given that AICAR is highly increased in the Nampt cKO mice, it might activate AMPK following NAMPT deletion.

ATP is not solely produced from glycolysis and OXPHOS, but also can be regenerated through the molecule phosphocreatine (P-creatine), the main storage form of energy in the cells. In this reaction, creatine kinase (CK) transfers a phosphate from P-creatine to ADP, which plays a particularly important role in controlling cellular energy homeostasis (Fig. 3.3E) [34]. This produces ATP and creatine, an AA. We found deletion of NAMPT caused the accumulation of creatine and creatinine (Fig. 3.3F). Together with the reduction of adenine, AMP and dAMP (Fig. 3.1E), our data show that deletion of NAMPT impairs ATP regeneration in Nampt cKO mice, causing further energy distress.

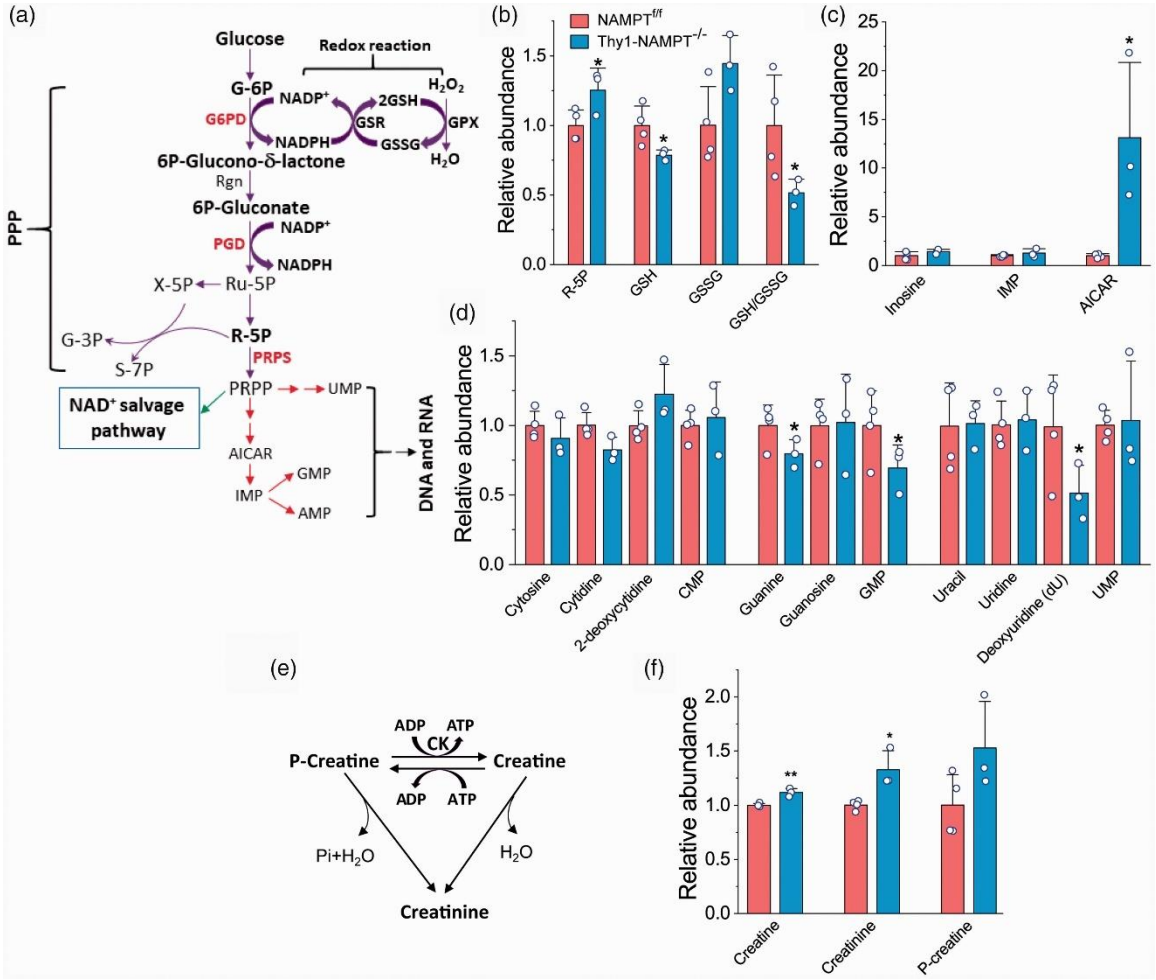

Figure 3.3. The effect of NAMPT deletion on oxidative stress, nucleotides and ATP regeneration. A) PPP and related pathways. PPP is coupled to GSSG production through NADP. PRPP is the backbone and precursor for nucleoside and nucleotide. **B)** R-5P, GSH, GSSG and GSH/GSSG ratio. **C)** Inosine, inosine monophosphate (IMP) and AICAR. **D**) Base, nucleoside and nucleotide. **E)** Conversion among Creatine, Creatinine and P-Creatine. **F**) Accumulation of Creatine, Creatinine and P-Creatine after NAMPT deletion. *P<0.05, **P<0.01, t-test with 2-tail distribution. Formal tests for normality were not used to assess data distribution.

3.4.3 NAMPT deletion in projection neurons dysregulates the expression of genes encoding enzymes in NAD metabolism

While metabolomic analysis can estimate the contents of metabolites in various metabolic pathways, RNA-seq is one of the most effective methods for serial analyses of expression of thousands of genes encoding enzymes and proteins [35, 36]. Thus, we performed RNA-sequencing (RNA-seq) on the motor cortex attempting to elucidate the underlying mechanism of the neuronal death after NAMPT deletion in the projection neurons. The RNA-seq data found 22611 native features and the PCA plot shows two distinct clusters between cKO and Ctrl mice (Fig. 3.4A). By setting thresholds of $|Log_2(FC)|>1$ and $P_{adj}<0.05$, we found 1604 differentially expressed genes (DEGs; 1186 upregulated, 418 downregulated) after deletion of NAMPT (Fig. 3.4B). This indicates that deletion of NAMPT in the projection neurons causes a large disruption in gene expression, consistent with the distinct phenotype of the cKO mice [17].

We have shown that the Nampt cKO mice exhibited a dramatically reduced NAD^+ metabolome (Fig. 3.1E). To determine whether NAMPT deletion also affects genes related to NAD metabolism, we first compared expression of salvage pathway genes. Indeed, the mRNA expression levels of NAMPT is reduced in cKO mice from (Ctrl=11.07±0.35 vs cKO=8.26± 0.85; p=0.038), while NMNAT1-3 were not significantly different from the Ctrl mice (Fig. 3.4C), consistent with the reduction of NAMPT protein levels in our previous study [17]. Because NAD^+ levels are determined not only by the salvage pathway but also by other biosynthetic and consuming pathways, we analyzed of a set of 71 genes encoding enzymes involved in NAD^+ biosynthesis (the salvage, *de novo* and Preiss-Handler pathways), NAD(H) phosphorylation, NADP(H) dephosphorylation, NAD^+-dependent deacetylation, ADP-ribosylation, cADP-ribose formation, NAM

methylation/oxidation, and other related functions in transport, binding, redox and regulation [37]. The volcano plot displays the up and down-regulated genes and the heatmap shows the distinct pattern of top 13 genes ($|Log_2(FC)|>1$ and $P_{adj}<0.05$) in NAD metabolism (Fig. 3.4D-E).

Nicotinamide riboside kinases, NMRK1 and NMRK2, were considered as a part of salvage pathway and catalyze the phosphorylation of nicotinamide riboside (NR) and nicotinic acid riboside (NaR) to form nicotinamide mononucleotide (NMN) and nicotinic acid mononucleotide (NaMN) (see Fig. 3.1B). We found NMRK2 was significantly upregulated while NMRK1 remained similar after NAMPT deletion (Fig. 3.4D). NNMT, which catalyzes the N-methylation of NAM and other pyridines to form pyridinium ions, mRNA levels are largely increased (Fig. 3.4D-E). Increased NNMT expression will expectedly cause enhanced elimination of NAM and increased MNAM, thus reducing NAD^+ synthesis in the salvage pathway, which is confirmed by metabolomic analysis (Fig. 3.1J). Analysis of genes in *de novo* and Preiss-Handler pathways, to determine whether there are compensatory effects for NAD^+ biosynthesis in cKO mice, found that only Ido1, the rate-limiting enzyme in *de novo* pathway, was significantly reduced (Fig. 3.4D-E). NAD^+-consuming enzymes include PARPs, SIRTs and CD38/157 (Fig. 3.1B) [2]. Importantly, mRNA levels of several genes in the PARP family including PARP3, 7, 9-10, 12-14 were significantly upregulated but expression of the SIRT genes was not altered. NAD^+-consuming CD157 was also highly upregulated in cKO mice (Fig. 3.4D-E). Moreover, mRNA levels of genes Slc28a2 and Slc28a4, which encode nucleotide transporters, were highly upregulated (Fig. 3.4D-E). Thus, NAMPT deletion causes

changes in the expression of many other genes related to NAD metabolism, which may further contribute to the overall reduction of NAD^+ content.

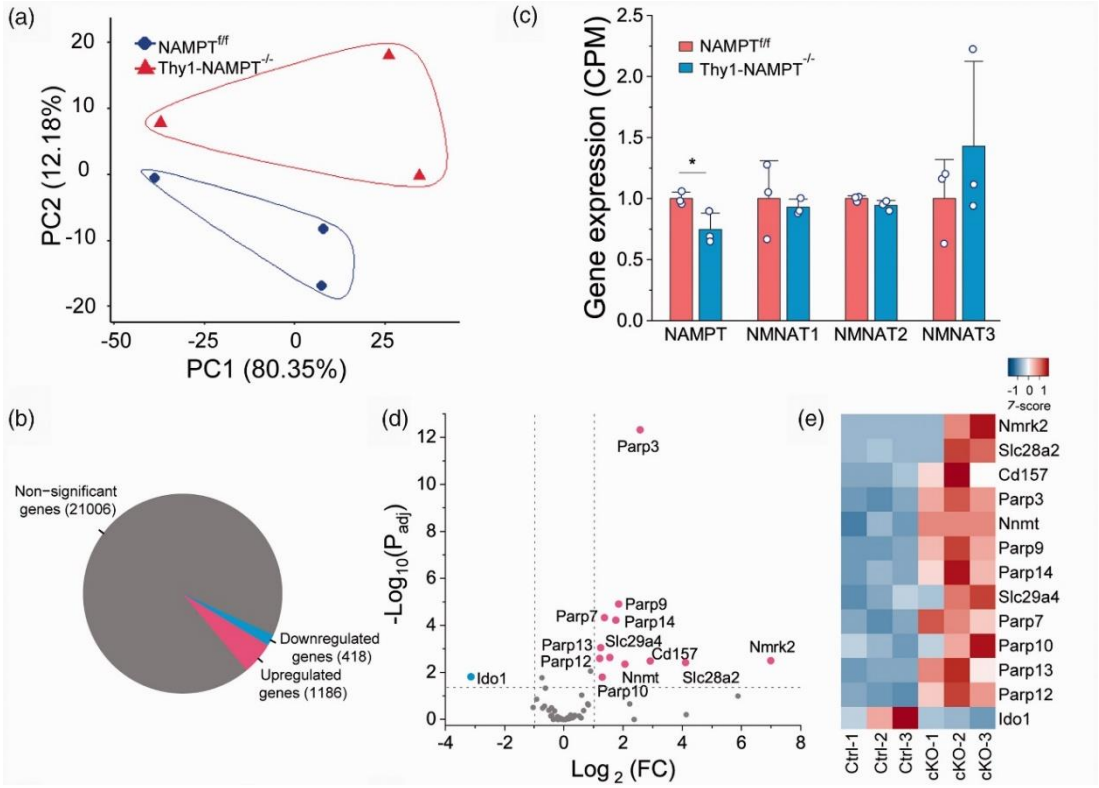

Figure 3.4. RNA-seq analysis of gene expression involving NAD metabolism and cell-type specific markers in Nampt$^{f/f}$ Ctrl and Nampt$^{-/-}$ cKO mice. A) PCA analysis score plot. **B**) The Venn diagram represented by differential expressed genes. **C**) Relative expression of genes in the NAD^+ salvage pathway. *P<0.05, t-test with 2-tail distribution. Formal tests for normality were not used to assess data distribution. **D**) Volcano plot of $\log_2$ (FC) vs $\log_{10}$ (P_{adj}) showing up- and down-regulated genes involved in NAD metabolism in the cKO mice. **E**) Heatmap of genes above the threshold of FC>2 and P_{adj}<0.05 in the NAD metabolism. N=3 for Ctrl, 3 cKO mice.

3.4.4 NAMPT deletion causes the upregulation of important genes in energy metabolism and redox status-related pathways

As NAD^+ is an essential co-factor in energy producing pathways, next we examined gene expression of enzymes involved in glycolysis, the TCA cycle and OXPHOS, which are critical for energy metabolism. mRNA levels of Glut1, Hk2 and Pfkfb3, which encode enzymes in the 3 steps before GAPDH in glycolysis, were significantly increased in Nampt cKO mice (Fig. 3.5A & Fig. 3.6A-C). Upregulation of these genes suggests that cKO mice responded to the energy stress by increasing glycolytic metabolism, which has a fast energy (ATP) production. Notably, the glycolytic gene GAPDH whose protein product uses NAD^+ as a co-factor, remained unchanged after NAMPT deletion, and genes downstream of GAPDH were not changed either. No genes in the TCA cycle had significantly altered mRNA levels (Fig. 3.5B). In OXPHOS, mRNA levels of Tcirg1, which encodes vacuolar H+-ATPase (V-ATPase) and acts as a pump to move protons across the membrane [38], was increased; the mRNA levels of COX IV genes Cox6a2 and Cox8b, which encode the terminal enzyme of the mitochondrial respiratory chain, were reduced (Fig. 3.5E). The reduced expression of COX IV genes further suggests energy stress in the cKO mice.

Based on the oxidative stress metabolites found (Fig. 3.3A), we analyzed the genes in the PPP and GSH-GSSG system that are important for maintaining redox balance and antioxidant capacity. GSR in GSH-GSSG system was found significantly upregulated in cKO mice (Fig. 3.5C & Fig. 3.6D), suggesting conversion of glutathione GSSG to GSH, which is couple to NADPH generated by G6PD in the PPP, is increased. The glutathione peroxidase (Gpx) proteins catalyze the reduction of hydrogen peroxide, organic and lipid

hydroperoxides, and thereby protect cells against oxidative damage. Gpx1 and Gpx7 were significantly upregulated in cKO mice *(*Fig. 3.5C & Fig. 3.6E-F*)*. G6PD (G6pdx) and PGD, which encode $NADP^+$-dependent enzymes in the PPP, were significantly increased after NAMPT deletion (Fig. 3.4D & Fig. 3.6G-H). These results suggest that there is an attempt to increase antioxidant capacity in cKO mice following NAMPT deletion.

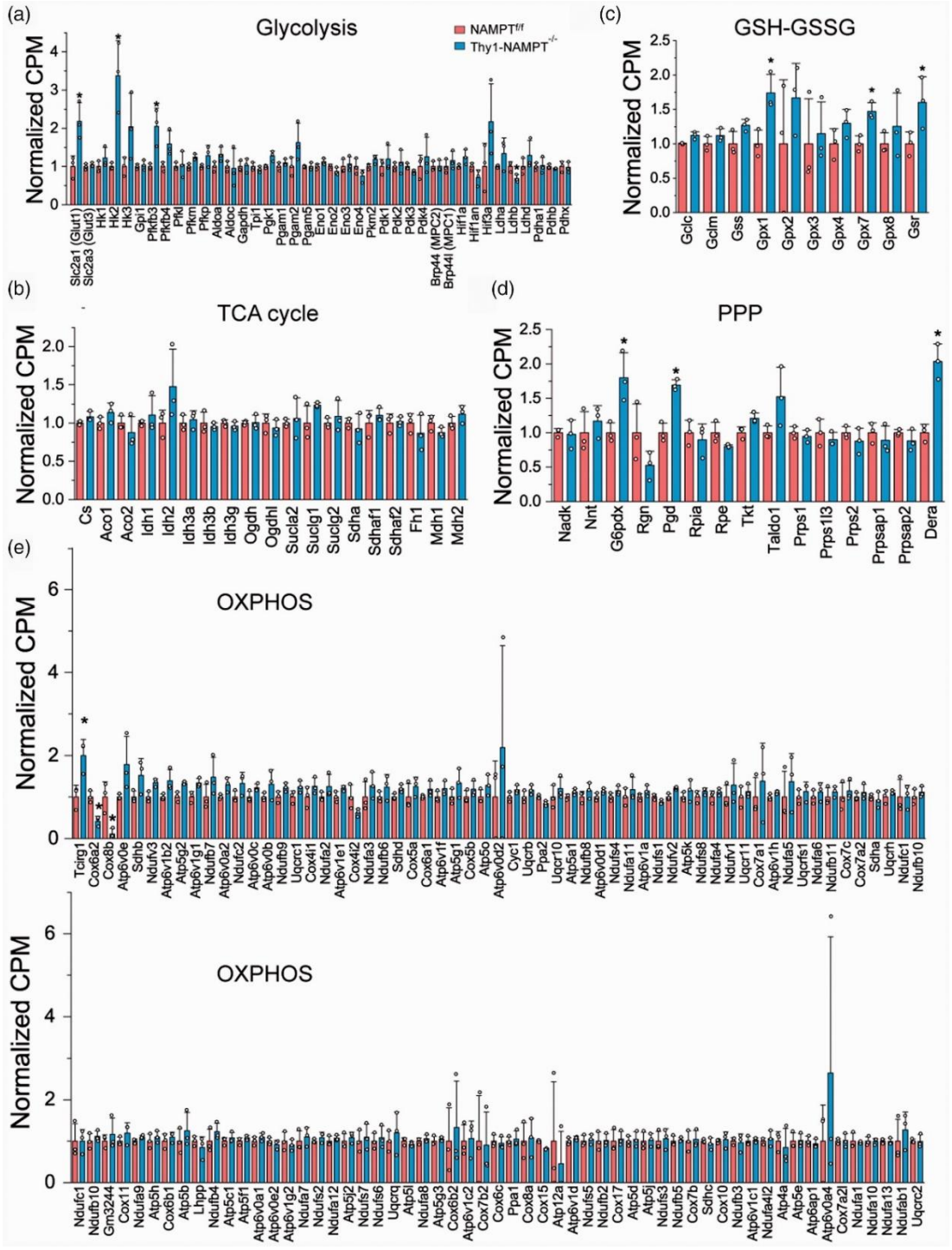
(a)
Glycolysis
NAMPT f/f
Thy1-NAMPT -/-
Normalized CPM
Slc2a1 (Glut1)
Slc2a3 (Glut3)
Hk1
Hk2
Hk3
Gpi1
Pfkfb3
Pfkfb4
Pfkl
Pfkm
Pfkp
Aldoa
Aldoc
Gapdh
Tpi1
Pgk1
Pgam1
Pgam2
Pgam5
Eno1
Eno2
Eno3
Eno4
Pkm2
Pdk1
Pdk2
Pdk3
Pdk4
Brp44 (MPC2)
Brp44l (MPC1)
Hif1a
Hif1an
Hif3a
Ldha
Ldhb
Ldhd
Pdha1
Pdhb
Pdhx
(c)
GSH-GSSG
Normalized CPM
Gclc
Gclm
Gss
Gpx1
Gpx2
Gpx3
Gpx4
Gpx7
Gpx8
Gsr
(b)
TCA cycle
Normalized CPM
Cs
Aco1
Aco2
Idh1
Idh2
Idh3a
Idh3b
Idh3g
Ogdh
Ogdhl
Sucla2
Suclg1
Suclg2
Sdha
Sdhaf1
Sdhaf2
Fh1
Mdh1
Mdh2
(d)
PPP
Normalized CPM
Nadk
Nnt
G6pdx
Rgn
Pgd
Rpia
Rpe
Tkt
Taldo1
Prps1
Prps1l3
Prps2
Prpsap1
Prpsap2
Dera
(e)
OXPHOS
Normalized CPM
Tcirg1
Cox6a2
Cox8b
Atp6v0e
Sdhb
Ndufv3
Atp6v1b2
Atp5g2
Atp6v1g1
Ndufb7
Atp6v0a2
Ndufc2
Atp6v0c
Atp6v0b
Ndufb9
Uqcrc1
Cox4i1
Ndufa2
Atp6v1e1
Cox4i2
Ndufa3
Ndufb6
Sdhd
Cox5a
Cox6a1
Atp6v1f
Atp5g1
Cox5b
Atp5o
Atp6v0d2
Cyc1
Uqcrb
Ppa2
Uqcr10
Atp5a1
Ndufb8
Atp6v0d1
Ndufs4
Ndufa11
Atp6v1a
Ndufs1
Ndufv2
Atp5k
Ndufs8
Ndufa4
Ndufv1
Uqcr11
Cox7a1
Atp6v1h
Ndufa5
Uqcrfs1
Ndufa6
Ndufb11
Cox7c
Cox7a2
Sdha
Uqcrh
Ndufc1
Ndufb10
OXPHOS
Normalized CPM
Ndufc1
Ndufb10
Gm3244
Cox11
Ndufa9
Atp5h
Cox6b1
Atp5b
Lhpp
Ndufb4
Atp5c1
Atp5f1
Atp6v0a1
Atp6v0e2
Atp6v1g2
Ndufa7
Ndufs2
Ndufa12
Atp5j2
Ndufs7
Ndufs6
Uqcrq
Atp5l
Ndufa8
Atp5g3
Cox6b2
Atp6v1c2
Cox7b2
Cox6c
Ppa1
Cox8a
Cox15
Atp12a
Atp6v1d
Ndufs5
Ndufb2
Cox17
Atp5d
Atp5j
Ndufs3
Ndufb5
Cox7b
Sdhc
Cox10
Ndufb3
Atp6v1c1
Ndufa4l2
Atp4a
Atp5e
Atp6ap1
Atp6v0a4
Cox7a2l
Ndufa1
Ndufa10
Ndufa13
Ndufab1
Uqcrc2

Figure 3.5. Changes of gene expression in different metabolic pathways after NAMPT deletion. A-D) Relative mRNA levels of genes in glycolysis (A), the TCA cycle (B), GSH-GSSG system (C), PPP (D) and OXPHOS (E). *P_{adj}<0.05 and Fc>2. N=3 mice in each group.

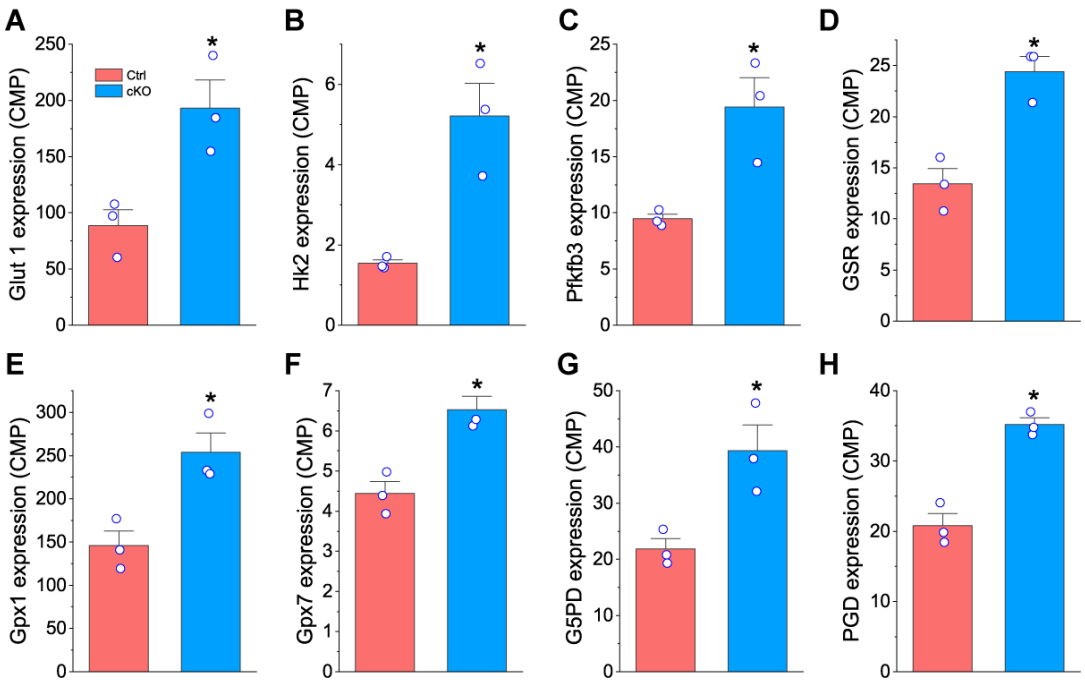

Figure 3.6. Deletion of NAMPT causes upregulation of genes in glycolysis and redox-related pathway. **A-C)** Upregulation of Glut1, HK2 and Pfkfb3 genes in glycolysis. **D-F)** Upregulation of Gpx1, Gpx7 and GSR in GSH-GSSG system. **G-H)** Upregulation of G5PD and PGD in PPP. *P>0.05, t-test. N=3 mice in each group.

3.4.5 GSEA shows increased activation of inflammation, immune response and cell death pathways, and reduced neuronal function after NAMPT deletion

Using a pre-ranked gene list, GSEA can determine whether *a priori* defined gene sets show any statistically significant and concordant differences between two phenotypes. In GSEA, all the genes are provided, ranked and weighed by FC in the analysis without a cutoff. This analysis also enables the detection of subtle effects of multiple genes in the same gene set that might be missed by assessing genes individually. We conducted GSEA of 4603 metabolic pathways from the GSKB database, including REACTOME, KEGG, EHMN and MouseCye [39-42]. Using our pre-ranked gene list and thresholds of NES>1.5 and FDR p-val<0.05, we identified 9 downregulated pathways and 206 upregulated pathways in cKO mice. We found that apoptosis, NF-κB, cytokine-cytokine receptor interaction, JAK-STAT, and complement and-coagulation cascade signaling pathways were highly upregulated, while glutamatergic synapse, GABAergic synapse and cholinergic synapse were down-regulated in cKO mice (Fig. 3.7A-B). GSEA and heatmap plots of gene sets show many genes in upregulated pathways (i.e., apoptosis and NF-κB signaling) were upregulated, while many genes in downregulated pathways (i.e., glutamatergic and GABAergic synapse) were downregulated (Fig. 3.7C-D). These results demonstrate that pathways related to immune response, inflammation and cell death were upregulated, while pathways related to synaptic function were downregulated after NAMPT deletion.

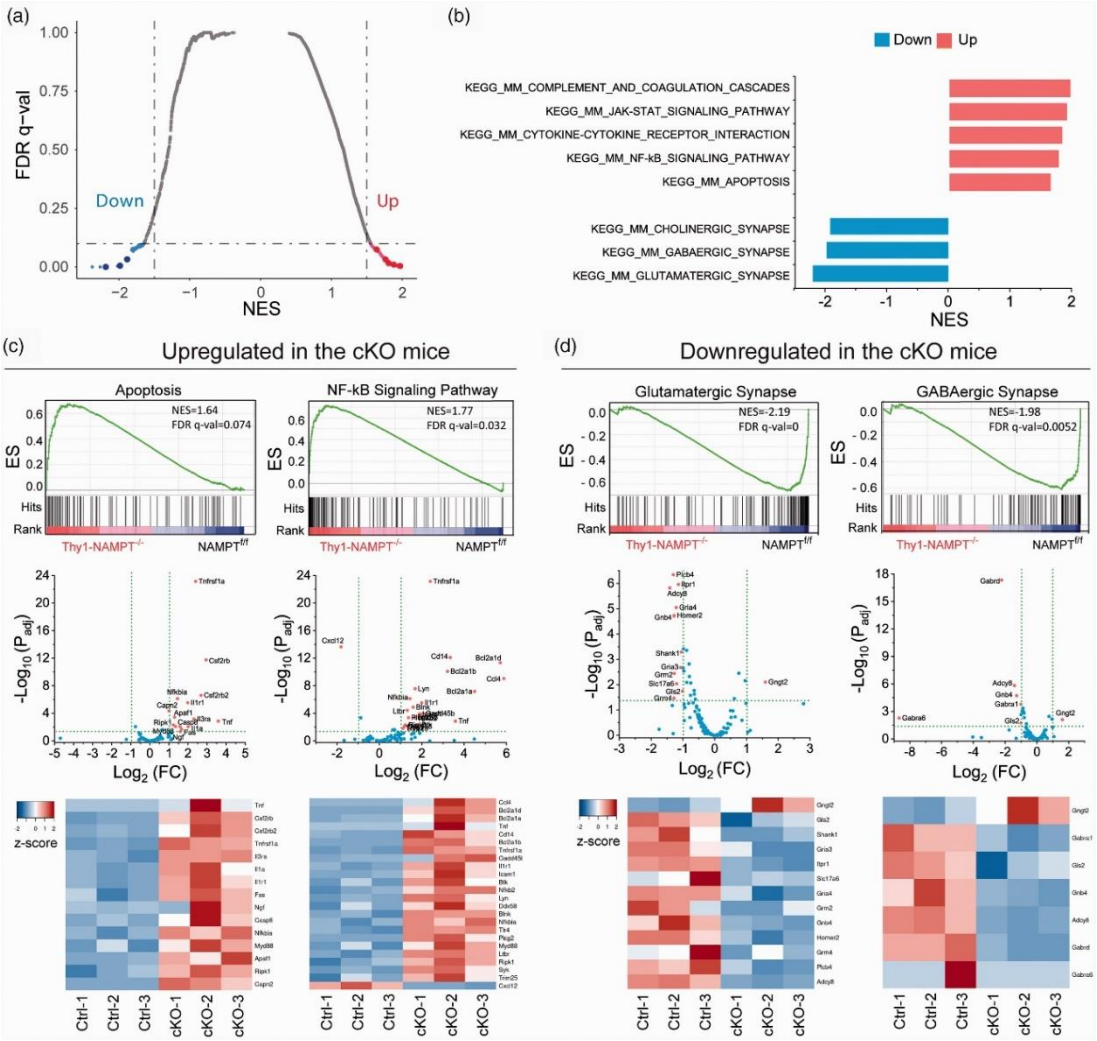

Figure 3.7. GSEA of metabolic pathways. A) Volcano plot of false discovery rate (FDR q-value) versus NES based on GSEA of RNA-seq data from Nampt^{f} Ctrl mice and Nampt$^{-/-}$ cKO mice using 4603 gene sets of GSKB metabolic pathway gene set collection (Lai et al., 2016). Significantly down-enriched gene sets are in blue (sig=True), significantly up-enriched gene sets are in red (sig=True), and nonsignificant gene sets are in grey (sig=False). Black vertical lines highlight NES of -1.5 and 1.5, and black horizontal line represents a FDR q-value of 0.05. **B**) Bar graph of FDR q-val showing representative top up-regulated (red) and down-regulated (blue) gene sets related to immune response, inflammation, cell death, and synaptic function in the cKO mice. Those pathways are visualized as large dots in A. **C-D**) Representative GSEA (up), volcano (middle) and heatmap (low) plots of upregulated (C) and downregulated (D) gene sets in the cKO mice.

Black bars in GSEA indicate the hits in gene sets represented among all genes pre-ranked by ranking metrics. The green dash lines in volcano plots indicate thresholds of $P_{adj}<0.05$ and $|Log_2(FC)|>1$. Heatmap plots only include genes within thresholds.

3.5 Discussion

In our previous study, we demonstrated that neuronal NAMPT is an essential gene for survival using Nampt cKO mice [17]. To further elucidate the mechanism of neurodegeneration and death of the Nampt cKO mice, we conducted metabolomic and transcriptional profiling. Through comprehensive assessment of the effect of NAMPT deletion on metabolism in the motor cortex, we have several novel findings. First, the NAD^+ metabolome and energy production were largely reduced in cKO mice, confirming the predominant role of NAMPT-mediated NAD^+ salvage pathway in NAD^+ biosynthesis. Second, G-5P/F-5P, F-1,6BP and DHAP, the metabolites before the NAD^+-dependent GAPDH in glycolysis, are highly accumulated in cKO mice, indicating that deletion of NAMPT impairs glycolytic metabolism and glycolysis is coupled to NAMPT-mediated NAD^+ production. Third, GSH levels and GSH/GSSG ratio were significantly reduced in cKO mice, suggesting oxidative stress plays a role in neuronal degeneration. Fourth, RNA-seq analysis indicates that genes related to NAD^+ consumption and elimination are more active in cKO mice. Fifth, the glycolytic genes Glut1, Hk2 and Pfkfb3 (upstream from GAPDH), as well as genes involved in oxidative stress, are highly upregulated in cKO mice, corroborating the results from the metabolomic study. Sixth, targeted GSEA shows that neurotransmission pathways (such as synaptic function) were largely down-regulated while immune response, inflammation and cell death pathways (*e.g.*, apoptosis, JAK-STAT, NF-κB signaling, cytokine-cytokine receptor interaction) were largely upregulated in cKO mice, indicating their contribution to neuronal degeneration. These results provide

mechanistic insights into neurodegeneration following NAMPT deletion in the projection neurons.

How does NAMPT deletion cause neuronal degeneration in Nampt cKO mice? Multiple findings indicate energy stress might be the initial cause. First, NAD^+ is dramatically reduced in cKO mice, which causes decrease in ATP production through glycolysis and OXPHOS [9, 10, 17]. The increase in NAD^+ consumption gene expression provides further evidence for the NAD^+ reduction in cKO mice. Second, glycolytic intermediates G-6P/F-6P, F-1,6BP and DHAP were highly accumulated in cKO mice, suggesting the decoupling of glycolysis from NAMPT-mediated NAD^+ salvage pathway and impairment of ATP production in the pathway. Third, adenine and AMP, precursors of ATP, were reduced in cKO mice. Fourth, accumulation of creatine and creatinine suggests the reduction of ATP regeneration. Fifth, AICAR has the highest FC increase in cKO mice. This is important considering AICAR is a downstream intermediate of PRPP and a stimulator of AMPK, the master regulator of energy metabolism and cellular energy stress sensor [32, 33].

Oxidative stress is associated with NAD^+ depletion, a decline in metabolic regulation and reduced cell viability [11, 43, 44]. One key function of the PPP is to maintain cellular redox homeostasis by producing NADPH, the reduced form of $NADP^+$ [31, 45]. $NADP^+$ is synthesized by NAD^+ kinase (NADK) by transferring a phosphate group from ATP to the adenosine ribose moiety of NAD^+ [3] and is involved in maintaining redox balance and supporting the biosynthesis of fatty and nucleic acids. On the other hand, reduced glutathione, GSH, a ubiquitous tripeptide with a free sulfhydryl group made up of

L-cysteine, glycine, and L-glutamate, is the major endogenous antioxidant produced by cells. GSH neutralizes free radicals and reactive oxygen compounds and is required to combat oxidative stress and maintain the normal redox state. GSH is a vital intracellular and extracellular antioxidant and is considered to be one of the most important scavengers of reactive oxygen species (ROS) to reduce oxidative stress [46]. Here, we found that GSH levels and GSH/GSSG ratio were highly reduced in cKO mice. The GSH/GSSG ratio is an important indicator of cellular health, with a higher ratio signifying less oxidative stress in the organism and a lower ratio is indicative of neurodegenerative diseases [3]. GSH is associated with the PPP, where both G6PD and PGD, $NADP^+$-dependent enzymes in the oxidative phase of the PPP, play a key role in producing NADPH and converting GSSG to GSH [47]. Although the mRNA levels of G6PD and PGD are significantly increased in cKO mice, $NADP^+$ was reduced in cKO mice. It is conceivable that the conversion of GSSG to GSH will be limited due to the reduction of $NAPD^+$ levels in cKO mice. Thus, our study indicates that NAMPT deletion could cause enhanced energy and oxidative stress, which subsequently triggers neuronal degeneration.

In light of the reduction of the NAD^+ metabolome in Nampt cKO mice, we then used RNA-seq to analyze a comprehensive set of genes comprising various NAD metabolic pathways including NAD^+ biosynthesis, consumption and transportation. Our data show that mRNA levels of many PARPs (PARP3, 7, 9-10, 12-14) were increased, which could deplete more NAD^+ in neurons and exacerbate energy stress. Similarly, the mRNA level of another NAD^+-consuming enzyme BST 1 (also called CD157) is highly upregulated, which may further contribute to the reduction of NAD^+ levels. We also found key

glycolytic genes Glut1, Hk2 and Pfkfb3, were significantly upregulated in cKO mice. Enhanced expression of glucose transporters and glycolytic enzymes is a common feature of metabolic adaptation to glycolysis [48]. This phenomenon is also consistent with our results that metabolites before GAPDH (G-5P/F-5P, F-1,6BP and DHAP) were highly accumulated in cKO mice, suggesting that the cKO mice attempt to increase glycolytic metabolism to cope with the energy crisis.

Up- and down-regulation of individual genes may only have a small influence on complex traits, whereas the combined effects of genes within a signaling pathway have a greater possibility of impacting complex phenotypes. Assessing the effects of gene expression within the context of entire pathways helps to understand phenotypic significance. Thus, we conducted GSEA, aiming to identify signaling pathways that have the potential to contribute to the pathological phenotype of Nampt cKO mice. These analyses revealed that pathways related to inflammation, immune response and cell death were upregulated while cellular function related pathways were downregulated. Using a curated database of 4603 gene sets, using GSEA we found that JAK-STAT, NF-κB, cytokine-cytokine receptor interaction and apoptosis signaling pathways were activated in cKO mice. The JAK-STAT pathway is activated by many cytokines and regulates cell growth, inflammation, and early embryonic development [49]. NF-κB regulates expression of a large number of genes critical to apoptosis, inflammation, cell survival and various autoimmune diseases. NF-κB induces the expression of various pro-inflammatory genes, including those encoding cytokines and chemokines, and inflammasome regulation, but also regulates cell proliferation and apoptosis [50]. The complement system is a proteolytic

cascade and mediates innate immunity and neuroinflammation [51]. One of the main consequences of complement activation is the recruitment of inflammatory and immunocompetent cells. Upregulation of these pathways in cKO mice is consistent with our observation that cKO mice exhibited enhanced reactive gliosis and motor neuron degeneration [17]. It is also consistent with results in human trials, where oral administration of NR has anti-inflammatory properties in muscle [52]. Since NAMPT is deleted in the projection neurons, this observation also indicates a non-cell autonomous effect of neuronal NAMPT on glial cell activation, a common phenomenon in brain injury and age-related neurodegenerative diseases including Alzheimer's disease. These pathways interact with each other, and activations of them may synergistically contribute to inflammation and cell death. On the other hand, function-related pathways including glutamatergic synapse, GABAergic synapse, cholinergic synapse, ion channel function and ion transportation activity were significantly down-regulated in cKO mice, suggesting neuronal/synaptic functions were impaired, which likely affects their downstream pathways of signal transduction.

There are a few weaknesses in the current study. One is that, for metabolomic and transcriptional profiling, we used cortical tissues where NAMPT was only deleted in neurons. Therefore, the results should reflect an overall response from multiple cell types, not just neurons. This might be particularly true when the brain tissues were collected ~3 weeks after TAM injection when the pathological conditions were fully developed. The other weakness is that due to the nature of *in vivo* experiments with relatively small sample sizes, we analyzed data from mice of both genders. Both animal and human studies indicate

that sex may affect protein expression and metabolism under normal and pathological conditions [53-55]. However, there is no difference in brain weight between WT and cKO mice in our study [17]. Age is another factor that may affect gene expression and metabolism and the NAD^+ metabolome is decreased with age [56-58]. Transcriptomic analysis also suggests impaired microglia response to cerebral ischemia in aged mice compared with young mice [59]. In the current study, since there is a dramatic change in phenotype after NAMPT deletion [17], the effect of NAMPT deletion on metabolism and other pathways should supersede other factors including age and sex, and thus the relative effect of NAMPT deletion is likely the same between male and female, and young and aged mice.

In summary, from our comprehensive study of combined metabolomic and transcriptional profiling, we conclude that the NAD^+ and NAD^+ metabolome reduction, a direct consequence of NAMPT deletion, leads to enhanced energy depletion and oxidative stress, suppresses cellular function, and activates cellular processes related to apoptosis, immune response and inflammation, and eventually causes animal death. These processes are likely time dependent as the NAD^+ contents in the brain tissue are progressively reduced following NAMPT deletion [17]. As NAD^+ decline has been found in aging and many acute and neurodegenerative diseases, our current study provides metabolic and molecular insights into the mechanism of neurodegeneration and potential therapeutic strategies under these pathological conditions.

3.6 References

1. Canto, C., K.J. Menzies, and J. Auwerx, *NAD(+) Metabolism and the Control of Energy Homeostasis: A Balancing Act between Mitochondria and the Nucleus.* Cell Metab, 2015. **22**(1): p. 31-53.
2. Verdin, E., *NAD(+) in aging, metabolism, and neurodegeneration.* Science, 2015. **350**(6265): p. 1208-13.
3. Xiao, W., et al., *NAD(H) and NADP(H) Redox Couples and Cellular Energy Metabolism.* Antioxid Redox Signal, 2018. **28**(3): p. 251-272.
4. Berger, F., et al., *Subcellular compartmentation and differential catalytic properties of the three human nicotinamide mononucleotide adenylyltransferase isoforms.* J Biol Chem, 2005. **280**(43): p. 36334-41.
5. Wang, X., et al., *Subcellular NAMPT-mediated NAD(+) salvage pathways and their roles in bioenergetics and neuronal protection after ischemic injury.* J Neurochem, 2019. **151**(6): p. 732-748.
6. Shackelford, R.E., et al., *Nicotinamide phosphoribosyltransferase in malignancy: a review.* Genes Cancer, 2013. **4**(11-12): p. 447-56.
7. Imai, S. and J. Yoshino, *The importance of NAMPT/NAD/SIRT1 in the systemic regulation of metabolism and ageing.* Diabetes Obes Metab, 2013. **15 Suppl 3**(s3): p. 26-33.
8. Garten, A., et al., *Physiological and pathophysiological roles of NAMPT and NAD metabolism.* Nat Rev Endocrinol, 2015. **11**(9): p. 535-46.
9. Zhang, W., et al., *Neuronal protective role of PBEF in a mouse model of cerebral ischemia.* J Cereb Blood Flow Metab, 2010. **30**(12): p. 1962-71.

10. Bi, J., et al., *Pre-B-cell colony-enhancing factor exerts a neuronal protection through its enzymatic activity and the reduction of mitochondrial dysfunction in in vitro ischemic models.* J Neurochem, 2012. **120**(2): p. 334-46.

11. Wang, X., H. Li, and S. Ding, *Pre-B-cell colony-enhancing factor protects against apoptotic neuronal death and mitochondrial damage in ischemia.* Sci Rep, 2016. **6**: p. 32416.

12. Zhu, Y., et al., *Nmnat restores neuronal integrity by neutralizing mutant Huntingtin aggregate-induced progressive toxicity.* Proc Natl Acad Sci U S A, 2019. **116**(38): p. 19165-19175.

13. Stein, L.R. and S. Imai, *Specific ablation of Nampt in adult neural stem cells recapitulates their functional defects during aging.* EMBO J, 2014. **33**(12): p. 1321-40.

14. Fang, E.F., et al., *NAD(+) in Aging: Molecular Mechanisms and Translational Implications.* Trends Mol Med, 2017. **23**(10): p. 899-916.

15. Zhang, H., et al., *NAD(+) repletion improves mitochondrial and stem cell function and enhances life span in mice.* Science, 2016. **352**(6292): p. 1436-43.

16. Hou, Y., et al., *NAD(+) supplementation normalizes key Alzheimer's features and DNA damage responses in a new AD mouse model with introduced DNA repair deficiency.* Proc Natl Acad Sci U S A, 2018. **115**(8): p. E1876-E1885.

17. Wang, X., et al., *Deletion of Nampt in Projection Neurons of Adult Mice Leads to Motor Dysfunction, Neurodegeneration, and Death.* Cell Rep, 2017. **20**(9): p. 2184-2200.

18. Frederick, D.W., et al., *Loss of NAD Homeostasis Leads to Progressive and Reversible Degeneration of Skeletal Muscle.* Cell Metab, 2016. **24**(2): p. 269-82.

19. Stein, L.R., et al., *Expression of Nampt in hippocampal and cortical excitatory neurons is critical for cognitive function.* J Neurosci, 2014. **34**(17): p. 5800-15.

20. Stromsdorfer, K.L., et al., *NAMPT-Mediated NAD(+) Biosynthesis in Adipocytes Regulates Adipose Tissue Function and Multi-organ Insulin Sensitivity in Mice.* Cell Rep, 2016. **16**(7): p. 1851-60.

21. Lin, J.B., et al., *NAMPT-Mediated NAD(+) Biosynthesis Is Essential for Vision In Mice.* Cell Rep, 2016. **17**(1): p. 69-85.

22. Rongvaux, A., et al., *Nicotinamide phosphoribosyl transferase/pre-B cell colony-enhancing factor/visfatin is required for lymphocyte development and cellular resistance to genotoxic stress.* J Immunol, 2008. **181**(7): p. 4685-95.

23. Lundt, S., et al., *The effect of NAMPT deletion in projection neurons on the function and structure of neuromuscular junction (NMJ) in mice.* Sci Rep, 2020. **10**(1): p. 99.

24. Percie du Sert, N., et al., *The ARRIVE guidelines 2.0: Updated guidelines for reporting animal research.* PLoS Biol, 2020. **18**(7): p. e3000410.

25. Young, P., et al., *Single-neuron labeling with inducible Cre-mediated knockout in transgenic mice.* Nat Neurosci, 2008. **11**(6): p. 721-8.

26. Xiong, N., et al., *Using arterial-venous analysis to characterize cancer metabolic consumption in patients.* Nat Commun, 2020. **11**(1): p. 3169.

27. Malavasi, F., et al., *Evolution and function of the ADP ribosyl cyclase/CD38 gene family in physiology and pathology.* Physiol Rev, 2008. **88**(3): p. 841-86.

28. Ortolan, E., et al., *CD157: From immunoregulatory protein to potential therapeutic target.* Immunol Lett, 2019. **205**: p. 59-64.

29. Davis, W.L., et al., *Glyoxylate cycle in the epiphyseal growth plate: isocitrate lyase and malate synthase identified in mammalian cartilage.* Anat Rec, 1989. **223**(4): p. 357-62.

30. Jong, C.J. and S. Schaffer, *Mechanism underlying the antioxidant activity of taurine.* The FASEB Journal, 2013. **27**(S1): p. 1086.1-1086.1.

31. Hwang, S., et al., *Correcting glucose-6-phosphate dehydrogenase deficiency with a small-molecule activator.* Nat Commun, 2018. **9**(1): p. 4045.

32. Giri, S., et al., *5-aminoimidazole-4-carboxamide-1-beta-4-ribofuranoside inhibits proinflammatory response in glial cells: a possible role of AMP-activated protein kinase.* J Neurosci, 2004. **24**(2): p. 479-87.

33. Kirchner, J., B. Brune, and D. Namgaladze, *AICAR inhibits NFkappaB DNA binding independently of AMPK to attenuate LPS-triggered inflammatory responses in human macrophages.* Sci Rep, 2018. **8**(1): p. 7801.

34. Schlattner, U., M. Tokarska-Schlattner, and T. Wallimann, *Mitochondrial creatine kinase in human health and disease.* Biochim Biophys Acta, 2006. **1762**(2): p. 164-80.

35. Wang, Z., M. Gerstein, and M. Snyder, *RNA-Seq: a revolutionary tool for transcriptomics.* Nat Rev Genet, 2009. **10**(1): p. 57-63.

36. Mortazavi, A., et al., *Mapping and quantifying mammalian transcriptomes by RNA-Seq.* Nat Methods, 2008. **5**(7): p. 621-8.

37. Heer, C.D., et al., *Coronavirus infection and PARP expression dysregulate the NAD metabolome: An actionable component of innate immunity.* J Biol Chem, 2020. **295**(52): p. 17986-17996.

38. Li, Y.P., W. Chen, and P. Stashenko, *Molecular cloning and characterization of a putative novel human osteoclast-specific 116-kDa vacuolar proton pump subunit.* Biochem Biophys Res Commun, 1996. **218**(3): p. 813-21.

39. Jupe, S., et al., *Reactome - a curated knowledgebase of biological pathways: megakaryocytes and platelets.* J Thromb Haemost, 2012. **10**(11): p. 2399-402.

40. Ma, H., et al., *The Edinburgh human metabolic network reconstruction and its functional analysis.* Mol Syst Biol, 2007. **3**(1): p. 135.

41. Evsikov, A.V., et al., *MouseCyc: a curated biochemical pathways database for the laboratory mouse.* Genome Biol, 2009. **10**(8): p. R84.

42. Lai, L., et al., *GSKB: A gene set database for pathway analysis in mouse.* bioRxiv, 2016: p. 082511.

43. Braidy, N., et al., *Mapping NAD(+) metabolism in the brain of ageing Wistar rats: potential targets for influencing brain senescence.* Biogerontology, 2014. **15**(2): p. 177-98.

44. Wang, X., H. Li, and S. Ding, *The effects of NAD+ on apoptotic neuronal death and mitochondrial biogenesis and function after glutamate excitotoxicity.* Int J Mol Sci, 2014. **15**(11): p. 20449-68.

45. Kuehne, A., et al., *Acute Activation of Oxidative Pentose Phosphate Pathway as First-Line Response to Oxidative Stress in Human Skin Cells.* Mol Cell, 2015. **59**(3): p. 359-71.

46. Goncalves, C.A., et al., *Glycolysis-Derived Compounds From Astrocytes That Modulate Synaptic Communication.* Front Neurosci, 2018. **12**: p. 1035.

47. Li, H., et al., *6-Phosphogluconate Dehydrogenase Links Cytosolic Carbohydrate Metabolism to Protein Secretion via Modulation of Glutathione Levels.* Cell Chem Biol, 2019. **26**(9): p. 1306-1314 e5.

48. Hoxhaj, G. and B.D. Manning, *The PI3K-AKT network at the interface of oncogenic signalling and cancer metabolism.* Nat Rev Cancer, 2020. **20**(2): p. 74-88.

49. Aaronson, D.S. and C.M. Horvath, *A road map for those who don't know JAK-STAT.* Science, 2002. **296**(5573): p. 1653-1655.

50. Liu, T., et al., *NF-kappaB signaling in inflammation.* Signal Transduct Target Ther, 2017. **2**(1): p. 17023.

51. Carpanini, S.M., M. Torvell, and B.P. Morgan, *Therapeutic Inhibition of the Complement System in Diseases of the Central Nervous System.* Front Immunol, 2019. **10**: p. 362.

52. Elhassan, Y.S., et al., *Nicotinamide Riboside Augments the Aged Human Skeletal Muscle NAD(+) Metabolome and Induces Transcriptomic and Anti-inflammatory Signatures.* Cell Rep, 2019. **28**(7): p. 1717-1728 e6.

53. Cikic, S., et al., *Sexual differences in mitochondrial and related proteins in rat cerebral microvessels: A proteomic approach.* J Cereb Blood Flow Metab, 2021. **41**(2): p. 397-412.

54. Vandekar, S.N., et al., *Sex differences in estimated brain metabolism in relation to body growth through adolescence.* J Cereb Blood Flow Metab, 2019. **39**(3): p. 524-535.

55. Cirillo, C., et al., *Post-stroke remodeling processes in animal models and humans.* J Cereb Blood Flow Metab, 2020. **40**(1): p. 3-22.

56. Yaku, K., K. Okabe, and T. Nakagawa, *Simultaneous measurement of NAD metabolome in aged mice tissue using liquid chromatography tandem-mass spectrometry.* Biomed Chromatogr, 2018. **32**(6): p. e4205.

57. Gomes, A.P., et al., *Declining NAD(+) induces a pseudohypoxic state disrupting nuclear-mitochondrial communication during aging.* Cell, 2013. **155**(7): p. 1624-38.

58. Clement, J., et al., *The Plasma NAD(+) Metabolome Is Dysregulated in "Normal" Aging.* Rejuvenation Res, 2019. **22**(2): p. 121-130.

59. Shi, L., et al., *Genome-wide transcriptomic analysis of microglia reveals impaired responses in aged mice after cerebral ischemia.* J Cereb Blood Flow Metab, 2020. **40**(1_suppl): p. S49-S66.

Chapter 4: Dietary NMN supplementation enhances motor and NMJ function in ALS

4.1 Abstract

Amyotrophic lateral sclerosis (ALS) is an adult-onset neurodegenerative disease that causes the degeneration of motor neurons in the motor cortex and spinal cord. Patients with ALS experience muscle weakness and atrophy in the limbs which eventually leads to paralysis and death. NAD^+ is critical for energy metabolism, such as glycolysis and oxidative phosphorylation, but is also involved in non-metabolic cellular reactions. In the current study, we determined whether the supplementation of nicotinamide mononucleotide (NMN), an NAD^+ precursor, in the diet had beneficial impacts on disease progression using a $SOD1^{G93A}$ mouse model of ALS. We found that the ALS mice fed with an NMN-supplemented diet (ALS^{+NMN} mice) had modestly extended lifespan and exhibited delayed motor dysfunction. Using electrophysiology, we studied the effect of NMN on synaptic transmission at neuromuscular junctions (NMJs) in symptomatic of ALS mice (18 weeks old). ALS^{+NMN} mice had larger end-plate potential (EPP) amplitudes and maintained better responses than ALS mice, and also had restored EPP facilitation. While quantal content was not affected by NMN, miniature EPP (mEPP) amplitude and frequency were elevated in ALS^{+NMN} mice. NMN supplementation in diet also improved NMJ morphology, innervation, mitochondrial structure, and reduced reactive astrogliosis in the ventral horn of the lumbar spinal cord. Overall, our results indicate that dietary consumption of NMN can slow motor impairment, enhance NMJ function and extend lifespan of ALS mice.

4.2 Introduction

In Chapters two and three we demonstrated that neuronal NAMPT deficiency produces dysfunctional NMJs and impairs cellular bioenergetics, most notably the NAD metabolome. Additionally, we previously observed that deleting NAMPT from projection neurons produces an ALS-like phenotype. This lead us to investigate whether NAD^+ homeostasis may be disrupted in ALS and if NAD^+ precursor supplementation may improve the NMJ function declines that occur during ALS.

ALS is an adult-onset fatal neurodegenerative disease characterized by the death of upper and lower motor neurons (MNs). ALS patients initially experience muscle weakness and atrophy in the limbs which progresses into paralysis and typically survive 2-5 years after symptoms appear [1]. Numerous genes have been linked to ALS, including *SOD1*, *TARDBP*, and *C9ORF72* [2]. Currently the only approved treatments for ALS have displayed limited efficacy [3-5]. As such, research into effective interventions that slow the progression of ALS is greatly needed. Common ALS symptoms include body weight loss, locomotor deficits, muscle weakness and atrophy, and paralysis. Symptoms arise from deficits in function of the central (spinal cord/brain) and peripheral (neuromuscular junctions, NMJ) nervous system. During ALS, NMJs undergo extensive structural and functional changes that contribute to muscle dysfunction and motor impairments and MN death, exhibiting denervation, broken motor endplates, mitochondrial dysfunction, and altered neurotransmission [6], making investigation of NMJs critical to understanding ALS development and progression.

Nicotinamide adenine dinucleotide (NAD^+) is an abundant metabolite in mammalian cells and is involved in hundreds of cellular reactions and pathways, including

DNA repair, oxidative stress, and energy metabolism [7]. NAD^+ is synthesized using one of three different pathways: the *de novo*, Preiss-Handler, and NAD^+ salvage pathways. In mammalian cells, the majority of NAD^+ is generated using the salvage pathway, where nicotinamide (NAM) is converted into nicotinamide mononucleotide (NMN), by the rate-limiting enzyme nicotinamide phosphoribosyltransferase (NAMPT), and NMN is subsequently converted into NAD^+ by nicotinamide mononucleotide acetyltransferases (NMNAT1-3) [8-10]. Nicotinamide riboside (NR) can also be converted to NMN and bypass the rate-limiting step in the salvage pathway. Altered NAD^+ homeostasis has been linked to aging and age-related neurodegenerative diseases, including Alzheimer's disease, Parkinson's disease, and ALS [11-13]. Many studies indicate that administering NAD^+ precursor metabolites, typically NAM, NMN, or NR, can increase NAD^+ levels and correct certain declines [14-19].

Abnormal and defective bioenergetic homeostasis has been observed in ALS and NAD is critical for maintaining bioenergetic homeostasis [20, 21]. There is also growing evidence showing that NAD homeostasis is impaired in ALS, with the salvage pathway specifically affected. Metabolomic profiling of the ALS mouse motor cortex revealed alterations to the NAD^+/NADH ratio and NAM levels, additionally, NAD^+ contents are decreased in the brain and spinal cords of ALS mice [22-24]. Disrupted NAM metabolism has also been observed in both ALS mice and human patients. NAM levels are reduced in ALS patient blood serum and cerebrospinal fluid. ALS mice administered NAM subcutaneously exhibited better motor performance than ALS mice not provided with NAM [25]. In the salvage pathway, expression of NAMPT and NMNAT2, the NMNAT isoform predominant in neurons, are altered in human ALS spinal cords [14, 23, 26].

In our previous studies we demonstrated that deleting NAMPT from projection neurons caused locomotor deficits, neurodegeneration, and NMJ dysfunction, a phenotype reminiscent of ALS mice; however, administering NMN can enhance motor behavior, NMJ structure and function, and survival of these NAMPT deficient mice [14, 17]. P7C3, a potential NAMPT activator, increased MN survival and improved walking gait in ALS mice [27]. NMN and NR can elevate NAD^+ levels, improve motor activity, increase lifespan and counteract the toxicity of $SOD1^{G93A}$ ALS astrocytes on MNs [22, 26, 28]. NMN treatment increased axonal and neurite outgrowth and improved mitochondrial structure in corticospinal MNs from ALS mice [24]. However, *in vivo* investigation of NMN supplementation on NMJ function in ALS has not been reported. Here, using the $SOD1^{G93A}$ ALS mouse model, we observed NAD^+ decline at the pre-symptomatic stage, and studied whether the dietary supplementation of NMN had beneficial effects on ALS. Overall, our study indicates that dietary NMN can enhance motor and NMJ function, delay the progression of ALS and may provide a therapeutic strategy for ALS.

4.3 Materials and Methods

4.3.1 Mice and NMN-supplemented diet

Mice were maintained on a 12 h light:12 h dark cycle (lights on 7 am-7 pm) in our AAALAC-accredited animal facility at the University of Missouri. All experimental procedures were performed in accordance with the NIH Guide for the Care and Use of Laboratory Animals and experiments were approved by the University of Missouri Animal Care Quality Assurance Committee. Adult male and female wild-type C57BL/6J (WT) and hemizygous transgenic $SOD1^{G93A}$ ALS mice (Strain 002726 B6SJL-Tg(SOD1*G93A), Jackson Lab, ME) were used for this study. At 8 weeks old, ALS mice were assigned to a control diet (i.e., standard mouse chow pellets) or an NMN-supplemented diet (hereafter, ALS and ALS^{+NMN} mice). The NMN-supplemented diet contained 2.7 g NMN/kg mouse chow. *Ad libitum* feeding from this diet translates into 400 mg/kg/day in adult mice. NMN was obtained from dietary NMN supplement tablets (Gene Formulas, Davie, FL) and stored at 4 ^{o}C. Pellets of the NMN-supplemented diet consisted of standard mouse chow, NMN powder, xanthan gum (Bob's Red Mill, Milwaukie, OR), and water. Standard mouse chow pellets were ground into a fine powder. Chow powder, NMN powder, xanthan gum, and water were mixed until well combined. Individual pellets were made using a granule machine and placed in dark room until completely dry. Pellets were made weekly, kept in an air-tight bag and stored at 4 ^{o}C until needed. For survival curve, a mouse was considered to have reached end-stage when it was unable to right itself within 20 s after being placed on its side [29].

4.3.2 NAD assay

Red blood cell, plasma, and cortical NAD^+ and NADH concentrations from 6-week-old (pre-symptomatic), 11-12 week-old (symptom on-set) and 19-20 week-old (end-stage) ALS and age-matched WT mice were assessed using commercially available kits (Cat. No. E2ND-100, Bioassay systems, Hayward, CA) as we previously reported [14].

4.3.3 Behavioral assessment

Behavior testing was performed between 8:30 am-12:30 pm. All the animals were taken out from the animal facility in their home cages to the behavior test room and habituated for at least 30 min starting at 8:00 am. Mice were given an interval of at least 30 min for recovery in their home cages between different behavior tests. All instruments were sanitized between tests to avoid olfactory effects. Behavior testing began at 7 weeks of age for all mice, considered to be the pre-symptomatic period for $SOD1^{G93A}$ mice [30, 31] and occurred weekly during the testing period.

4.3.4 Rotarod test

Accelerated rotarod is a commonly used test to assess motor performance in rodents [32]. An ENV-557M accelerating rotarod (Med Associates, VT) was used for testing. Mice were pre-trained to learn to walk on the accelerating rod prior to testing. Mice were placed on the rod and allowed to move freely. 4 to 40 rpm acceleration setting was used. The time when the mouse fell off the rod was recorded, with a maximum time of 180 s. If a mouse dropped before 180 s, a second trial was given with at least 10 min between trials.

4.3.5 Hanging wire test

The hanging wire test is used to assess upper limb strength [33]. Mice were pre-trained prior to testing. Mice utilized forelimbs to hang their body weight on a wire stretched between two posts separated by 50 cm. The wire was 60 cm high, with padding

placed underneath to cushion mice should they drop. The time until the mouse dropped from the wire was recorded. A time of zero was assigned if the mouse dropped off immediately with a maximum time of 120 s. Two trials were performed for each mouse at each test period, with at least 10 min between trials.

4.3.6 Four limb grip force

Four limb grip force testing is used to measure peak muscle force [34]. Grip strength was measured by a M4-2 digital force gauge (Mark-10 Corporation, Copiague, NY) attached with a rectangular grid. The apparatus was used to measure the combined strength of the forelimbs and hindlimbs. The mouse was held near the base of the tail and gently lowered to allow the forelimbs and hindlimbs to grab the grid. The mouse was gently pulled back by the tail and the mouse's body stayed parallel to the grid. Peak force was recorded from the reading when the mouse released the grid. Mice were tested over five trials with at least 30 s between trials. The largest three values of the five were chosen, and the average value of them was used for analysis.

4.3.7 Open field test

The open field test is used to assess voluntary movement [35]. After at least 30 min habituation in the testing area, the mouse was placed in the center of the open field recording chamber, which consists of a clear, open Plexiglass box (46.6 cm×38.5 cm×25.6 cm) with an overhead camera to record movements of mice for 10 min. The total distance travelled, total time immobile, mean speed, and maximum speed during the 10 min testing period were analyzed by ANY- maze software (Stoelting, IL). The sensitivity for the detection of immobile was set as 65% of the body area. If the mouse remained motionless for 5 s it was considered immobile.

4.3.8 Walking gait analysis

Walking gait was assessed using a modified version of a previously established protocol [36]. Briefly, the forepaws and hindpaws of the mice were painted with two contrasting colors (orange and purple, respectively), using a non-toxic water-based paint. The mice were then gently placed on one end of textured watercolor paper strip that was approximately 43 cm long and 12 cm wide. The sides of the paper were bordered with blocks to ensure the mice walked in a straight line. The strip led into a darkened enclosure to encourage the mice to walk down the paper. The paws of the mice were then cleaned to remove any remaining paint. Parameters measured, for both forelimbs and hindlimbs, were stride length (the center of the paw pad to the center of the following paw pad) and stride width (the distance between the left and right forelimbs or hindlimbs. For both forelimbs and hindlimbs, the initial stride on the paper and the initial stride after the mouse had stopped, was not recorded.

4.3.9 End-Plate Potential (EPP) recording

Electrophysiological recordings of isolated semitendinosus muscles were conducted using methods previously described [14, 37]. The recording chamber, covered with Sylgard, was perfused with regular Tyrode's solution (140 mM NaCl, 5.6 mM KCl,1 mM $MgCl_2$, 2 mM $CaCl_2$, 1.8 mM Na_2HPO_4, 10 mM $NaHCO_3$, 5.5 mM glucose) and continuously received 95% O_2/5% CO_2. The isolated muscle-nerve preparation was carefully extended and pinned flat on the bottom of the recording chamber. Nerves were sucked into a tight polyethylene electrode and stimulated with a Grass S44 stimulator (pulse duration of 0.5 ms, Grass Medical Instruments, Quincy, MA) through a PSIU6 photoelectric stimulus isolation unit (Grass Instrument Co, Quincy, MA) (Fig. 4.1, graphic designed with

BioRender). The minimum voltage and current threshold to induce muscle contraction was used for recording. Muscles lacking contractility were discarded. A muscle specific voltage-gated Na^+ channel blocker μ-conotoxin GIIIB (1 μM, Alomone Labs, Jerusalem, Israel) was added to the chamber to prevent muscle contractions during recording. Sharp glass electrodes (40-60 MΩ) filled with 3 mM KCl solution were inserted into individual muscle fibers near motor endplates. EPPs were then recorded with a BA-1S bridge amplifier (NPI Electronic, Tamm, Germany) during stimulations and acquired with a Digidata 1440A digitizer (Molecular Devices, San Jose, CA) using Axoscope 11.2 software (Molecular Devices, San Jose, CA).

Evoked EPPs were recorded during the voltage pulse stimulations of 10, 20, 50, 100, and 200 Hz. The stimulation period for each frequency lasted approximately 2 s, with at least 5 s between stimulation periods. Paired-pulse facilitation, starting with 100 ms interval between pulses, was recorded following the frequency stimulation. Each interval was repeated 3 times, with at least 3 s between recordings. At the conclusion of both the frequency stimulation and the paired-pulse stimulation, the recording was continued without stimulation to acquire miniature EPPs (mEPPs) for assessing spontaneous vesicle release and quantal content.

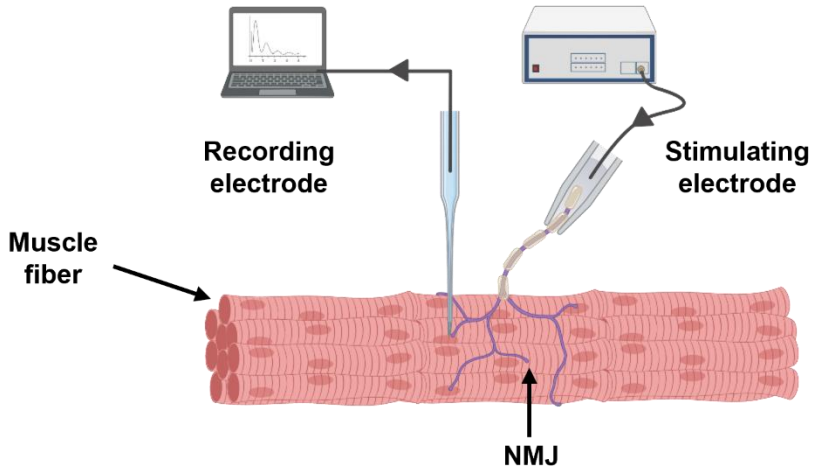

Figure 4.1. Semitendinosus EPP recording diagram.

Data was analyzed using Clampfit 11.2 (Molecular Devices, San Jose, CA). Only the first second of stimulation period for each frequency was used for analysis. The amplitude (resting baseline to peak of response) of the first five and last five responses of the first second of stimulation were recorded. These responses were averaged together to determine the mean EPP amplitude at the start (first five responses) and end (last five responses) of one second of stimulation. The EPP amplitude ratio was determined as the ratio of the mean EPP amplitudes of the last five responses to the first five responses. To study paired-pulse facilitation, the EPPs of the first and second responses with different pulse intervals were recorded and the ratio of the second response amplitude to the first response amplitude was calculated. At least three facilitation ratios were calculated for each pulse interval and were averaged together to determine the mean facilitation at each pulse interval.

To measure spontaneous vesicle release, mEPPs were recorded. At least 3 different end-plate recordings were used to assess mEPP amplitude, with at least 200 mEPPs for each recording. The responses were fitted with a Gaussian distribution, with peak of the

best-fit line used as the mean amplitude. Each end-plate recording had a unique mEPP amplitude with individual amplitudes averaged together to determine mean mEPP for each condition. To determine mEPP frequency, the number of mEPPs that occurred in a 10-15 s period following the final frequency or paired-pulse stimulation event were counted. The 10-15 s period began at least 5 s after the final stimulation event. Quantal content was calculated by dividing the mean EPP amplitude at 10 Hz by the mean mEPP amplitude of each individual end-plate recording.

4.3.10 Neuromuscular junction (NMJ) Immunostaining

To analyze the structure of NMJs, fresh semitendinosus muscles were isolated from 18-week-old WT, ALS, and ALS^{+NMN} mice following cervical dislocation. Muscles were incubated with α-bungarotoxin (α-BTX) conjugated with Alex Flour-555 (1:1000, B34451, Invitrogen) for 25-30 min, and then washed 3 times for 10 min with 1X PBS. Muscles were then fixed with 4% paraformaldehyde (PFA) overnight at 4 ^{o}C and washed 3 times for 20 min with 1X PBS. Fixed muscles were pinned to the bottom of a Sylgard dish and incubated with rabbit-neurofilament-200 (1:300, N4142, Millipore Sigma) on shaker at 4 ^{o}C for 1 week. Muscles were washed with 1X PBS for at least 4 days on shaker at 4 ^{o}C, with PBS replaced each day. Muscles were then incubated with donkey anti-rabbit AlexaFluor-488 (1:400, A21206, Invitrogen) on shaker at 4 ^{o}C for 1 week followed by washing with 1X PBS for at least 4 days on shaker at 4 ^{o}C, with PBS replaced each day. Muscles were embedded in OCT compound and stored at -20 ^{o}C prior to cutting. Using a cryostat (Leica CM1900), 30 μm longitudinal sections of muscle were cut and placed onto coated glass microscope slides. Slides were allowed to dry, carefully washed with 1X PBS to remove excess OCT around muscle slices and sealed with glass coverslips using Permount.

4.3.11 Brain and spinal cord Immunostaining

18-week-old WT, ALS, and ALS^{+NMN} mice were anesthetized with urethane (200 mg/ml) and perfused with cold 1X PBS. The brains and spinal cords were quickly dissected, placed in 4% PFA, and stored at 4 ^{o}C for 4 days. After 2 days, the lumbar portion of the spinal cord was dissected out and returned to 4% PFA and stored at 4 ^{o}C for another 2 days. Brains and spinal cords were then transferred to 30% sucrose solution for 7 days. Tissues were embedded in ice and sectioned using a cryostat (Leica CM1900). 30 μm coronal (brain) and transverse (lumbar) sections were cut. Slices were then covered with a cryoprotective solution and stored at -20 ^{o}C until needed.

For immunolabelling, slices were washed 3 times for 10 min to remove cryoprotective solution. Slices were then blocked for 1 h (10% Donkey serum and 0.3% Triton-X in 1X PBS) and washed again 3 times for 10 min. Slices were incubated with goat-choline acetyltransferase (ChAT, 1:300, AB144P, Abcam), rabbit-NeuN (1:300, #12943, Cell Signaling), rabbit-GFAP (1:300, G9269), or rabbit-Iba1 (1:300, 019-19741, FUJIFILM) at 4 ^{o}C on shaker for overnight. Slices were then washed 3 times for 10 min and incubated with donkey anti-rabbit Alexa Fluor-488 (1:400, A21206, Invitrogen) or donkey anti-goat Alexa Fluor-568 (1:400, A11051, Invitrogen) at room temperature on shaker for 4 h. Slices were then washed 3 times for 10 min. Slices were then carefully transferred to glass microscope slides and covered with DAPI (P36931, Invitrogen) or Permount mounting media.

4.3.12 Transmission electron microscopy (TEM)

18-week-old WT, ALS, and ALS^{+NMN} mice were anesthetized with urethane (200 mg/ml) and perfused with cold 1X PBS. The spinal cord and semitendinosus muscles were

quickly dissected out. Immediately, muscles were cleaned of excessive non-semitendinosus muscle, connective tissue, and fat. The proximal and distal end of the muscle were discarded with only the central portion of the muscle, which contains the NMJs, was retained. The muscle was then cut into small pieces and fixed in 100 mM sodium cacodylate buffer containing 2% PFA and 2% glutaraldehyde (pH 7.35). Samples were left at room temperature for at least one hour and moved to 4 °C for at least 23 h. Spinal cords were placed in 4% PFA and stored at 4 °C for 4 days. The vertebrae were carefully removed, and L1/2 of lumbar spinal cord was dissected out. The dorsal portion was discarded, and the ventral horns were carefully cut into smaller sections and placed in 100 mM sodium cacodylate buffer containing 2% PFA and 2% glutaraldehyde (pH 7.35). Samples were left at room temperature for at least one hour and moved to 4 °C for at least 23 h.

Fixed samples were washed with 100 mM sodium cacodylate buffer (pH 7.35) containing 130 mM sucrose. Secondary fixation was performed using 1% osmium tetroxide in a cacodylate buffer using a Pelco Biowave (Ted Pella, Inc. Redding, California) operated at 100 Watts for 1 min. Samples were incubated at 4 °C for 1 h, then rinsed with cacodylate buffer, followed with distilled water. En bloc staining was performed using 1% aqueous uranyl acetate and incubated at 4 °C overnight, then rinsed with distilled water. A graded dehydration series (30%, 50%, 70%, 90%, 100%, 100%) was performed using ethanol at 4 °C, transitioned to acetone. Dehydrated samples were then infiltrated with Epon resin for 24 h at room temperature and polymerized at 60 °C for 48-72 h. Samples were cut into 85 nm thick longitudinal (semitendinosus) or transverse (spinal cord) sections

using an ultramicrotome (Ultracut UCT, Leica Microsystems, Germany) and a diamond knife (Diatome, Hatfield, PA).

4.3.13 Imaging and analysis

Fluorescent images were taken using a Nikon Eclipse FN1 fluorescent microscope with a 10x, 20x or 40x water immersion Olympus objectives (LUMPlanFI/IR, 40x/0.8) and were acquired using a Photometric Cool SNAP EZ CCD camera controlled by Metaview software. Fluorescent intensity, area, length, breadth, and shape factor measurements were performed by Metamorph software using the integrated morphometry analysis function. Metamorph or ImageJ (NIH) were used for cell counting. At least 100 NMJ images were acquired for each mouse and neurofilament-200 staining was used to assess innervation. Only the gray matter of each ventral horn was used for analysis of L2-6 lumbar spinal cord staining. Only the CA1 region of the hippocampus was used for analysis. Representative images in figures were acquired using a Leica DMI4000B (Mannheim, Germany) confocal microscope using Leica 20x (HC PL APO, 20x/0.60) and 63x oil immersion (HD PL APO, 63x/1.40) lens. For TEM, 2000X, 2500X, and 5000X images were acquired with a JEOL JEM 1400 transmission electron microscope (JEOL, Peabody, MA) at 80 kV (0.35 s exposure time) on a Gatan Ultrascan 1000 CCD (Gatan, Inc, Pleasanton, CA). Mitochondrial area, perimeter, circularity, and Feret's diameter were assessed using ImageJ. Circularity is scored from 0 to 1, with a score of 1 reflecting a perfect circle and the score decreasing as the shape becomes elongated. Feret's diameter is the longest distance between any two points along the outlined area and can be referred to as caliper diameter [38].

4.3.14 Western blotting analysis

The procedure was described as in our previous studies [39-41]. Briefly, cortical tissues were collected from end-stage ALS and age-matched WT mice and were homogenized in lysis buffer mixed with a protease inhibitor (Pierce Biotechnology, Rockford, IL) and phosphatase inhibitor cocktails (Sigma). The homogenized tissue was centrifuged at 13,500 g at 4 °C for 20 min and supernatant was retained. BCA assay kit (Thermo Scientific) was used to measure protein concentration. Equivalent amounts of protein from each sample were diluted with lysis buffer and boiled for 5 min. Samples were then subjected to electrophoresis in 10% SDS-polyacrylamide gels at 100 mV for 110-120 min. Gels were then transferred to polyvinylidene fluoride membranes using mixed molecular weight function of Trans-Blot Turbo Transfer System (Bio-Rad). Membranes were blocked for 1 h in 5% BSA in Tris-buffered saline containing (0.1%) Tween-20 (TBST). Membranes were then incubated overnight at 4 °C with primary antibodies Ms-NAMPT (1:2500, ALX-804-922-C100, Enzo Life Sciences), Ms-NMNAT1 (1:1000,sc-271557, Santa Cruz), Ms-NMNAT2 (1:1000, sc-515206, Santa Cruz), Gt-NMNAT3 (1:1000, ab121030, Abcam), Ms-PSD95 (1:1000, sc-32290, Santa Cruz), Ms-Synaptophysin (1:2500, s5768, Sigma), Rab-NMDAR2A (1:1000, NB300-105, Novus), Rab-NMDAR2B (1:1000, NB300-106, Novus), Ms-GluR1 (1:1000, NBP2-22399, Novus), Rab-GluR2 (1:1000, NBP2-75510), Ms-VGlut1 (1:1000, NBP2-59329, Novus), or Ms-β-actin (1:5000, sc-47778, Santa Cruz). Membranes were exposed to Clarity™ Western ECL Substrate (Bio-Rad) and imaged with ChemiDoc™ XRS+ system (BioRad). Precision Plus Protein™ Dual Color Standards (Bio-Rad) was used as the marker to evaluate the molecular size of protein bands.

4.3.15 Statistical analysis

Data were expressed as mean ± standard error of the mean (SEM). Comparisons were made using One-way ANOVA or unpaired Student's t-test. Survival data was analyzed using Kaplan-Meier survival curve followed by Log-Rank test. Levels of statistical significance were set as *$p<0.05$, **$p<0.01$, and ***$p<0.001$. Statistical analyses were performed using OriginPro 2022 and Excel.

4.4 Results

4.4.1 ALS causes reduction of NAD levels at pre-symptomatic stage

We first determined whether NAD homeostasis was altered in $SOD1^{G93A}$ ALS mice. NAD^+ and NADH levels in the blood (both plasma and red blood cells) were already reduced in pre-symptomatic (6-week-old) ALS mice and the deficit of NAD^+ and NADH became larger at the symptom onset stage (11-12 weeks old) and end-stage (19-20 weeks old), suggesting a disease-stage dependent decline in NAD levels (Fig. 4.2A-B). Similarly, NAD^+ and NADH levels were also reduced in the cortex of end-stage ALS mice (Fig. 4.2C). These results demonstrate that ALS mice have impaired NAD homeostasis in both circulation and tissues; nevertheless, the NAD^+/NADH ratios in blood and brain tissue remained unchanged in ALS mice as compared with WT mice, suggesting ALS does not affect redox state. Despite the decline of NAD^+ levels, there was no difference in expression of NAD^+ salvage pathway proteins in ALS mice, though NAMPT levels appeared to be slightly reduced (Fig. 4.2D-E). The NAD^+ level can be also affected by its synthesis of other pathways and consumption; thus, the mechanism of NAD reduction remains to be further studied. Widespread synapse loss occurs in the brain and spinal cord during ALS, with glutamate transport and signaling potentially being a driving factor [42-44]. Supporting this, PSD95 expression was decreased in the cortex at the end-stage of ALS mice (Fig. 4.3A-B).

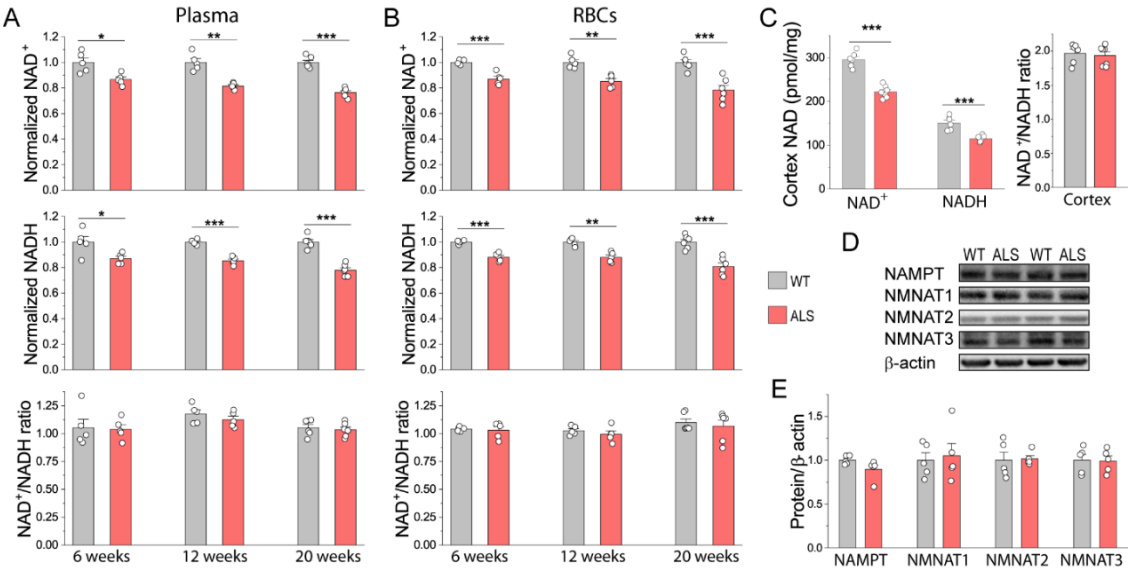

Figure 4.2. SOD1^{G93A} ALS mice have reduced NAD$^+$ levels in the blood and brain. A-B) Normalized plasma and red blood cell NAD$^+$ and NADH levels and NAD$^+$/NADH ratio in 6 week (pre-symptomatic), 11-12 week (symptom on-set) and 19-20 week (end-stage) old ALS mice (N=5-6) and age-matched WT mice (N=5-6). C) NAD$^+$ and NADH concentrations and the NAD$^+$/NADH ratio in the cortex of end-stage WT (N=6) and ALS (N=7) mice. D-E) Western blot images and summary data of NAD pathway salvage from cortex of end-stage of ALS mice (N=5) and age-matched WT mice (N=5). Data were normalized to β-actin of WT mice. *p<0.05; **p<0.01; and ***p<0.001, Student's T-test.

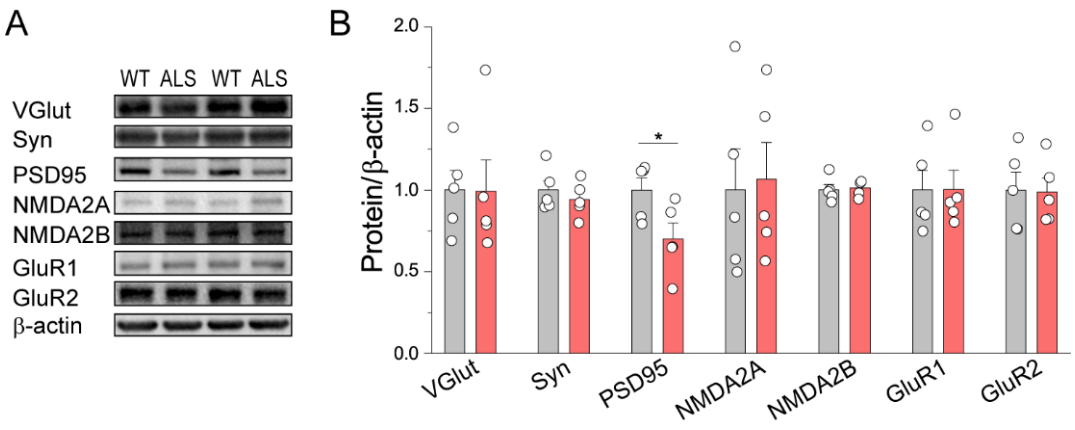

Figure 4.3. Western blot analysis of synaptic proteins. A-B) Western blot images (A) and summary data (B) of synaptic proteins from cortex of end-stage of ALS mice (N=5) and age-matched WT mice (N=5). Data were normalized to β-actin of WT mice. *$p<0.05$, Student's T-test.

4.4.2 NMN supplementation extends lifespan and reduces motor dysfunction of SOD1^{G93A} ALS mice

Given that NAD levels were reduced in ALS mice, we studied whether dietary supplementation of NAD^+ precursor NMN had any beneficial effects on disease progression in SOD1^{G93A} ALS mouse model. SOD1^{G93A} mice were fed either a diet of standard mouse chow (ALS mice) or standard mouse chow supplemented with NMN (NMN diet, ALS^{+NMN} mice) beginning at 8 weeks of age (Fig. 4.4A).

After 10 weeks of either the standard or our NMN diet, ALS mice were not paralyzed but had noticeably impaired mobility (Fig. 4.4B). ALS^{+NMN} mice had a 5-day increase in median lifespan (138 days ALS mice vs 143 days ALS^{+NMN} mice; χ^2=0.089) (Fig. 4.4C-D), suggesting that NMN supplementation has a modest effect on lifespan extension. Nevertheless, ALS and ALS^{+NMN} mice had similar body weight loss during the testing period (Fig. 4.4E). One of the most prominent aspects of ALS is the progressive decline in motor function, therefore, we performed various motor behavior tests, starting prior to symptom on-set, to determine if NMN is beneficial for motor function. ALS^{+NMN} mice exhibited slower motor impairment in both rotarod and hanging wire tests, with a two-week delay in dysfunction (Fig. 4.4F-G) however, four-limb grip force was not different between ALS and ALS^{+NMN} mice until 18 weeks of age (Fig. 4.4H). Open field testing was used to measure voluntary movement. While there was no difference in activity prior to symptom appearance, ALS^{+NMN} mice were more active, having increased distance travelled and mean speed, reduced immobile time, but similar maximal speed compared with ALS mice (Fig. 4.4I-L).

In addition to the weekly behavior tests, we also assessed walking gait by measuring stride length and stride width (Fig. 4.4M). We analyzed mice at three age time

points corresponding to disease progression in $SOD1^{G93A}$ mice: 60 (pre-symptomatic), 90 (early symptomatic), and 120 (symptomatic) days old. Both ALS and ALS^{+NMN} mice had altered walking gaits relative to WT mice. However, ALS^{+NMN} mice had improved forelimb and hindlimb stride length compared to ALS mice (Fig. 4.4N-O) but appeared to have similar forelimb and hindlimb stride widths (Fig. 4.4P-Q). To determine how gait is changed during ALS progression, we compared stride length and width among the mouse groups between 60-90, 90-120, and 60-120 days old (Table 4.1). From 60-90 days, ALS mice stride length was unchanged but both WT and ALS^{+NMN} mice had a significant increase. However, from 60-120 days, ALS mice had significant decrease in forelimb and hindlimb stride length (forelimb, $p=6.16x10^{-5}$; hindlimb, $p=1.80x10^{-5}$), while the forelimb and hindlimb stride lengths for ALS^{+NMN} mice at 60 days and 120 days was not significantly different (forelimb, p=0.38; hindlimb, p=0.55) (Table 4.1). Thus, our NMN diet appeared to slow the changes to walking gait reduction in ALS mice.

Overall, these results suggest that NMN supplementation can slow the progression of motor impairment, extend life span, and is beneficial against ALS.

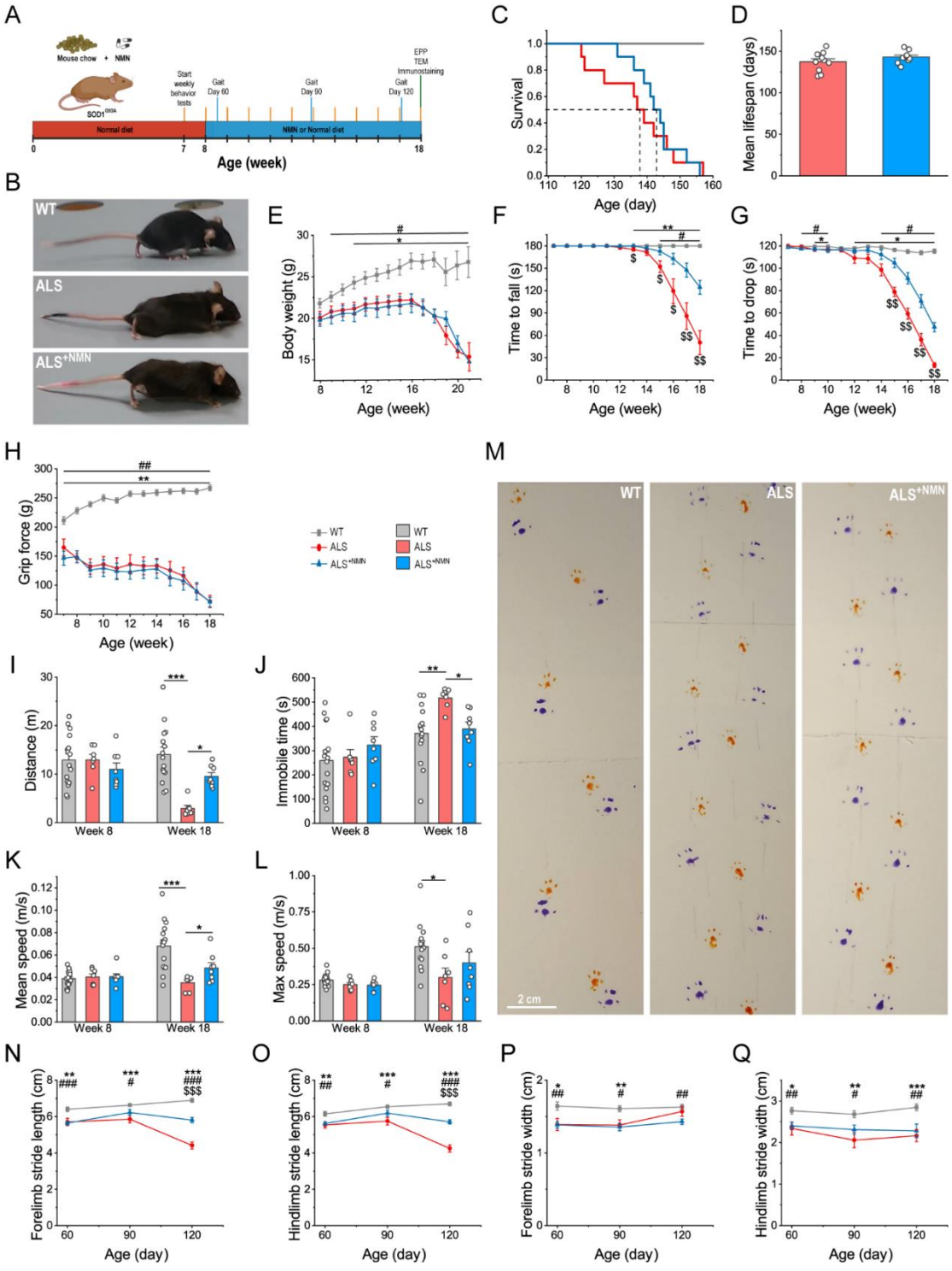

Figure 4.4. NMN delayed motor and gait impairments in ALS mice. A) Experimental timeline. B) 18-week-old WT, ALS, and ALS^{+NMN} mice. C-D) Survival curve (C) and mean lifespan (D) for WT (N=10), ALS (N=10), and ALS+NMN (N=10). Dashed lines represent median lifespan (ALS=138 days and ALS^{+NMN} =143 days). E-H) Weekly behavior assessment for WT (N=15-26), ALS (N=7-17), and ALS^{+NMN} (N=8-18).

E) Body weight. F) Accelerated rotarod time to fall. G) Hanging wire time to drop. H) Four limb grip force. I-L) Open field measurements over 10 min period from mice at 8 and 18 weeks old. I) Total distance. J) Immobile time. K) Mean speed. L) Maximum speed. M) Representative walking gait tracks for WT, ALS, and ALS^{+NMN} mice at 120 days. Walking gait was assessed at 60 (pre-symptomatic), 90 (early symptomatic), and 120 (late symptomatic) days. Forepaws were painted orange and hindpaws were painted purple. N) Mean forelimb stride length for WT (N=15-16, n=30-32), ALS (N=7-8, n=14-16), and ALS^{+NMN} (N=8, n=16). O) Mean hindlimb stride width for WT (N=15-16), ALS (N=7-8), and ALS^{+NMN} (N=8). P) Mean forelimb stride width for WT (N=15-16, n=30-32), ALS (N=7-8, n=14-16), and ALS^{+NMN} (N=8, n=16). Q) Mean hindlimb stride width for WT (N=15-16), ALS (N=7-8), and ALS^{+NMN} (N=8). For C, E-H, N-Q, *WT vs ALS; #WT vs ALS^{+NMN}; $ALS vs ALS^{+NMN}. For I-J, *$p<0.05$; ** $p<0.01$; ***$p<0.001$. Analyses performed using One-way ANOVA or Student's T-test. For A, created with BioRender.

Table 4.1. Test statistics for walking gait changes from 60 to 120 days old

		P-value					
		Hindlimb			Forelimb		
Stride	Age Range (days)	WT	ALS	ALS^{+NMN}	WT	ALS	ALS^{+NMN}
Length	60-90	0.0144	0.4416	0.0042	0.1403	0.5950	0.0050
	90-120	0.2550	1.1E-05	0.0232	0.0621	1.4E-05	0.0684
	60-120	0.0014	1.8E-05	0.5480	0.0051	6.2E-05	0.3750
Width	60-90	0.4841	0.2622	0.4935	0.6182	0.9386	0.6822
	90-120	0.1651	0.6589	0.8855	0.6876	0.0839	0.2880
	60-120	0.4654	0.4325	0.5079	0.8505	0.1228	0.4839

4.4.3 NMN improves synaptic transmission at NMJs

ALS is a MN disease that also affects skeletal muscle by disrupting neurotransmission at NMJs. Based on the improvements to motor function in ALS^{+NMN} mice, we investigated how the function of NMJs were impacted by our NMN diet. We recorded evoked EPPs and mEPPs from freshly isolated semitendinosus muscles from 18-week-old WT, ALS, and ALS^{+NMN} mice. We recorded EPP responses at different stimulation frequencies (10, 20, 50, 100 and 200 Hz) and analyzed the amplitudes for the first five and final five responses during the first second of stimulation (Fig. 4.5A-F). At all frequencies, EPPs recorded from WT mice were significantly larger than those from both ALS groups, however, EPPs from ALS^{+NMN} mice were larger than ALS mice. At 10 and 20 Hz, ALS^{+NMN} mice had larger EPPs for the first and last five responses (Fig. 4.5B-C). At 50 Hz, ALS^{+NMN} mice had significantly improved EPP amplitudes for the first but not the last five responses (Fig. 4.5D). At the highest stimulation frequencies (100 and 200 Hz), ALS^{+NMN} mice again had increased amplitudes for the first and last five responses (Fig. 4.5E-F). To assess whether synaptic transmission at NMJs was maintained during the stimulation, we calculated the ratio of the last five EPPs to the first five EPPs. Expectedly, WT mice had a higher ratio than both ALS and ALS^{+NMN} mice at most frequencies. At 200 Hz, the amplitude ratio for WT and ALS^{+NMN} mice was not significantly different, and both were significantly higher than ALS mice (Fig. 4.5G). This indicates ALS^{+NMN} mice have an improved ability to maintain EPPs during sustained high frequency stimulation, though the response amplitude is reduced considerably compared to healthy mice.

Spontaneous NMJ activity was determined by recording mEPPs (Fig. 4.5H). The amplitude of mEPPs was significantly decreased in ALS mice but restored in ALS^{+NMN}

mice (Fig. 4.5I). There was also a distinct shift in the probability of small mEPPs (<0.5 mV), which were more likely in ALS mice. ALS^{+NMN} mice had an increased probability of moderate mEPPs (0.5-0.8 mV), but there did not appear to be any change in very large mEPPs (>1 mV) between WT, ALS, and ALS^{+NMN} mice (Fig. 4.5J-K). However, quantal content was not different between ALS and ALS^{+NMN} mice (Fig. 4.5L). ALS^{+NMN} mice also had improved mEPP frequency compared with ALS mice (Fig. 4.5M-N). These findings show that our NMN diet was able to correct deficits to spontaneous vesicle release present in ALS mice.

To assess short-term plasticity at the NMJ, we evaluated paired-pulse facilitation by applying progressively shorter intervals between pulses. At longer intervals (20-100 ms), the facilitation ratio was similar between the three conditions, though some small differences were found (Fig. 4.6A-E). As intervals became shorter (≤10 ms), alterations to the facilitation ratio appeared. At 8 ms, ALS^{+NMN} mice had a larger facilitation ratio than ALS mice, though ALS and WT mice were not different (Fig. 4.6F-G). At 6 ms, WT and ALS^{+NMN} mice both had higher facilitation ratios (Fig. 4.6H), and at 4 ms, ALS and ALS^{+NMN} mice had similarly reduced ratios (Fig. 4.6I) with a noticeable lack of facilitation as compared with WT mice. ALS^{+NMN} mice were able to maintain facilitation until a pulse interval of 6 ms while WT mice exhibited facilitation at all intervals (Fig. 4.6J). Notably, starting at 10 ms, ALS mice displayed larger variability in the facilitation ratio compared to WT and ALS^{+NMN} mice. ALS^{+NMN} mice only had similar response variance at 4 ms (Fig. 4.6I). These results indicate that ALS mice improved short-term synaptic plasticity albeit with no improvement at very short pulse intervals.

Overall, electrophysiological recording demonstrated that diet supplementation of NMN can enhance synaptic function at NMJs in ALS.

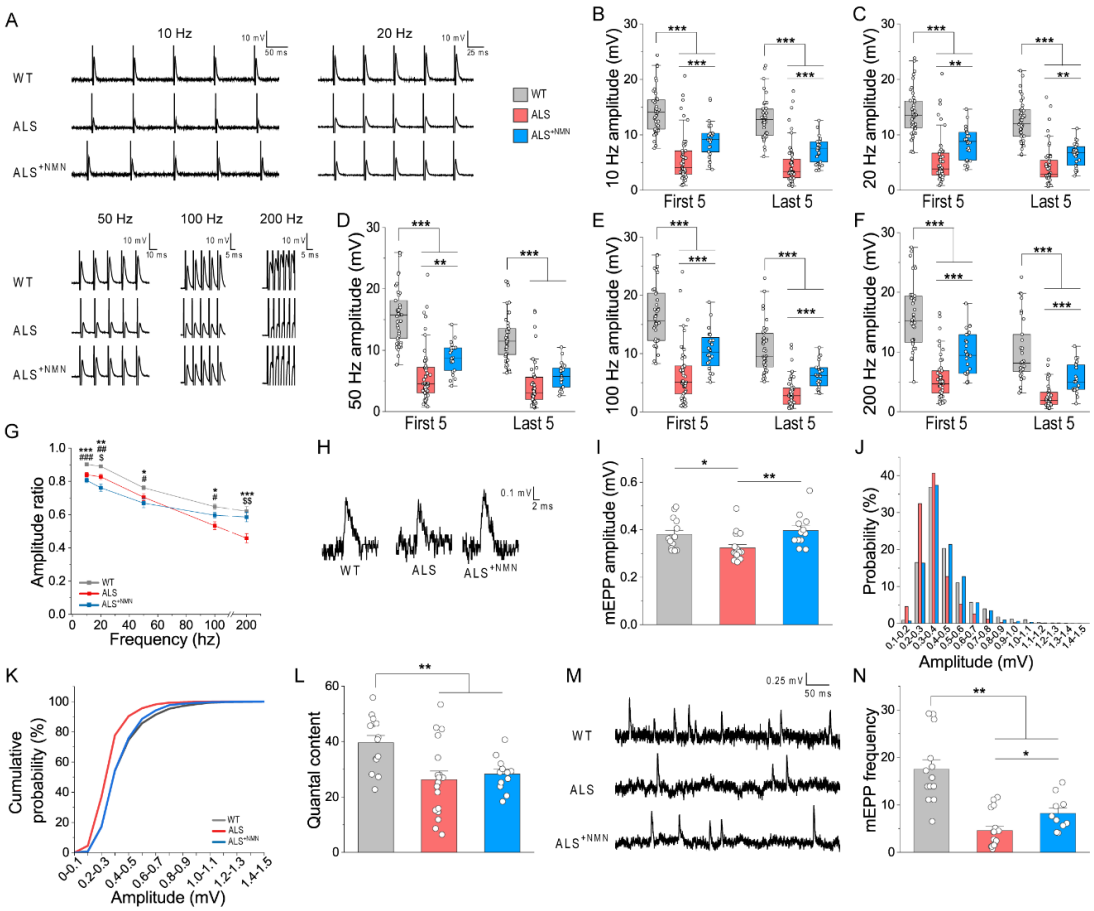

Figure 4.5. NMN improved synaptic transmission at NMJs in ALS. A) Representative traces for 10 Hz, 20 Hz, 50 Hz, 100 Hz, and 200 Hz stimulation. B-F) Mean amplitude for first 5 and last 5 responses for 10 Hz [WT (N=5, n=42), ALS (N=6, n=50), and ALS^{+NMN} (N=4, n=26)], 20 Hz [WT (N=5, n=42), ALS (N=6, n=50), and ALS^{+NMN} (N=4, n=25)] 50 Hz [WT (N=5, n=41), ALS (N=6, n=50), and ALS^{+NMN} (N=4, n=21)], 100 Hz [WT (N=5, n=39), ALS (N=6, n=49), and ALS^{+NMN} (N=4, n=24)], and 200 Hz [WT (N=5, n=29), ALS (N=6, n=43), and ALS^{+NMN} (N=4, n=23)]. G) Ratio of the mean amplitude for the last 5 responses over the mean amplitude for the first 5 responses. H) Representative mEPP amplitude trace. I) Peak mEPP amplitude. Determined using best fitting of Gaussian function for WT (N=5, n=14), ALS (N=6, n=18), and ALS^{+NMN} (N=4, n=12) mice. J) Quantal content. Quantal content was determined dividing amplitude of first 5 responses to 10 Hz stimulation by the peak mEPP amplitude for WT (N=5, n=14), ALS (N=6, n=18), and ALS^{+NMN} (N=4, n=12) mice. K-L) Histogram and cumulative probability of mEPP amplitude. M) Representative mEPP frequency trace. Analyzed 10-15 seconds, with analysis starting 5-10 seconds after

final stimulation event. N) Mean mEPP frequency (mEPP/s) for WT (N=5, n=14, ALS (N=6, n=16), and ALS^{+NMN} (N=4, n=10) mice. All mice used for recording were 18-weeks old. N, number of mice; n, number of traces analyzed. For B-F, *p<0.05; **p<0.01; ***p<0.001. For G, *WT vs ALS; #WT vs ALS^{+NMN}; $ALS vs ALS^{+NMN}. Analyses performed using Student's T-test.

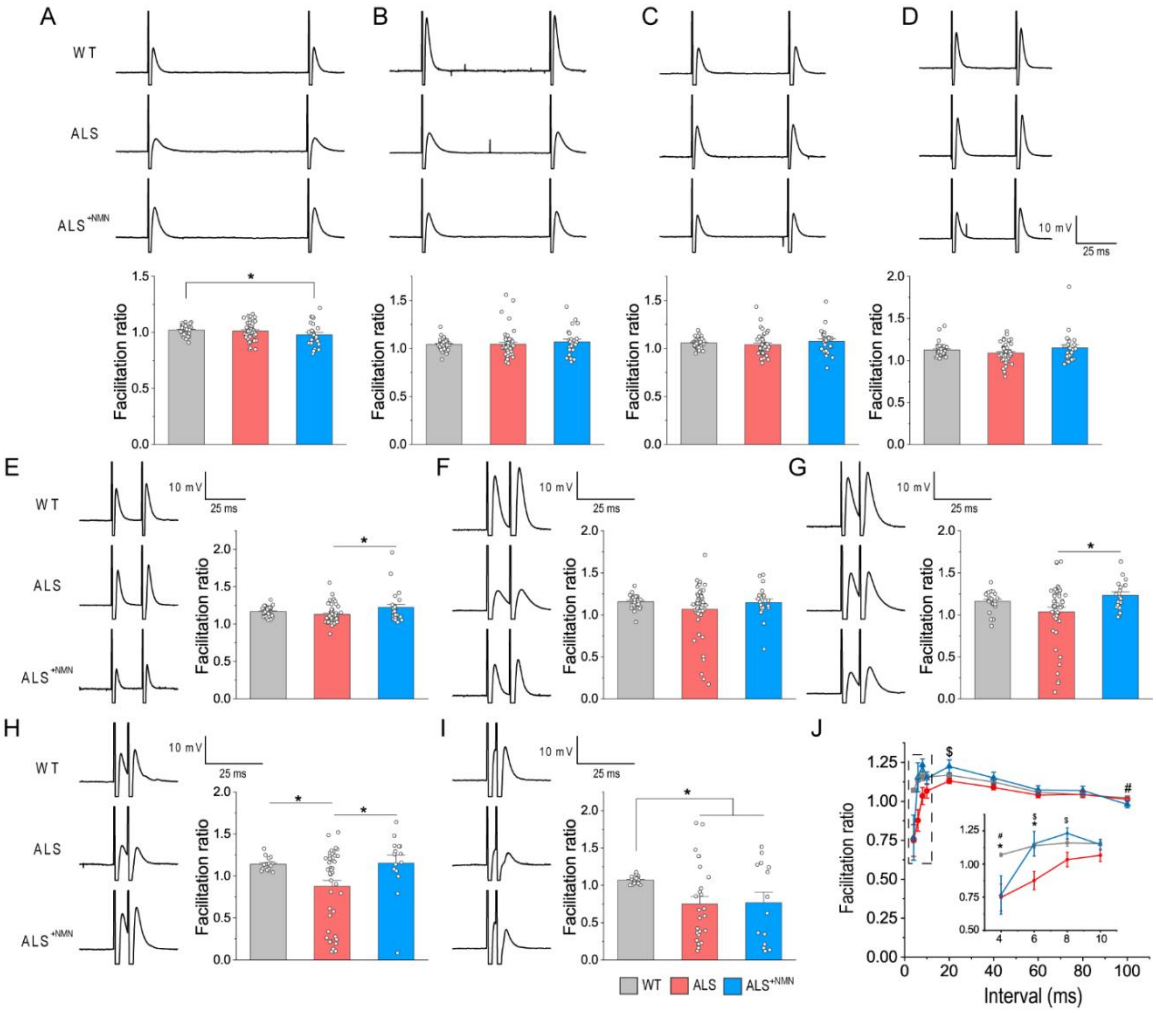

Figure 4.6. NMN increased synaptic (short-term plasticity) facilitation in ALS. A-I) Representative trace and facilitation ratio (amplitude of the second response over amplitude of the first response) for 100 ms [A, WT (N=5, n=38), ALS (N=6, n=46), and ALS^{+NMN} (N=4, n=25)], 80 ms [B, WT (N=5, n=38), ALS (N=6, n=48), and ALS^{+NMN} (N=4, n=25)], 60 ms [C, WT (N=5, n=38), ALS (N=6, n=48), and ALS^{+NMN} (N=4, n=25)], 40 ms [D, WT (N=5, n=38), ALS (N=6, n=48), and ALS^{+NMN} (N=4, n=25)],20 ms [E, WT (N=5, n=38), ALS (N=6, n=48), and ALS^{+NMN} (N=4, n=25)], 10 ms [F, WT (N=5, n=32), ALS (N=6, n=48), and ALS^{+NMN} (N=4, n=22)],8 ms [G, WT (N=5, n=26), ALS (N=6, n=45), and ALS^{+NMN} (N=4, n=19)], 6 ms [H, WT (N=5, n=20), ALS (N=6, n=45), and ALS^{+NMN} (N=4, n=16)], and 4 ms [I, WT (N=5, n=15), ALS (N=6, n=34), and ALS^{+NMN} (N=4, n=15)] pulse interval. J) Mean facilitation ratio as a function of time interval. Insert: Mean facilitation ratio from 10 ms to 4 ms interval. All mice used for recording were 18-weeks old.

N, number of mice; n, number of traces analyzed. For A-I, *p<0.05. For J, *WT vs ALS; #WT vs ALS^{+NMN}; $ALS vs ALS^{+NMN}. Analyses performed using Student's T-test.

4.4.4 NMN supplementation reduces MNJ and intermyofibrillar (IMF) mitochondrial abnormalities

We observed similar body weight reduction of ALS and ALS^{+NMN} mice compared with WT mice (Fig. 4.4E), however, compared with WT mice, ALS^{+NMN} mice had less impairment of NMJ function (Fig. 4.5-4.6) and reduction of semitendinosus muscle mass than ALS mice (Fig. 4.7A-B). Because synaptic transmission at a NMJ is related to its structure, we studied the effect of NMN on NMJ morphology and innervation [14, 17, 45-47].

At NMJs, acetylcholine receptors were labeled with α-BTX and axons were stained with neurofilament (Fig. 4.7C-D). Both motor endplate area and perimeter were reduced in ALS and ALS^{+NMN} mice, but the area reduction was smaller for ALS^{+NMN} mice (Fig. 4.7E-F). Similarly, the length and breadth of the motor endplate were improved in ALS^{+NMN} mice (Fig. 4.7G-H). The endplates were more circular in both ALS groups (Fig. 4.7I). At a functional level, NMN significantly increased the innervation ratio of NMJs, counteracting the loss caused by ALS (Fig. 4.7I-J).

Growing evidence suggest mitochondria defects in ALS human patient and mouse models [48-51], and our previous study also showed deletion of NAMPT affects mitochondrial function [52] (our cell report); therefore, using TEM we investigated whether the NMN diet influences skeletal muscle IMF mitochondria, which are important for muscle contraction (Fig. 4.7K-L). IMF mitochondrial density was reduced in both ALS conditions with no improvement by NMN (Fig. 4.7M). However, mitochondrial area and perimeter were significantly larger in ALS mice than those in ALS^{+NMN} mice (Fig. 4.7N-O). NMN also significantly increased Feret's diameter of mitochondria and restored

mitochondria circularity in ALS mice (Fig. 4.7P-Q). These results indicate that our NMN diet can alleviate some of the changes to IMF mitochondria that occurs in ALS.

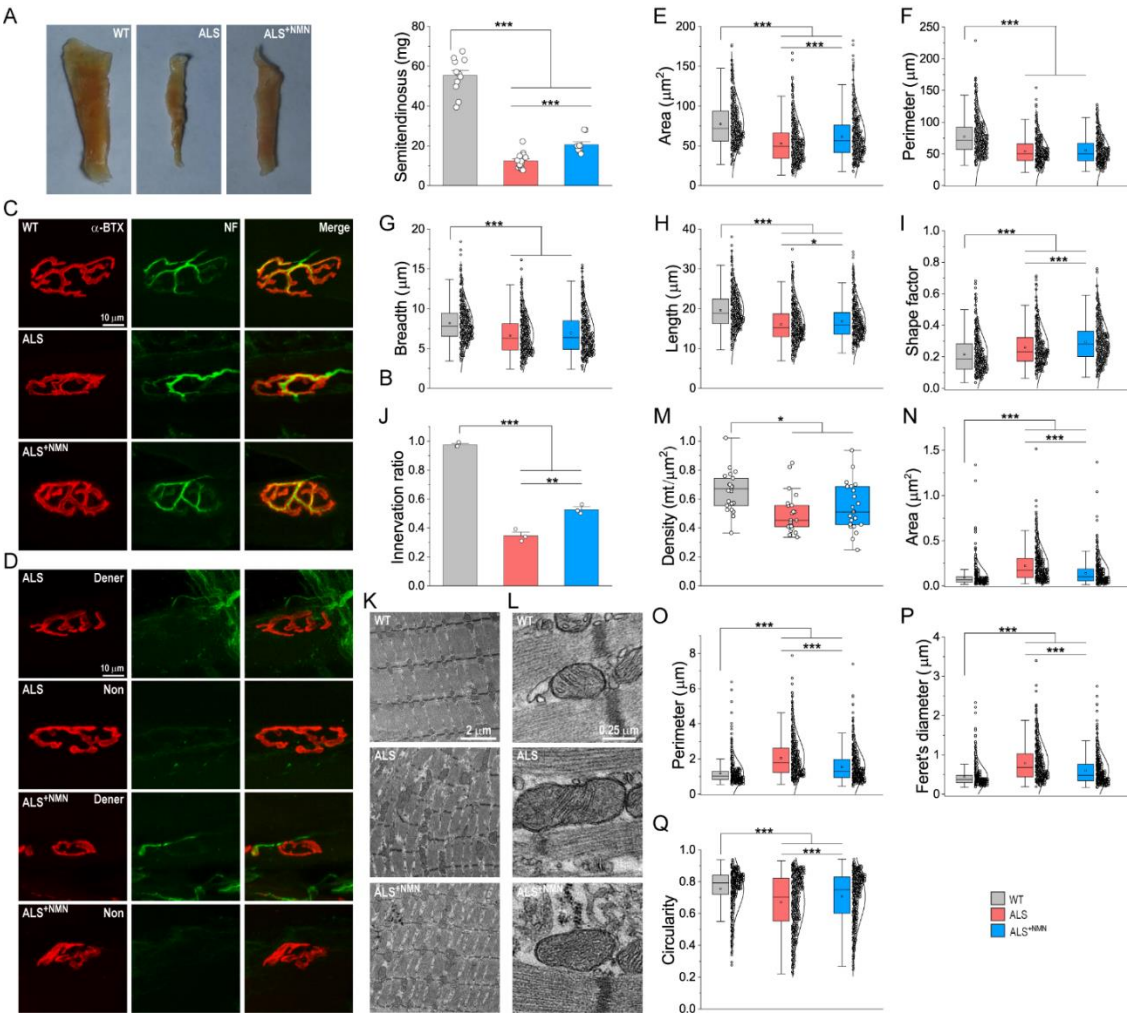

Figure 4.7. NMN diet reduced skeletal muscle and NMJ abnormalities. A-B) Representative photograph of semitendinosus muscle and mean mass for 18-week-old WT (N=6, n=11), ALS (N=10, n=14), and ALS^{+NMN} (N=6, n=9) mice. C-D) Representative innervated, denervated and non-innervated NMJs stained with BTX and neurofilaments in semitendinosus muscles from WT, ALS, and ALS^{+NMN} mice. E-I) Morphological measures of motor endplate area (E), perimeter (F), breadth (G), length (H), and shape factor (I), for WT (N=3, n=375), ALS (N=3, n=387), and ALS^{+NMN} (N=3, n=394) mice. J) NMJ innervation ratio for WT (N=3), ALS (N=3), and ALS^{+NMN} (N=3) mice. K-L) IMF mitochondria TEM images at 5000X (K) and 10000X (L). M) Mitochondrial density for WT (N=2, n=21), ALS (N=2, n=21), and ALS^{+NMN} (N=2, n=21) mice. N-Q) Morphological measures for mitochondria area (N), perimeter (O), Feret's diameter (P), and circularity (Q) for WT (N=2, n=558), ALS (N=2, n=530), and ALS^{+NMN} (N=2, n=547) mice. All mice used for analysis were 18-weeks old. N, number of mice, n, number of muscles (B), NMJs (E-J), images

(M), or mitochondria (N-Q). *p<0.05, **p<0.01, ***p<0.001. Analyses performed using One-way ANOVA or Student's T-test.

4.4.5 NMN supplementation ameliorates ALS pathology

The loss of lower MNs from the ventral horn is a hallmark of ALS. Here we examined whether NMN can ameliorate ALS pathology in spinal cord and cortex. To determine if our NMN diet improves spinal cord MN survival, we did immunostaining of cross-sectioned lumbar spinal cords from 18-week-old mice with antibodies against choline acetyltransferase (ChAT), a marker of MNs, and NeuN, a marker for neurons (Fig. 4.8A). There was no difference in ChAT+ MN number between the ALS groups, with both having a 50% reduction compared with WT mice (Fig. 4.8B). Morphologically, the area and perimeter of the ChAT+ MNs were improved in ALS^{+NMN} mice (Fig. 4.8C-D). Similarly, NMN significantly restored the length, breadth and shape in ALS^{+NMN} mice (Fig. 4.8E-G). These analyses suggest that while ALS^{+NMN} mice have similar MN number to ALS mice, they have larger size of surviving MNs with morphologies more similar to those in WT mice.

To further investigate any changes to spinal cord MNs, we assessed the mitochondrial structure using TEM (Fig. 4.8H-I). Mitochondrial density was significantly reduced in ALS mice but restored in ALS^{+NMN} mice (Fig. 4.8J). ALS mice had an increase in mitochondria area, but this was modestly corrected by the NMN diet (Fig. 4.8K). Mitochondrial perimeter and Feret's diameter were returned to normal length in ALS^{+NMN} mice (Fig. 4.8L-M), but there was no difference in mitochondrial shape between ALS and ALS^{+NMN} groups (Fig. 4.8N). Overall, these results indicate that spinal cord mitochondrial density and structure are restored to normal in ALS^{+NMN} mice.

Though primarily associated with MNs, ALS is a non-cell autonomous disease with glial cells, especially astrocytes, contributing to neuroinflammation and MN toxicity [53].

Thus, we determined whether our NMN diet had any effect on glial cell activation in lumbar spinal cords by immunostaining for Iba1, a marker of microglia, and GFAP, a marker of astrocytes (Fig. 4.9A-B). We found that both Iba1 and GFAP signals were increased in the ALS groups (Fig. 4.9C-D); however, the ALS^{+NMN} mice had a significant reduction in GFAP signal compared to ALS mice (Fig. 4.9D). This suggests that NMN can reduce astrocyte activation in the lumbar spinal cord.

Finally, we examined whether our NMN diet had any benefits to the brain. In the motor cortex, there was no difference in NeuN intensity between the three groups but ALS^{+NMN} mice had an increase in NeuN+ cell number (Fig. 4.10A-C). ALS and ALS^{+NMN} mice had similar GFAP intensities that were significantly lower compared to WT mice and no difference in GFAP+ cell density was found among 3 groups (Fig. 4.10D-F). There was no difference in Iba1 intensity, though ALS^{+NMN} mice had a significant reduction in Iba+ cells compared to ALS mice (Fig. 4.10G-I). In the hippocampus, GFAP intensity and the density of GFAP+ astrocytes were significantly higher in both ALS and ALS^{+NMN} mice than in WT mice, but there was no difference between ALS and ALS^{+NMN} mice (Fig. 4.10J-L). There was no difference in Iba1 intensity and both ALS conditions had significantly more Iba+ cells (Fig. 4.10M-O). Glial cells in the brains of ALS mice do not appear to be strongly impacted by our NMN diet.

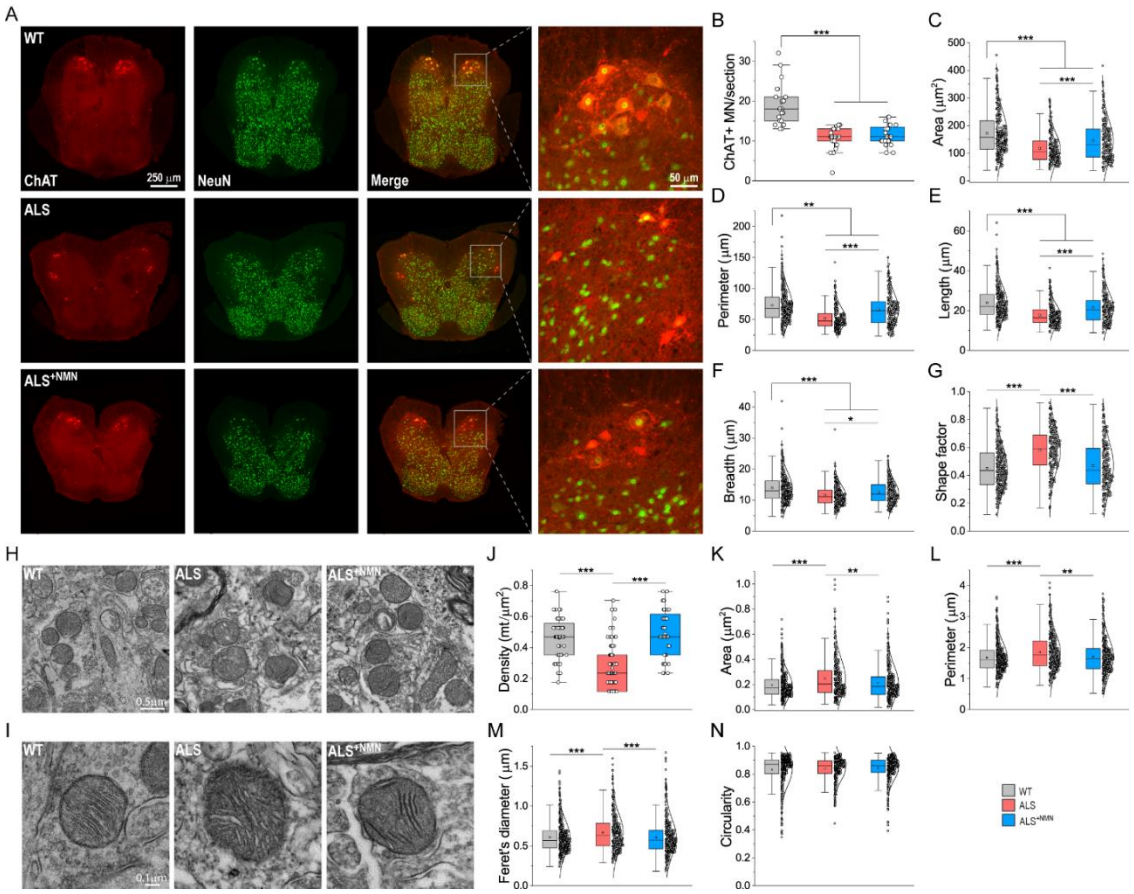

Figure 4.8. NMN improved spinal cord MN and mitochondrial morphology in ALS^{+NMN} mice. A) Representative spinal cord image for WT, ALS, and ALS^{+NMN} mice. B) ChAT+ MN density for WT (N=2, n=21), ALS (N=2, n=21), and ALS^{+NMN} (N=2, n=24) mice. C-G) Morphological measures of MN area (C), perimeter (D), length (E), breadth (F), and shape factor (G), for WT (N=2, n=316), ALS (N=2, n=235), and ALS^{+NMN} (N=2, n=226). H-I) TEM image of ventral horn mitochondria at 5000X (H) and 10000X (I). J) Mitochondrial density for WT (N=2, n=60), ALS (N=2, n=70), and ALS^{+NMN} (N=2, n=44) mice. K-N) Morphological analyses for mitochondria area (D), perimeter (E), Feret's diameter (F), and circularity (H) for WT (N=2, n=475), ALS (N=2, n=334), and ALS^{+NMN} (N=2, n=384) mice. All mice used for analysis were 18-weeks old. N, number of mice; n, number of sections (B), MNs (C-G), images (J), or mitochondria (K-N). *p<0.05, **p<0.01, ***p<0.001. Analyses performed using One-Way ANOVA or Student's T-test.

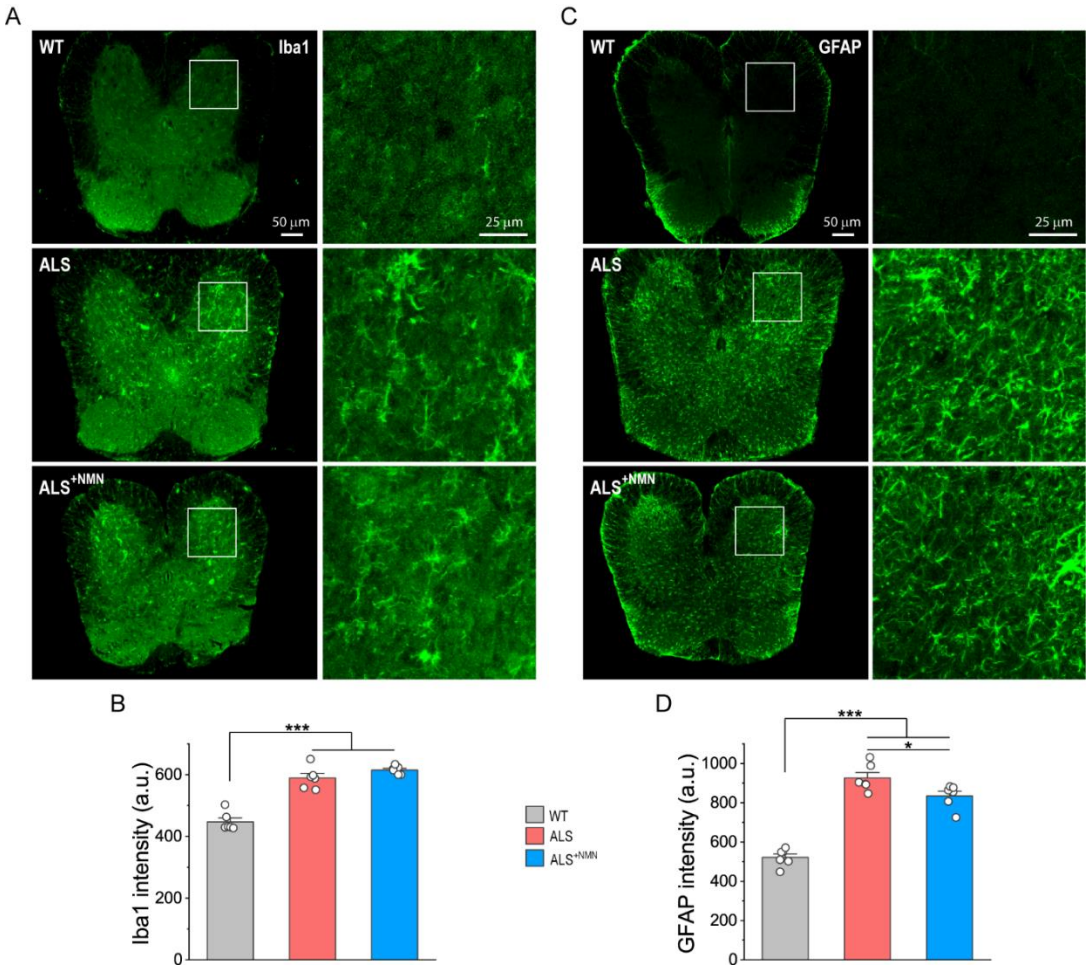

Figure 4.9. NMN reduced astrocyte activation in lumbar spinal cord of ALS mice. A-B) Representative Iba1 image (A) and mean intensity (B) for WT (N=2, n=6), ALS (N=2, n=6), and ALS^{+NMN} (N=2, n=6) mice. C-D) Representative GFAP image (C) and mean intensity (D) for WT (N=2, n=6), ALS (N=2, n=6), and ALS^{+NMN} (N=2, n=6) mice. N, number of mice; n, average intensity in ventral horns from one section. All mice used for analysis were 18-weeks old. *p<0.05 and ***p<0.001, Student's T-test.

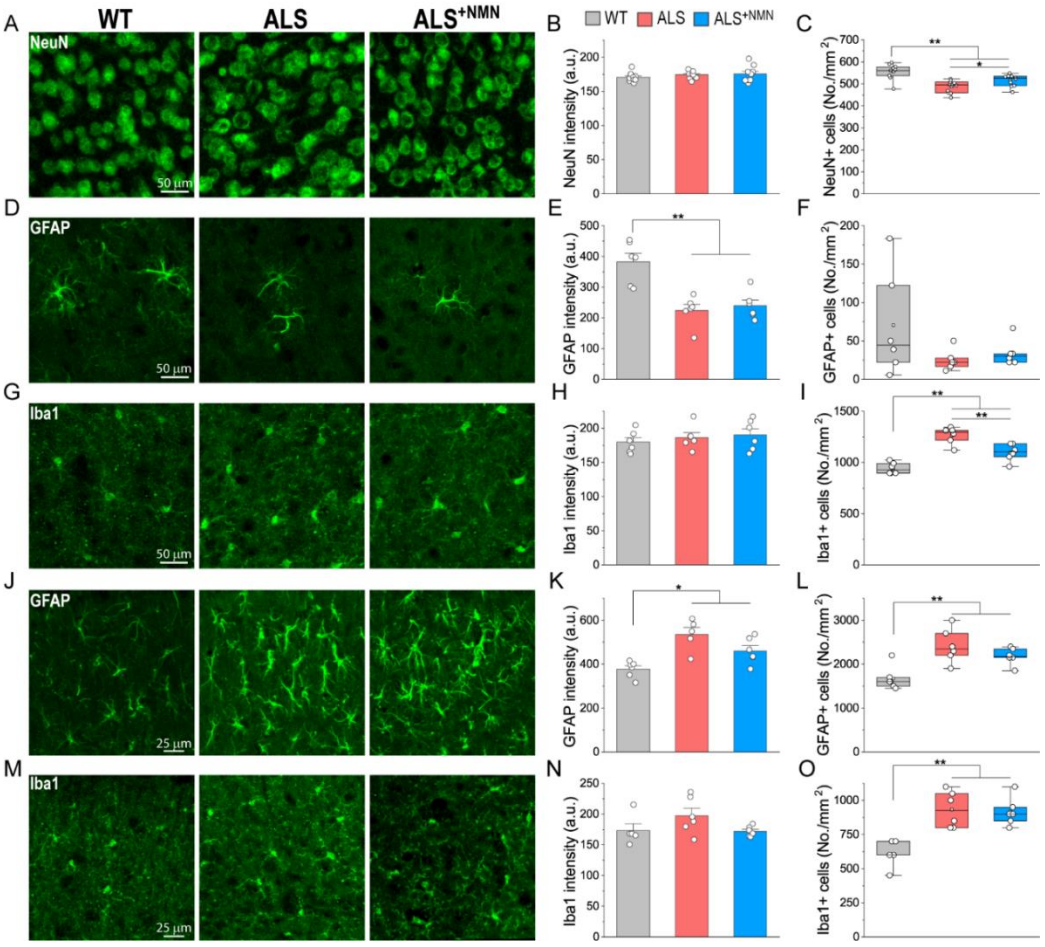

Figure 4.10. Glial cell activation in motor cortex and hippocampus of ALS^{+NMN} mice. A-C) Representative NeuN images (A) and mean NeuN intensity (B) and NeuN+ density (C) in motor cortex. D-F) Representative motor cortex GFAP images (D), mean GFAP intensity (E) and density of GFAP+ astrocytes (F). G-I) Representative motor cortex Iba1 images (G), mean Iba1 intensity (G) and density of Iba1+ microglia (H). J-L) Representative CA1 hippocampal GFAP images (J), mean GFAP intensity (K) and density of GFAP+ astrocytes (L). M-O) Representative CA1 hippocampal Iba1 images (M), mean Iba1 intensity (N) and density of Iba1+ microglia (O). For staining, WT (N=2, n=5-12), ALS (N=2, n=6-11), and ALS^{+NMN} (N=2, n=10). All mice used for analysis were 18-weeks old. N, number of mice; n, average from 1 slice. **p<0.01, Student's T-test.

4.5 Discussion

In this study, we investigated the effect of dietary NMN on ALS using mouse model. Our findings demonstrated that NMN delayed motor and gait impairments that occur as ALS progresses and modestly extended lifespan of ALS mice. Importantly, NMJs, one of the earliest affected sites in ALS, benefited greatly from our NMN diet. ALS^{+NMN} mice had improved neurotransmission, motor endplate morphology, and innervation at NMJs. Skeletal muscle atrophy and mitochondrial morphology were partially restored in ALS by NMNs. MN survival was not affected, though MNs were larger in ALS^{+NMN} mice. Glial cell activation was reduced in ventral horn in ALS^{+NMN} mice compared with ALS mice. Thus, NMN supplementation to ALS mouse diet can exert various beneficial effects against ALS.

Prior studies only reported a loss of blood NAD at end-stage [22, 23], we found NAD availability was reduced in the blood at 6 weeks of age, long before the appearance of motor deficits. Additionally, our results indicate that the NAD decline follows ALS disease, with the NAD deficit becoming larger as symptoms appear and progress. Impairments to NAD homeostasis are likely due to either decreased biosynthesis or increased consumption. Our result is consistent with a previous study where NAMPT expression was reduced, but not significantly, in brains of ALS mice [54]. In ALS spinal cords, NAMPT and NMNAT2 expression are significantly altered, indicating the brain and spinal cord may undergo different changes [14, 26]. While we did not find there is a reduction in the protein expression levels of enzymes in the salvage pathway it is possible the activity of other NAD synthesis pathways might be reduced. It is also possible that increased acetylation of NAMPT might reduce NAMPT activity, as reported in aged mice

[55, 56]. Increased NAD consumption by PARP1 or CD38 could also cause NAD^+ reduction in ALS as inhibition or knockout of PARP1 or CD38 can nearly restore NAD^+ levels [57, 58]. The mechanism by which NAD homeostasis is disrupted in ALS warrants further study.

How impactful NAD^+ precursors are to survival appears variable in different studies. NAM and NR have each demonstrated modest to significant increases on survival in ALS mice [22, 25, 26, 54]. We found ALS^{+NMN} mice had a 5-day increase in median lifespan, suggesting that dietary supplementation of NMN might be a good strategy to delay ALS progression like what we observed in NAMPT conditional KO mice [14].

To determine if NMN impacted motor function of ALS mice, we conducted a battery of motor behavior tests. We observed a delay in the motor deficits in ALS^{+NMN} mice, consistent with previous findings where increased NAD^+ availability improved motor performance in neurodegenerative diseases [14, 17, 59, 60]. This is also consistent with past studies that NR or NAM significantly slowed motor decline in ALS [22, 25, 54]. For walking gait, while WT strides were longer, ALS^{+NMN} and WT mice experienced increases in stride length from 60 to 90 days old, whereas ALS mice stride length was unchanged. Interestingly, this timeframe corresponds to symptom onset [61]. ALS^{+NMN} mice also had longer strides at 120 days. Our results are consistent with the results from ALS mice administered P7C3, a purported NAMPT activating molecule [27]. Those mice also had improved accelerated rotarod performance and experienced similar changes to stride length between 90 and 120 days, suggesting similar effects of NMN and P7C3 on motor performance.

Electrophysiological recording of EPP is a gold standard approach to assess NMJ function [62, 63], however, how it is affected by NAD^+ precursors in ALS has not been reported. Consistent with previous reports [30, 64, 65], we found ALS mice had reduced evoked and spontaneous synaptic activity and were less capable of maintaining responses at all frequencies. We examined the effect of stimulation frequencies and paired-pulse stimulation on EPP at the same NMJ and demonstrated that NMN can strengthen synaptic transmission at NMJ. Relative to ALS mice, ALS^{+NMN} mice had higher EPP amplitude, maintained larger response amplitude at higher stimulation frequencies and higher short-term plasticity. These results indicate ALS^{+NMN} mice had stronger neurotransmitter release compared to ALS mice, with NMJs of ALS^{+NMN} mice having improved synaptic vesicle (SV) release and/or cycling. A slowed SV cycle has been observed in an ALS zebrafish model, with impaired exocytosis [66]; $SOD1^{G93A}$ ALS mice also have reduced SV density in diaphragm motor nerve terminals [67]. These results are consistent with our previous findings that NMN can improve the SV cycle in NMJs in mice undergoing significant neurodegeneration [17].

Results from paired-pulse stimulation indicated short-term plasticity at the NMJ was improved in ALS^{+NMN} mice. ALS^{+NMN} and WT had similar facilitation until the shortest pulse interval while ALS mice exhibited no facilitation to short pulse intervals ($\leq$10 ms). Lack of facilitation may indicate increased SV release probability or cycling defects at NMJs in ALS mice [64, 67]. We did not observe an increase in quantal content at NMJ in ALS mice, suggesting a decrease of available SVs is likely responsible for the short-term plasticity differences [68]. A reduction of SVs would be consistent with the results from responses at different stimulation frequencies. More investigation is needed to

determine whether release probability and/or vesicle number is responsible for the short-term plasticity benefits in ALS^{+NMN} mice.

Our NMN diet improved spontaneous NMJ activity, with both mEPP amplitude and frequency increased at NMJs. This indicates ALS^{+NMN} mice have improved SV movement within the nerve terminal. Curiously, there was no increase in quantal content in ALS^{+NMN} mice compared with ALS mice, suggesting that the neurotransmitter release is not changed by NMN supplementation. One possible explanation for this could be due to the age of ALS mice when they were fed with our NMN diet. Motor behavior decline in $SOD1^{G93A}$ mice may not appear until 80-100 days, however significant physiological changes have already occurred in these mice well before this time periods. In addition to the early NAD loss we found, alterations to neurotransmission, energy metabolism, and NMJ architecture also occur prior to observable phenotypic changes [30, 69, 70]. Another possibility is that improving the movement of SVs is not enough to entirely ameliorate the neurotransmission changes in ALS mice. More investigation is needed to better understand how the SV cycle is disrupted and how to improve neurotransmission in the NMJs of ALS mice. The cause of the vesicle cycling/release problems could be related to TGF-β. Increased TGF- β has been found to be a shared characteristic across ALS mice and human patients [71-73]. TGF-β can affect both synaptic function and MN degeneration at NMJs [73, 74]. In WT mice, increased TGF-β significantly affected mEPP amplitude and quantal content, similar to what we observed in our ALS and ALS^{+NMN} mice [75]. Interestingly, the NAD^+ consuming enzyme SIRT6, reported to regulate TGF-β signaling activity, is reduced in ALS patient spinal cords [26]. The neuroprotective effects of NAD^+ precursor treatments require SIRT6 and the knockdown of SIRT6 in astrocytes prevents these

treatments from counteracting the astrocytic neurotoxicity observed in ALS [76, 77]. More studies are required to determine whether TGF-β may be involved in the synaptic changes in NMN supplemented ALS mice.

ALS^{+NMN} mice showed improvements in hindlimb skeletal muscle, specifically to motor endplates, mass, and mitochondrial structure. This was an important finding given mutant SOD1 is harmful to skeletal muscle and complements previous studies that NAD^+ precursors were beneficial to degenerating or aged muscles [15, 16, 78, 79]. ALS^{+NMN} mice also had increased innervation and motor endplate size. The early and progressive loss of motor endplate innervation in ALS mice has been established [80]. Our study increases the known benefits of NAD^+ precursors on ALS pathology because previous studies on ALS mice did not investigate NMJs [22, 26]. NMN prevented morphological changes to IMF mitochondria, similar to what we found previously in a conditional knockout mouse with an ALS-like phenotype [17]. These results suggest that ALS skeletal muscles benefit from our NMN diet through restoring mitochondrial function.

Although MN density was not affected, our NMN diet also elicited many changes in the spinal cord of ALS mice. Morphology of MNs and their mitochondria as well as astrocyte reactivity were positively affected in spinal cord. Importantly, NMN can restore mitochondrial density in ALS, indicating a positive effect on energy metabolism. The reduced GFAP reactivity was also observed in ALS mice provided with NR [22, 26]. *In vitro*, cortical MNs from TDP-43 ALS mice treated with NMN had improved morphology [24]. MN loss and microglial activation was not prevented by NMN, which is unlike previous reports that NR or P7C3 increased MN survival and reduced microglial reactivity [22, 26, 27]. In the brain, we found increased NeuN+ cell number in the motor cortex and

reduced reactive gliosis in motor cortex and hippocampus of ALS^{+NMN} mice as compared with ALS mice. It was reported that NR treatments did increase neurogenesis in symptomatic ALS mice [54], making it possible our NMN diet has a similar impact on neurogenesis.

In summary, our findings demonstrate that NMN supplementation in diet can extend lifespan and enhance motor performance and NMJ function in ALS mice. The current study provides new insights into the role of NMN supplementation in the delay of development of ALS. Future study is needed to determine how NMN can improve mitochondrial function and bioenergetics in skeletal muscle and MNs, and in conjunction with other interventions such as the inhibitors of NAD^+-consuming enzymes, may be best incorporated into an ALS treatment regimen.

4.6 References

1. Zufiria, M., et al., *ALS: A bucket of genes, environment, metabolism and unknown ingredients.* Prog Neurobiol, 2016. **142**: p. 104-129.
2. Mejzini, R., et al., *ALS Genetics, Mechanisms, and Therapeutics: Where Are We Now?* Front Neurosci, 2019. **13**(1310): p. 1310.
3. Agrawal, M. and A. Biswas, *Molecular diagnostics of neurodegenerative disorders.* Front Mol Biosci, 2015. **2**: p. 54.
4. Sturmey, E. and A. Malaspina, *Blood biomarkers in ALS: challenges, applications and novel frontiers.* Acta Neurol Scand, 2022. **146**(4): p. 375-388.
5. Gwathmey, K.G., et al., *Diagnostic delay in amyotrophic lateral sclerosis.* Eur J Neurol, 2023. **n/a**(n/a).
6. Alhindi, A., I. Boehm, and H. Chaytow, *Small junction, big problems: Neuromuscular junction pathology in mouse models of amyotrophic lateral sclerosis (ALS).* J Anat, 2022. **241**(5): p. 1089-1107.
7. Verdin, E., *NAD(+) in aging, metabolism, and neurodegeneration.* Science, 2015. **350**(6265): p. 1208-13.
8. Revollo, J.R., A.A. Grimm, and S. Imai, *The NAD biosynthesis pathway mediated by nicotinamide phosphoribosyltransferase regulates Sir2 activity in mammalian cells.* J Biol Chem, 2004. **279**(49): p. 50754-63.
9. Canto, C., K.J. Menzies, and J. Auwerx, *NAD(+) Metabolism and the Control of Energy Homeostasis: A Balancing Act between Mitochondria and the Nucleus.* Cell Metab, 2015. **22**(1): p. 31-53.
10. Chini, C.C.S., et al., *Evolving concepts in NAD(+) metabolism.* Cell Metab, 2021. **33**(6): p. 1076-1087.

11. Lautrup, S., et al., *NAD(+) in Brain Aging and Neurodegenerative Disorders.* Cell Metab, 2019. **30**(4): p. 630-655.

12. Covarrubias, A.J., et al., *NAD(+) metabolism and its roles in cellular processes during ageing.* Nat Rev Mol Cell Biol, 2021. **22**(2): p. 119-141.

13. Lundt, S. and S. Ding, *NAD(+) Metabolism and Diseases with Motor Dysfunction.* Genes (Basel), 2021. **12**(11): p. 1776.

14. Wang, X., et al., *Deletion of Nampt in Projection Neurons of Adult Mice Leads to Motor Dysfunction, Neurodegeneration, and Death.* Cell Rep, 2017. **20**(9): p. 2184-2200.

15. Ryu, D., et al., *NAD+ repletion improves muscle function in muscular dystrophy and counters global PARylation.* Sci Transl Med, 2016. **8**(361): p. 361ra139.

16. Mills, K.F., et al., *Long-Term Administration of Nicotinamide Mononucleotide Mitigates Age-Associated Physiological Decline in Mice.* Cell Metab, 2016. **24**(6): p. 795-806.

17. Lundt, S., et al., *The effect of NAMPT deletion in projection neurons on the function and structure of neuromuscular junction (NMJ) in mice.* Sci Rep, 2020. **10**(1): p. 99.

18. Hou, Y., et al., *NAD(+) supplementation normalizes key Alzheimer's features and DNA damage responses in a new AD mouse model with introduced DNA repair deficiency.* Proc Natl Acad Sci U S A, 2018. **115**(8): p. E1876-E1885.

19. Li, F., C. Wu, and G. Wang, *Targeting NAD Metabolism for the Therapy of Age-Related Neurodegenerative Diseases.* Neurosci Bull, 2023.

20. Browne, S.E., et al., *Bioenergetic abnormalities in discrete cerebral motor pathways presage spinal cord pathology in the G93A SOD1 mouse model of ALS.* Neurobiol Dis, 2006. **22**(3): p. 599-610.

21. Dupuis, L., et al., *Evidence for defective energy homeostasis in amyotrophic lateral sclerosis: benefit of a high-energy diet in a transgenic mouse model.* Proc Natl Acad Sci U S A, 2004. **101**(30): p. 11159-64.

22. Obrador, E., et al., *Nicotinamide Riboside and Pterostilbene Cooperatively Delay Motor Neuron Failure in ALS SOD1(G93A) Mice.* Mol Neurobiol, 2021. **58**(4): p. 1345-1371.

23. Roderer, P., et al., *Increased ROS Level in Spinal Cord of Wobbler Mice due to Nmnat2 Downregulation.* Mol Neurobiol, 2018. **55**(11): p. 8414-8424.

24. Gautam, M., et al., *Mitochondrial dysregulation occurs early in ALS motor cortex with TDP-43 pathology and suggests maintaining NAD(+) balance as a therapeutic strategy.* Sci Rep, 2022. **12**(1): p. 4287.

25. Blacher, E., et al., *Potential roles of gut microbiome and metabolites in modulating ALS in mice.* Nature, 2019. **572**(7770): p. 474-480.

26. Harlan, B.A., et al., *Evaluation of the NAD(+) biosynthetic pathway in ALS patients and effect of modulating NAD(+) levels in hSOD1-linked ALS mouse models.* Exp Neurol, 2020. **327**: p. 113219.

27. Tesla, R., et al., *Neuroprotective efficacy of aminopropyl carbazoles in a mouse model of amyotrophic lateral sclerosis.* Proc Natl Acad Sci U S A, 2012. **109**(42): p. 17016-21.

28. Harlan, B.A., et al., *Enhancing NAD+ Salvage Pathway Reverts the Toxicity of Primary Astrocytes Expressing Amyotrophic Lateral Sclerosis-linked Mutant Superoxide Dismutase 1 (SOD1).* J Biol Chem, 2016. **291**(20): p. 10836-46.

29. Hatzipetros, T., et al., *A Quick Phenotypic Neurological Scoring System for Evaluating Disease Progression in the SOD1-G93A Mouse Model of ALS.* J Vis Exp, 2015(104): p. e53257.

30. Rocha, M.C., et al., *Early changes of neuromuscular transmission in the SOD1(G93A) mice model of ALS start long before motor symptoms onset.* PLoS One, 2013. **8**(9): p. e73846.

31. Olivan, S., et al., *Comparative study of behavioural tests in the SOD1G93A mouse model of amyotrophic lateral sclerosis.* Exp Anim, 2015. **64**(2): p. 147-53.

32. Knippenberg, S., et al., *Significance of behavioural tests in a transgenic mouse model of amyotrophic lateral sclerosis (ALS).* Behav Brain Res, 2010. **213**(1): p. 82-7.

33. Klein, S.M., et al., *Noninvasive in vivo assessment of muscle impairment in the mdx mouse model--a comparison of two common wire hanging methods with two different results.* J Neurosci Methods, 2012. **203**(2): p. 292-7.

34. Dong, W., et al., *Knock in of a hexanucleotide repeat expansion in the C9orf72 gene induces ALS in rats.* Animal Model Exp Med, 2020. **3**(3): p. 237-244.

35. Jambeau, M., et al., *Comprehensive evaluation of human-derived anti-poly-GA antibodies in cellular and animal models of C9orf72 disease.* Proc Natl Acad Sci U S A, 2022. **119**(49): p. e2123487119.

36. Wertman, V., et al., *Low-Cost Gait Analysis for Behavioral Phenotyping of Mouse Models of Neuromuscular Disease.* J Vis Exp, 2019(149): p. e59878.

37. Polo-Parada, L., et al., *NCAM 180 acting via a conserved C-terminal domain and MLCK is essential for effective transmission with repetitive stimulation.* Neuron, 2005. **46**(6): p. 917-31.

38. Leduc-Gaudet, J.P., et al., *Mitochondrial morphology is altered in atrophied skeletal muscle of aged mice.* Oncotarget, 2015. **6**(20): p. 17923-37.

39. Wang, X., et al., *Subcellular NAMPT-mediated NAD(+) salvage pathways and their roles in bioenergetics and neuronal protection after ischemic injury.* J Neurochem, 2019. **151**(6): p. 732-748.

40. Zhang, N., et al., *GLAST-CreER(T2) mediated deletion of GDNF increases brain damage and exacerbates long-term stroke outcomes after focal ischemic stroke in mouse model.* Glia, 2020. **68**(11): p. 2395-2414.

41. Wang, X., H. Li, and S. Ding, *Pre-B-cell colony-enhancing factor protects against apoptotic neuronal death and mitochondrial damage in ischemia.* Sci Rep, 2016. **6**: p. 32416.

42. Nishimura, A.L. and N. Arias, *Synaptopathy Mechanisms in ALS Caused by C9orf72 Repeat Expansion.* Front Cell Neurosci, 2021. **15**: p. 660693.

43. Rothstein, J.D., L.J. Martin, and R.W. Kuncl, *Decreased Glutamate Transport by the Brain and Spinal Cord in Amyotrophic Lateral Sclerosis.* New England Journal of Medicine, 1992. **326**(22): p. 1464-1468.

44. Baczyk, M., et al., *Synaptic restoration by cAMP/PKA drives activity-dependent neuroprotection to motoneurons in ALS.* J Exp Med, 2020. **217**(8).

45. Ryten, M., et al., *Abnormalities in neuromuscular junction structure and skeletal muscle function in mice lacking the P2X2 nucleotide receptor.* Neuroscience, 2007. **148**(3): p. 700-11.

46. Fralish, Z., et al., *Neuromuscular Development and Disease: Learning From in vitro and in vivo Models.* Front Cell Dev Biol, 2021. **9**: p. 764732.

47. Zou, S. and B.X. Pan, *Post-synaptic specialization of the neuromuscular junction: junctional folds formation, function, and disorders.* Cell Biosci, 2022. **12**(1): p. 93.

48. Luo, G., et al., *Defective mitochondrial dynamics is an early event in skeletal muscle of an amyotrophic lateral sclerosis mouse model.* PLoS One, 2013. **8**(12): p. e82112.

49. Crugnola, V., et al., *Mitochondrial respiratory chain dysfunction in muscle from patients with amyotrophic lateral sclerosis.* Arch Neurol, 2010. **67**(7): p. 849-54.

50. Smith, E.F., P.J. Shaw, and K.J. De Vos, *The role of mitochondria in amyotrophic lateral sclerosis.* Neurosci Lett, 2019. **710**: p. 132933.

51. Krasnianski, A., et al., *Mitochondrial changes in skeletal muscle in amyotrophic lateral sclerosis and other neurogenic atrophies.* Brain, 2005. **128**(Pt 8): p. 1870-6.

52. Lundt, S., et al., *Metabolomic and transcriptional profiling reveals bioenergetic stress and activation of cell death and inflammatory pathways in vivo after neuronal deletion of NAMPT.* J Cereb Blood Flow Metab, 2021. **41**(8): p. 2116-2131.

53. Van Harten, A.C.M., H. Phatnani, and S. Przedborski, *Non-cell-autonomous pathogenic mechanisms in amyotrophic lateral sclerosis.* Trends Neurosci, 2021. **44**(8): p. 658-668.

54. Zhou, Q., et al., *Nicotinamide Riboside Enhances Mitochondrial Proteostasis and Adult Neurogenesis through Activation of Mitochondrial Unfolded Protein Response Signaling in the Brain of ALS SOD1(G93A) Mice.* Int J Biol Sci, 2020. **16**(2): p. 284-297.

55. Yoshino, J., et al., *Nicotinamide mononucleotide, a key NAD(+) intermediate, treats the pathophysiology of diet- and age-induced diabetes in mice.* Cell Metab, 2011. **14**(4): p. 528-36.

56. Yang, L., et al., *Nicotine rebalances NAD(+) homeostasis and improves aging-related symptoms in male mice by enhancing NAMPT activity.* Nat Commun, 2023. **14**(1): p. 900.

57. Zha, S., et al., *PARP1 inhibitor (PJ34) improves the function of aging-induced endothelial progenitor cells by preserving intracellular NAD(+) levels and increasing SIRT1 activity.* Stem Cell Res Ther, 2018. **9**(1): p. 224.

58. Camacho-Pereira, J., et al., *CD38 Dictates Age-Related NAD Decline and Mitochondrial Dysfunction through an SIRT3-Dependent Mechanism.* Cell Metab, 2016. **23**(6): p. 1127-1139.

59. Schondorf, D.C., et al., *The NAD+ Precursor Nicotinamide Riboside Rescues Mitochondrial Defects and Neuronal Loss in iPSC and Fly Models of Parkinson's Disease.* Cell Rep, 2018. **23**(10): p. 2976-2988.

60. Hathorn, T., A. Snyder-Keller, and A. Messer, *Nicotinamide improves motor deficits and upregulates PGC-1alpha and BDNF gene expression in a mouse model of Huntington's disease.* Neurobiol Dis, 2011. **41**(1): p. 43-50.

61. Schaefer, A.M., J.R. Sanes, and J.W. Lichtman, *A compensatory subpopulation of motor neurons in a mouse model of amyotrophic lateral sclerosis.* J Comp Neurol, 2005. **490**(3): p. 209-19.

62. Arbour, D., et al., *Early and persistent abnormal decoding by glial cells at the neuromuscular junction in an ALS model.* J Neurosci, 2015. **35**(2): p. 688-706.

63. Orr, B.O., et al., *Presynaptic Homeostasis Opposes Disease Progression in Mouse Models of ALS-Like Degeneration: Evidence for Homeostatic Neuroprotection.* Neuron, 2020. **107**(1): p. 95-111 e6.

64. Chand, K.K., et al., *Defects in synaptic transmission at the neuromuscular junction precede motor deficits in a TDP-43(Q331K) transgenic mouse model of amyotrophic lateral sclerosis.* FASEB J, 2018. **32**(5): p. 2676-2689.

65. Tremblay, E., E. Martineau, and R. Robitaille, *Opposite Synaptic Alterations at the Neuromuscular Junction in an ALS Mouse Model: When Motor Units Matter.* J Neurosci, 2017. **37**(37): p. 8901-8918.

66. Butti, Z., et al., *Reduced C9orf72 function leads to defective synaptic vesicle release and neuromuscular dysfunction in zebrafish.* Commun Biol, 2021. **4**(1): p. 792.

67. Cappello, V., et al., *Analysis of neuromuscular junctions and effects of anabolic steroid administration in the SOD1G93A mouse model of ALS.* Mol Cell Neurosci, 2012. **51**(1-2): p. 12-21.

68. Xu, Y., et al., *Defects in Neuromuscular Transmission May Underlie Motor Dysfunction in Spinal and Bulbar Muscular Atrophy.* J Neurosci, 2016. **36**(18): p. 5094-106.

69. Casas, C., et al., *Early presymptomatic cholinergic dysfunction in a murine model of amyotrophic lateral sclerosis.* Brain Behav, 2013. **3**(2): p. 145-58.

70. Clark, J.A., et al., *Axonal degeneration, distal collateral branching and neuromuscular junction architecture alterations occur prior to symptom onset in the SOD1(G93A) mouse model of amyotrophic lateral sclerosis.* J Chem Neuroanat, 2016. **76**(Pt A): p. 35-47.

71. Duque, T., et al., *Transforming growth factor-beta plasma levels and its role in amyotrophic lateral sclerosis.* Med Hypotheses, 2020. **139**: p. 109632.

72. Si, Y., et al., *Transforming Growth Factor Beta (TGF-beta) Is a Muscle Biomarker of Disease Progression in ALS and Correlates with Smad Expression.* PLoS One, 2015. **10**(9): p. e0138425.

73. Namboori, S.C., et al., *Single-cell transcriptomics identifies master regulators of neurodegeneration in SOD1 ALS iPSC-derived motor neurons.* Stem Cell Reports, 2021. **16**(12): p. 3020-3035.

74. Kim, M.J. and M.B. O'Connor, *Anterograde Activin signaling regulates postsynaptic membrane potential and GluRIIA/B abundance at the Drosophila neuromuscular junction.* PLoS One, 2014. **9**(9): p. e107443.

75. Fong, S.W., et al., *TGF-beta2 alters the characteristics of the neuromuscular junction by regulating presynaptic quantal size.* Proc Natl Acad Sci U S A, 2010. **107**(30): p. 13515-9.

76. Maity, S., et al., *Sirtuin 6 deficiency transcriptionally up-regulates TGF-beta signaling and induces fibrosis in mice.* J Biol Chem, 2020. **295**(2): p. 415-434.

77. Harlan, B.A., et al., *Enhanced SIRT6 activity abrogates the neurotoxic phenotype of astrocytes expressing ALS-linked mutant SOD1*. FASEB J, 2019. **33**(6): p. 7084-7091.

78. Frederick, D.W., et al., *Loss of NAD Homeostasis Leads to Progressive and Reversible Degeneration of Skeletal Muscle.* Cell Metab, 2016. **24**(2): p. 269-82.

79. Dobrowolny, G., et al., *Skeletal muscle is a primary target of SOD1G93A-mediated toxicity.* Cell Metab, 2008. **8**(5): p. 425-36.

80. Fischer, L.R., et al., *Amyotrophic lateral sclerosis is a distal axonopathy: evidence in mice and man.* Exp Neurol, 2004. **185**(2): p. 232-40.

Chapter 5: Significance and Future Directions

5.1 Significance of current study

This study was designed to explore the effect of NAMPT-mediated NAD^+ salvage pathway on NMJ function and metabolic changes during neurodegenerative conditions in the motor system. In Chapter one, I reviewed cellular NAD metabolism, the role of the NAD^+ salvage pathway in health and neurodegeneration, and the relationship between ALS and NAD^+. In Chapters two and three, using a conditional and inducible projection-neuron targeted NAMPT knockout mouse, I investigated how loss of NAMPT that impairs the NAD^+ salvage pathway affects vesicle recycling in NMJs and metabolic changes in motor cortex. In Chapter four, I examined the effect of dietary NMN supplementation on the functions motor behavior and NMJs in ALS.

For our investigation on the effects of NAMPT deletion from projection neurons on NMJs and neurodegeneration, we used multiple approaches including fluorescent imaging, TEM, LC-MS, and RNA-sequencing, our main findings include the following: 1) NMN can restore the synaptic cycling deficits at the NMJ following NAMPT deletion. 2) NMN improves motor endplate morphology and sarcomere alignment in skeletal muscle after NAMPT loss. 3) NAMPT deletion produces a significantly dysregulated NAD metabolome. 4) NAMPT deletion disrupts cellular bioenergetics, especially glycolysis, and impairs cellular response to oxidative stress. 5) NAMPT deletion up-regulates cell death and inflammatory signaling pathways and down-regulates neurotransmission pathways.

For our investigation into the impact of NMN on ALS, we used NAD assays, motor behavior tests, electrophysiology, immunohistochemistry, TEM, and western blotting analysis, we found that supplementing the diets of $SOD1^{G93A}$ ALS mice with NMN delayed

motor dysfunction by two weeks and modestly increased lifespan. ALS mice had reduced neurotransmission and synaptic plasticity that could be partially restored with NMN. Our NMN diet increased NMJ innervation and improved both motor endplate and IMF mitochondrial morphology, reduced astrocyte activation although loss of spinal cord motor neurons was not prevented. When viewed all together, these findings suggest that NAMPT-mediated NAD^+ salvage pathway is critical for cellular homeostasis and neuronal function, with the novel finding that NMN supplementation can improve synaptic vesicle cycling and reduce neurotransmission deficits in motor neurons experiencing physiological stress from either gene deletion or genetic disease.

Neurodegeneration is a hallmark of both normal aging as well as neurodegenerative diseases. Additionally, the risk of developing a neurodegenerative disease increases with age. Aging and neurodegenerative diseases both feature significant neurodegeneration but the exact cause for the neuronal loss could be due to many different cellular responses, including neuroinflammation, oxidative stress, or bioenergetic dysfunction [1-3]. NAD^+ levels decline with age and increase in response to a variety of behaviors known to improve lifespan. It was soon found that NAD homeostasis is also altered in different diseases, including common neurodegenerative diseases [4, 5]. As the NAD^+ salvage pathway is responsible for the majority of NAD^+ produced in mammalian cells, a more direct investigation into how the salvage pathway is involved in neurodegeneration is needed. While NAMPT was previously understood to be necessary for viability at birth, the importance of NAMPT to motor behavior and survival in adulthood suggests that the effects of an impaired NAD^+ salvage pathway extends well beyond decreased NAD^+ levels

[6, 7]. Our findings provide novel insights into the widespread effects of the NAD^+ salvage pathway on metabolic changes and NMJ function.

Neuroinflammation, oxidative stress, and bioenergetic dysfunction are among the most common features that promote neurodegeneration [8]. Based on our data, deleting NAMPT from projection neurons results in all three being activated in the motor cortex of our conditional knockout mouse. While NAD was known to have some involvement in those pathways, that impairing the NAD metabolome would induce such broad negative effects and stimulate some of the most prominent neurodegenerative-related processes suggests that the critical importance of NAD homeostasis may be underappreciated. Given the significant neurodegenerative effects caused by disrupting the NAD metabolome, the extent that this may also occur in diseased states requires further investigation.

Neurons are the most energetically demanding cells in the body. Within neurons, synaptic activity is considered to be responsible for the majority of energy consumption [9, 10]. We know that loss of NAMPT impairs neuronal energy metabolism and produces significant motor dysfunction, thus how synaptic activity of NMJs is affected by impairing NAD homeostasis should be further investigated. This study found that the synaptic vesicle cycling in the axon terminal of NMJs is substantially affected. NAMPT ablation decreased synaptic vesicle recovery, release, and recruitment from different pools. Importantly, treating the knockout mice with NMN was restorative to the synaptic vesicle cycling. These results implicate a more direct role for NAD^+ in the synaptic function. How this may occur requires more study.

In ALS, the mechanism for the motor neuron death remains an open question, though bioenergetic and oxidative stress are likely involved. Additionally, motor neurons

display dysfunctional cellular energy metabolism early in disease development in ALS [11, 12]. With the deletion of NAMPT inducing bioenergetic distress, oxidative stress and impairing NMJ function, investigating the NAD^+ salvage pathway in the context of a motor neuron disease, specifically ALS, was needed. Our study found that ALS mice experienced a chronic NAD deficit that occurred well before appearance of physical symptoms. This finding suggests that the loss of NAD may be the driving force of the early bioenergetic deficits. Additionally, we found that the neurotransmission impairments that occur at NMJs in ALS mice could be significantly restored by providing NMN in mouse diet. This further establishes an important role for the NAD^+ salvage pathway in NMJ function.

When considered all together, the NAD^+ salvage pathway is critically important to neurons, in both healthy and diseased states, and NMN, an NAD^+ precursor, can provide significant therapeutic benefits when NAD homeostasis has been impaired. Further work needs to be performed to identify what is acting downstream from NAD^+. With NAD^+ serving as both a reusable redox molecule and being a substrate for NAD^+-consuming enzymes, there are many potential mechanisms of action for why NMN supplementation is therapeutic. Identifying this could help improve the efficacy for any treatments involving NAD^+ precursor metabolites.

5.2 Potential directions for the further study

Further investigation into a mechanism of action for NMN could be done using *in vitro* co-cultures of human motor neurons and skeletal muscle fibers. This would provide results more translatable to humans while also providing the ability to more easily perform live imaging, recording, and enzyme assessments. This approach would provide a direct method to study the relationship between motor neurons and skeletal muscle in ALS with and without NMN. We could evaluate: 1) formation and loss of NMJs; 2) NMJ function; 3) activity of NAD^+ consuming enzymes, such as SIRT1 or PARP1; 4) impact of inhibitors or activators of NAD^+ consuming enzymes; 5) gene and protein expression changes in motor neurons. The findings from this approach should identify the specific therapeutic mechanisms of action that NMN produces during ALS.

A future *in vivo* study of ALS could use a different method to achieve elevated NAD^+. With CD46 transgenic mouse, we can over-express NAMPT in red blood cells using an adenovirus encoding NAMPT [13]. This procedure can increase blood and brain NAD^+ levels. Due to the aggressive disease time course for $SOD1^{G93A}$ ALS mice, this approach may be best tested using an ALS mouse model with slower symptom development like $SOD1^{G37R}$ ALS mice [14]. This method would allow a constant increase in NAD^+ without the fluctuations that occur with daily injections. This approach would allow investigating motor behavior and systemic bioenergetics over a longer period. We could evaluate: 1) Disease on-set and symptom progression; 2) Impact on hypermetabolism, which can occur during ALS, using metabolic cages; 3) The NAD metabolome at critical timepoints during ALS development using LC-MS; 4) Cytokine responses in the blood, spinal cord, and brain using ELISA; 5) Calcium dependent vesicle release at NMJs using EPP recordings, where

stimulation frequency is held constant but different calcium concentrations are used in the recording chamber. The results from these experiments would provide insight into how long-term elevated NAD^+ effects motor behavior, energy metabolism, and NMJ function.

With regards to the findings of this dissertation, more research into the benefits of NMN supplementation on ALS is needed. While adding NMN to the food was effective at delaying the decline in motor activity in ALS mice, this procedure may not lead to the most consistent dietary NMN supplementation. First, the diet was made by hand weekly and while care was taken to make the pellets as uniform as possible, it is likely that the NMN was not always distributed evenly. Second, while the pellets were stored in an air-tight container in the dark before use, when the pellets were fed to the mice they were constantly exposed to air and 12 hours of light. This may have degraded the NMN more quickly. One possible alternative would be to add the NMN to the drinking water instead. This would allow the NMN to be uniformly distributed and every drink would contain the same concentration of NMN. The bottles would minimize air exposure and could be wrapped in tin foil to eliminate light exposure.

While administering NAD^+ precursors to mice has been shown to be effective at elevating NAD^+ levels, improving NAD^+ biosynthesis is not the only manner that can increase NAD^+ availability. The activity of NAD^+ consuming enzymes, such as PARPs or CD38, can decrease NAD^+ levels. There is evidence indicating that NAD^+ consumption has increased in ALS. Increased nuclear PAR was found in the spinal cord motor neurons of ALS patients, suggesting elevated PARP activity [15]. While CD38 has predominantly been investigated for a role in the aging process, CD38 inhibition has been shown to be effective at increasing NAD^+ levels. Administering PARP or CD38 inhibitors can increase

NAD^+ levels in multiple tissues and pairing inhibitors together has an additive effect [16]. However, whether these inhibitors have any effect on NAD^+ levels in ALS has not been investigated. Furthermore, pairing NMN supplementation with PARP or CD38 inhibition may also prove more effective treatments against ALS.

While the NAD^+ salvage pathway is responsible for the majority of NAD^+ synthesized in cells, more research is needed into understanding the extent that NAD homeostasis may be impaired during ALS. One aspect needed more study is the *de novo* pathway, also called the kynurenine pathway, which utilizes tryptophan. Intermediate metabolites generated within the *de novo* pathway are considered to be neurotoxic [17]. There is metabolic evidence suggesting that the *de novo* pathway is dysregulated in ALS. In ALS patient CSF samples, there was an decrease in metabolites of the kynurenine pathway but an increase in the ratio of neurotoxic to neuroprotective metabolites suggesting that the overall activity of the *de novo* pathway may be reduced but with a tendency to form the neurotoxic intermediates [18]. One specific metabolite of interest would be 2-amino-3-carboxymuconic-6-semialdehyde (ACMS). ACMS can generate quinolinic acid, which can be neurotoxic if accumulated [19], in a spontaneous reaction or can be utilized by the enzyme ACMSD and converted into a metabolite that can be used to generate picolinic acid, a neuroprotective metabolite, or further converted into acetyl-CoA. In ALS patient blood plasma and CSF, picolinic acid was lower and quinolinic acid was increased and that tryptophan metabolism may be impaired [20, 21]. Additionally, we found that ACMSD expression was upregulated in the lumbar spinal cord of end-stage ALS mice. Overall, this suggests that multiple NAD^+ biosynthetic pathways may be impaired during ALS.

More investigation into the neuromuscular junction is necessary for both the Thy1-NAMPT$^{-/-}$ and ALS mice. For the Thy1-NAMPT$^{-/-}$ mice, EPP responses could be recorded from the diaphragm. These results may provide information concerning whether the phrenic nerve and diaphragm are functioning appropriately. Given that Thy1-NAMPT$^{-/-}$ mice exhibit a phenotype similar to ALS mice and ALS mice generally die from asphyxiation, this may provide more insight into whether Thy1-NAMPT$^{-/-}$ mice also experience dysfunction. For the ALS mice, an FM dye could be used to visualize the synaptic vesicle endocytosis and exocytosis and the NMJs in the semitendinosus muscle, similar to what was performed on the Thy1-NAMPT$^{-/-}$ mice. This would provide insight into the synaptic vesicle cycle of the ALS NMJ.

Additionally, for both Thy1-NAMPT$^{-/-}$ and ALS mice, labelling synaptic vesicles with FM dye could be used to assess the different vesicle pools using TEM. The labelling procedure would remain the same with stimulation occurring in the presence of the FM dye. However, after the vesicles have been labelled, the muscle could be fixed and incubated with diaminobenzidine (DAB). When DAB is exposed to fluorescent light, it oxidizes. This process both labels the synaptic vesicles and allows the nerve terminal to be seen under transmitted light. The labelled NMJ dense regions can more accurately be dissected out and prepared for TEM [22, 23]. The NMJ images from TEM can be used to analyze the synaptic vesicle pool within the nerve terminal, where the synaptic vesicles will appear as electron dense spots. If any synaptic vesicle release problems are observed, you could perform the entire FM procedure but end stimulation before too much dye has been released. This would help determine whether a portion of labelled vesicles are not being actively used during NMJ stimulation. TEM images of the nerve terminal of the NMJ

would provide information concerning synaptic vesicle density, size, and organization around the active sites.

In ALS mice, skeletal muscle undergoes significant atrophy as well as other changes including muscle fibers transitioning from one type to a different type [24]. Skeletal muscles of varying fiber type composition, such as semitendinosus, gastrocnemius, EDL, and soleus, could be isolated and stained with multiple fiber-type specific antibodies. Results from this would allow for a better understanding of the proportion of the fast-glycolytic (Type IIb), fast-oxidative (Type IIa), and slow (Type I) twitch fibers in hindlimb skeletal muscles. The TEM imaging from ALS mice suggests that mitochondrial morphology is altered in skeletal muscle. Whether this morphological change also has an impact on function is not known. Mitochondria could be isolated from dissected skeletal muscle and, using microplate-based respirometric assays, mitochondrial function (oxygen consumption rate/OCR) can be determined [25]. Mitochondria from other tissues, like cerebral cortex or spinal cord, could be isolated and OCR assessed as well. Importantly, all the previously discussed potential experiments should contain a group of ALS mice receiving NMN and a group of ALS mice not provided the NMN supplementation.

5.3 References

1. Hou, Y., et al., *Ageing as a risk factor for neurodegenerative disease.* Nat Rev Neurol, 2019. **15**(10): p. 565-581.
2. Campisi, J., et al., *From discoveries in ageing research to therapeutics for healthy ageing.* Nature, 2019. **571**(7764): p. 183-192.
3. Strope, T.A., C.J. Birky, and H.M. Wilkins, *The Role of Bioenergetics in Neurodegeneration.* Int J Mol Sci, 2022. **23**(16): p. 9212.
4. Chu, X. and R.P. Raju, *Regulation of NAD(+) metabolism in aging and disease.* Metabolism, 2022. **126**: p. 154923.
5. Xie, N., et al., *NAD(+) metabolism: pathophysiologic mechanisms and therapeutic potential.* Signal Transduct Target Ther, 2020. **5**(1): p. 227.
6. Wang, X., et al., *Deletion of Nampt in Projection Neurons of Adult Mice Leads to Motor Dysfunction, Neurodegeneration, and Death.* Cell Rep, 2017. **20**(9): p. 2184-2200.
7. Revollo, J.R., et al., *Nampt/PBEF/Visfatin regulates insulin secretion in beta cells as a systemic NAD biosynthetic enzyme.* Cell Metab, 2007. **6**(5): p. 363-75.
8. Dugger, B.N. and D.W. Dickson, *Pathology of Neurodegenerative Diseases.* Cold Spring Harb Perspect Biol, 2017. **9**(7): p. a028035.
9. Cheng, X.T., N. Huang, and Z.H. Sheng, *Programming axonal mitochondrial maintenance and bioenergetics in neurodegeneration and regeneration.* Neuron, 2022. **110**(12): p. 1899-1923.
10. Li, S. and Z.H. Sheng, *Energy matters: presynaptic metabolism and the maintenance of synaptic transmission.* Nat Rev Neurosci, 2022. **23**(1): p. 4-22.

11. Obrador, E., et al., *The Link between Oxidative Stress, Redox Status, Bioenergetics and Mitochondria in the Pathophysiology of ALS.* International Journal of Molecular Sciences, 2021. **22**(12): p. 6352.

12. Barone, C. and X. Qi, *Altered Metabolism in Motor Neuron Diseases: Mechanism and Potential Therapeutic Target.* Cells, 2023. **12**(11): p. 1536.

13. Wang, H., et al., *High-level protein production in erythroid cells derived from in vivo transduced hematopoietic stem cells.* Blood Adv, 2019. **3**(19): p. 2883-2894.

14. Tremblay, E., E. Martineau, and R. Robitaille, *Opposite Synaptic Alterations at the Neuromuscular Junction in an ALS Mouse Model: When Motor Units Matter.* J Neurosci, 2017. **37**(37): p. 8901-8918.

15. McGurk, L., et al., *Nuclear poly(ADP-ribose) activity is a therapeutic target in amyotrophic lateral sclerosis.* Acta Neuropathol Commun, 2018. **6**(1): p. 84.

16. Tarrago, M.G., et al., *A Potent and Specific CD38 Inhibitor Ameliorates Age-Related Metabolic Dysfunction by Reversing Tissue NAD(+) Decline.* Cell Metab, 2018. **27**(5): p. 1081-1095 e10.

17. Chen, Y. and G.J. Guillemin, *Kynurenine pathway metabolites in humans: disease and healthy States.* Int J Tryptophan Res, 2009. **2**: p. 1-19.

18. Alarcan, H., et al., *Some CSF Kynurenine Pathway Intermediates Associated with Disease Evolution in Amyotrophic Lateral Sclerosis.* Biomolecules, 2021. **11**(5): p. 691.

19. Loganathan, C. and P. Thayumanavan, *Asiatic acid prevents the quinolinic acid-induced oxidative stress and cognitive impairment.* Metab Brain Dis, 2018. **33**(1): p. 151-159.

20. Chen, Y., et al., *The Kynurenine Pathway and Inflammation in Amyotrophic Lateral Sclerosis.* Neurotoxicity Research, 2010. **18**(2): p. 132-142.

21. Tan, V.X. and G.J. Guillemin, *Kynurenine Pathway Metabolites as Biomarkers for Amyotrophic Lateral Sclerosis.* Front Neurosci, 2019. **13**: p. 1013.

22. Hoopmann, P., S.O. Rizzoli, and W.J. Betz, *FM dye photoconversion for visualizing synaptic vesicles by electron microscopy.* Cold Spring Harb Protoc, 2012. **2012**(1): p. 84-6.

23. Opazo, F. and S.O. Rizzoli, *Studying synaptic vesicle pools using photoconversion of styryl dyes.* J Vis Exp, 2010(36): p. e1790.

24. Hegedus, J., et al., *Preferential motor unit loss in the SOD1 G93A transgenic mouse model of amyotrophic lateral sclerosis.* J Physiol, 2008. **586**(14): p. 3337-51.

25. Boutagy, N.E., et al., *Isolation of Mitochondria from Minimal Quantities of Mouse Skeletal Muscle for High Throughput Microplate Respiratory Measurements.* J Vis Exp, 2015(105): p. 53217.

VITA

Samuel Lundt was born in Ida Grove, Iowa on September 29th, 1991. In 2014 he received a Bachelor's of Science in Psychology from Iowa State University in Ames, Iowa. In 2017, he attained a Bachelor's of Science in Biology from the University of Iowa in Iowa City, Iowa. Also in 2017, he was admitted to the University of Missouri in the Interdisciplinary Neuroscience Program and joined Dr. Shinghua Ding's lab to further his research interests in neuroscience. His specialties are animal behavior tests, immunohistochemistry, and *ex vivo* neuromuscular stimulation and recording.